Forschungszentrum Jülich

Institut für Schicht- und Ionentechnik

Electrodynamic Properties of Oxide Superconductors

Norbert Klein

Jül-3773

Berichte des Forschungszentrums Jülich 3773

Electrodynamic Properties of Oxide Superconductors

Norbert Klein

Berichte des Forschungszentrums Jülich ; 3773
ISSN 0944-2952
Institut für Schicht- und Ionentechnik Jül-3773
D82 (Habil.-Schr. RWTH Aachen, 1997)

Zu beziehen durch: Forschungszentrum Jülich GmbH · Zentralbibliothek
D-52425 Jülich · Bundesrepublik Deutschland
☎ 02461/61-6102 · Telefax: 02461/61-6103 · e-mail: zb-publikation@fz-juelich.de

Abstract

The electrodynamic properties of oxide high temperature superconductors are reviewed. Most of the experimental data are from thin films and bulk single crystals of $YBa_2Cu_3O_{7-x}$, which – together with thin films of thallium-based oxide superconductors – provide the lowest microwave losses making epitaxially grown thin films attractive for applications in microwave technology. Among the various techniques for the determination of the electrodynamic response of superconducting thin films cavity, dielectric, and planar resonators are the most successful ones for the frequency range from 1 to 100 GHz. For the millimeter and submillimeter wave range nonresonant transmission techniques in frequency and time domain have been used successfully. Bulk single crystals have been studied by various types of cavity perturbation techniques.

$YBa_2Cu_3O_{7-x}$ bulk single crystals and epitaxial thin films exhibit a steep drop of the surface resistance R_s just below the transition temperature T_c to values at 77 K which are about 300 $\mu\Omega$ at 10 GHz. The observed dependence on the frequency f can be described by f^A with sample-dependent A values between 1.5 and 2. At lower temperatures $R_s(T)$ is substantially different both from that predicted by BCS theory and observed experimentally for conventional superconductors. Typically, $R_s(T)$ exhibits a plateau between 30 and 70 K corresponding to a frequency-dependent maximum in the real part of the conductivity. The observed correlation of the height of this maximum to the defect density indicates that above about 30 K the electrodynamic response is dominated by a strong decrease of the quasiparticle lifetime just below T_c. Below $T_c/2$ the situation is still quite unclear. The observed temperature dependences both for R_s and the London penetration depth λ_L range from weak exponential corresponding to energy gaps more than two times smaller than expected from weak-coupling BCS theory over quadratic to linear dependences. In any case, a high residual surface resistance $R_{res} = R_s(T \rightarrow 0)$ remains. In particular, the low temperature regime was found to be strongly affected by the amount and ordering of oxygen vacancies in the copper-oxygen chains. The active role of the copper-oxygen chains as a conducting subsystem was worked out theoretically within a strong-coupling theory based on phonon-mediated superconductivity and can quantitatively explain some of the observed results. In particular, gapless superconductivity can be easily achieved from magnetic pair breaking in the copper-oxygen chains. *d*-wave superconductivity, as expected for superconductivity mediated by spin fluctuations instead of phonons, leads to a gapless behavior as well. The observed temperature dependences of λ_L and R_s can be explained to some extent within *d*-wave models. In contradiction to the hole doped cuprates (as e.g. $YBa_2Cu_3O_{7-x}$), the electron doped cuprates exhibit an electromagnetic response which is similar to predictions for an isotropic *s*-wave order parameter.

The dependence of the surface resistance on the amplitude of the high frequency magnetic field is of particular importance as it defines the limitation of the applicability of high temperature superconductor films for passive microwave devices operating at elevated levels of microwave power. The observed dependences were found to be strongly sample dependent. For the best films of $YBa_2Cu_3O_{7-x}$ R_s is independent of the field amplitude up to about 200 Oe at a temperature of 10 K, limited in most cases by a field breakdown at a certain field level (quench). The field amplitude at which the quench occurs decreases with increasing temperature. Such breakdown is most likely to originate from local defects. However, even films with low R_s values at low field levels sometimes exhibit strong field dependences at field levels of a few Oerstedt. Generally, the observed field dependences for thin films of the Tl-Ba-Ca-Cu-O compound are stronger than for $YBa_2Cu_3O_{7-x}$.

In the vortex state the electrodynamic response was found to be determined by the viscous motion of vortices within their pinning potentials. The analysis of the observed field dependences of the surface impedance at different temperatures allows to determine the temperature dependence of the average pinning force constant and the vortex viscosity (at $T << T_c$). In spite of strongly sample dependent results the temperature dependence of the pinning force constant can be understood assuming pinning potentials which are smeared due to thermal fluctuations. For the vortex viscosity the Bardeen-Stephen formula is in agreement with the observed temperature dependences.

Contents

Chapter 1

Introduction

Microwave technology has become one of the key areas for applications of high temperature superconductors. Low microwave losses at temperatures attainable with compact closed cycle cryocoolers or liquid nitrogen have initiated the development of various HTS-based passive microwave devices (HTS = high temperature superconductor) like transmission lines, resonators, filters, and antennas. The presently ongoing system implementation of such devices has a large potential to impact satellite and cellular phone communication, electronic warfare, and medical diagnostics ([1] and references therein, [2]).

The successful preparation of epitaxial thin films of HTS material with microwave surface resistance R_s at 77 K being significantly below that of any normal-conducting metal up to the millimeter-wave range [3] has stimulated device development as well as extensive investigation of the electrodynamic properties from the low Gigahertz range up to the optical range (corresponding to frequencies in the range of 10^{14} Hz) [4]. The electrodynamic response of the HTS cuprates was found to exhibit substantial deviations from that of conventional superconductors. Although to date a complete microscopic understanding of the observed temperature and frequency dependences, and the effects of dc and rf magnetic fields on the surface resistance (and penetration depth as well) has not yet been attained, several possible scenarios have been worked out in detail, providing convincing explanations for many of the experimental results.

In this review the electrodynamic properties of HTS cuprates are discussed with emphasis on frequencies where the dominant absorption processes are initiated by thermally excited quasiparticles. This is the range from several hundred Megahertz up to a few Terahertz, the latter belonging already to the far-infrared range. Infrared and optical absorption, however, which are dominated by direct quasiparticle excitation as well as phonon and interband absorption processes (see e.g. [5]), are beyond the scope of this review.

In Chapter 1 various theoretical approaches are reviewed starting from phenomenological models. Based on the two-fluid model and Fermi's Golden Rule simple relations between the quasiparticle density of states and the low temperature behavior of the surface impedance are derived. The temperature and frequency dependence of the surface impedance at elevated temperatures can be understood within the two-fluid model, if a Drude ansatz is employed for the conductivity of the normal-conducting fluid. The effects of pair breaking and granularity of the HTS material give possible explanations for the observed dependencies of R_s (and penetration depth as well) on the amplitude of the high frequency magnetic field.

Calculations of the surface impedance in the framework of microscopic theories have been quite successful in the past two years. In contrast to the case of classical superconductors, the theory of Bardeen, Cooper and Schrieffer (BCS theory) does not describe the surface impedance of the cuprates correctly. Various modifications and extensions of the BCS approach have meanwhile been worked out taking into account the peculiar band structure of the cuprates and effects of strong-coupling phonon-mediated superconductivity as well. Moreover, predictions for the surface impedance in the framework of models describing a *d*-wave pairing state will be reviewed. *d*-wave superconductivity has gained increasing attention as it turns out to be a fingerprint of a new mechanism of superconductivity in the cuprates. Finally, the microwave losses above the lower critical field H_{c1} were described successfully within a model combining viscous and thermally excited motion of vortices within their pinning potentials with absorption by the quasiparticles in the vortex cores.

In Chapter 2 the experimental techniques for determining the surface impedance of thin films and bulk single crystals are reviewed. Chapter 3 is a selection of representative experimental results, most of them for epitaxially grown thin films and bulk single crystals of $YBa_2Cu_3O_{7-x}$. However, in spite of the poorer sample quality surface impedance investigation of other cuprates, in particular the electron doped (n-type) cuprates, has turned out to be important for understanding the underlying physics. Thin films of some of the Tl-Ba-Ca-Cu-O compounds have become the most important competitors of $YBa_2Cu_3O_{7-x}$ for applications in microwave technology. Granular materials, like thick films on curved substrates, are quite important for applications at low frequencies and therefore have been studied extensively as well [6]. However, granular materials are beyond the scope of this article, which – to a large extent – is defined by the question: “What can we learn about the intrinsic properties of the HTS cuprates by looking at the electrodynamic response?”

Chapter 2

Theory: Electrodynamic response of superconductors

The interaction between electromagnetic waves and superconductors is determined by material properties from two different viewpoints:

Firstly, by intrinsic electronic properties which are related to both the superconducting condensate and the quasiparticles. In particular, the penetration depth of an electromagnetic wave is determined by the density of superconducting charge carriers. The absorption process, however, is determined by the interaction of the electromagnetic wave with the quasiparticles. Here the most important energy scale is the energy gap of size 2Δ in the quasiparticle density of states. At frequencies $f = \omega/2\pi$ corresponding to photon energies $\hbar\omega < 2\Delta$ thermally excited quasiparticles dominate the absorption process. According to BCS theory the size of the energy gap is related to the critical temperature T_c of a superconductor by $2\Delta = 3.52kT_c$ (weak-coupling limit). However, for the majority of superconductors with $T_c > 10$ K $2\Delta/kT_c$ is larger than 3.52. This is a result of strong electron-phonon coupling (see Section 2.2.2 and [7, 8]). Direct quasiparticle excitation by photons is restricted to a narrow temperature range close to T_c where the width of the energy gap approaches zero. For HTS materials a highly anisotropic energy gap (see Section 2.2.3) and/or two distinct gap energies resulting from two distinct bands crossing the Fermi level (see Section 2.2.2) make the situation more complicated. Moreover, due to strong electron-electron scattering resulting from the peculiar shape of the Fermi surface (see Section 2.2.2) the observed temperature dependence of the surface resistance is determined by a strong temperature dependence of the quasiparticle scattering rate.

Secondly, the electrodynamic response of a superconductor is strongly affected by material imperfections. In the case of conventional superconductors with a well defined energy gap the intrinsic surface resistance approaches zero for $T \rightarrow 0$. However, experimentally a small residual surface resistance R_{res} remains observable down to the lowest temperatures. In conventional superconductors R_{res} results from normal-conducting regions, frozen-in magnetic flux, or dielectric oxide layers [12]. Since the coherence length of conventional superconductors is quite large (e.g. 30 nm for niobium, [13]) imperfections of size smaller than the coherence length become superconducting by the proximity effect. Therefore very low values of R_{res} in the range of $10^{-9}\ \Omega$ are achievable even for polycrystalline niobium [12]. As a result of the short coherence length of HTS materials [14] here the magnitude of extrinsic losses caused by impurities and material imperfections is expected to be larger. As an example large angle grain boundaries exhibit weak link behavior [15, 16] resulting in a strong dependence of the absorption on the amplitude of the electromagnetic fields and on external dc magnetic fields (see Section 2.2.1).

2.1 Conventional superconductors

The designations "classical" and "conventional" for a superconducting material are somewhat fuzzy with respect to its properties. As an example, even among the cuprates there are substances which exhibit electrical transport properties in the normal state like conventional metals, and superconducting properties which are partially in good agreement with BCS theory. In this section more general theoretical approaches are discussed, which are not tailored to the superconducting cuprates. However, this does not exclude their validity for these particular materials.

2.1.1 Surface impedance and conductivity

Consider a plane electromagnetic wave propagating in an isotropic non-magnetic medium in z-direction of a cartesian coordinate system with electric field vector $\vec{E} = E_x\vec{e_x}$. The time and z dependence of E_x is assumed to be purely harmonic, i.e. $E_x \propto \exp[-i(\omega t - \beta z)]$. The quantity β is called propagation constant of the medium.

The magnetic field vector $\vec{H} = H_y\vec{e_y}$ can be calculated from $\vec{E}$ using Maxwell's equation $\vec{\nabla}\times\vec{E} = -\mu_0\partial\vec{H}/\partial t$. The ratio of E_x and H_y is called plane wave impedance of the medium, which is related to β by:

$$Z = \frac{E_x}{H_y} = \frac{\omega\mu_0}{\beta} \tag{2.1}$$

The plane wave impedance is defined by analogy with the impedance of a transmission line, which is defined as the ratio of voltage and current per unit length.

Consider now an isotropic dielectric medium with complex permittivity $\epsilon_r = \epsilon_{r,1} + i\epsilon_{r,2}$. According to Maxwell's equation $\vec{\nabla} \times \vec{H} = \vec{j} + \partial\vec{D}/\partial t$ the magnetic field induces a non-dissipative displacement current $\vec{j_D} = \partial\vec{D}/\partial t$. For a harmonic time dependence of the electric field the displacement current is given by:

$$\vec{j_D} = -i\omega\epsilon_0\epsilon_{r,1}\vec{E} \tag{2.2}$$

$\vec{j}_D$ is non-dissipative because current and electric field are out of phase by 90°. The small imaginary part of the permittivity $\epsilon_{r,2}$, however, gives rise to a small dissipative current density of the order $\omega\epsilon_{r,2}\epsilon_0\vec{E}$.

In a conducting medium the displacement current can be neglected in comparison to the ohmic current $\vec{j} = \sigma\vec{E}$. Here the conductivity σ is the relevant quantity, which is formally related to ϵ_r by $\sigma = i\omega\epsilon_0\epsilon_r$. This formal equivalence of permittivity and conductivity allows to treat dielectrics and metals in the same way.

By combining Maxwell's equations the wave equation for plane electromagnetic waves can be derived [17] providing simple expressions for β and hence for the impedance of the medium (Eq. 2.1). For a non-dissipative dielectric material with $\epsilon_{r,2}$=0 β is real and the impedance follows from Eq. 2.1

$$Z = \sqrt{\frac{\mu_0}{\epsilon_{r,1}\epsilon_0}} = \frac{Z_0}{\sqrt{\epsilon_{r,1}}} \tag{2.3}$$

with $Z_0 = 376\ \Omega$ being the wave impedance of the vacuum. In a conducting medium β becomes purely imaginary and the solutions of the wave equation are exponentially decaying waves. For a normal-conducting metal the relevant decay length is called skin depth $\lambda_n = \sqrt{2/(\omega\mu_0\sigma)}$, which is in the micrometer range for high-conductivity metals at frequencies in the Gigahertz range. Therefore, the impedance of a conducting medium is called surface impedance Z_s:

$$Z_s = \sqrt{\frac{i\omega\mu_0}{\sigma}} \tag{2.4}$$

The real part of Z_s is called surface resistance R_s. R_s is proportional to the power loss per unit area dP/dA:

$$dP/dA = \frac{1}{2}|\vec{E} \times \vec{H}^*| = \frac{1}{2}R_s H_y^2 \tag{2.5}$$

The imaginary part of Z_s is called surface reactance X_s. X_s is proportional to the penetration depth λ of E_x and H_y:

$$\lambda = \frac{X_s}{\omega\mu_0} \tag{2.6}$$

The electrodynamic response of a normal-conducting metal can be described by a Drude-conductivity

$$\sigma = \frac{e^2 N}{\tau m^*}\frac{1}{1 - i\omega\tau} \tag{2.7}$$

with charge carrier density N, scattering time τ, and effective mass m^*. In the Gigahertz frequency range $\omega\tau << 1$ holds, i.e. the imaginary part of σ is neglegible. Eq.2.4 can then be simplified:

$$Z_s = \sqrt{\frac{\omega\mu_0}{2\sigma}}(1+i) \tag{2.8}$$

Eq.2.8 describes the so-called normal skin effect, i.e. surface resistance and surface reactance are equal. However, if the skin depth comes in the order of the mean free path l of the charge carriers, Ohm's law is no longer fulfilled. This is because Ohm's law implies a local relation between electric field and current density, i.e. there is no variation of electric field on the distance scale of l. Reuter and Sondheimer first developed the theory of the anomalous skin effect based on a nonlocal current-field relation [27]. This theory describes the temperature dependence of the surface impedance down to zero Kelvin very well. The most important result is a low temperature limit of the surface impedance of high-purity metals ($l \to \infty$), which is independent of the conductivity:

$$Z_s(l \to \infty) = \frac{\iota}{2}\mu_0 \left[\frac{\sqrt{3}}{2^{\pi}} \frac{v_F m^* \omega^2}{\mu_0 N e^2}\right]^{1/3} [1+\sqrt{3}i] \tag{2.9}$$

In Eq. 2.9 v_F is the Fermi velocity and $\iota = 8/9$ for specular and $\iota = 1$ for diffuse reflection of the charge carriers at the surface, respectively. The frequency dependence of R_s for a metal with high conductivity like copper changes continously from $f^{2/3}$ to $f^{1/2}$ upon inreasing the temperature from 4 K to room temperature. The low temperature limit of R_s for copper ($N = 8.45 \cdot 10^{28}\ \mathrm{m}^{-3}, m^* \approx m_e$, $v_F = 1.57 \cdot 10^6$ m/s) at a frequency of 10 GHz is 4.7 mΩ, the room temperature R_s value is 26 mΩ (from Eq.2.8 using $\sigma = 5.8 \cdot 10^7\ (\Omega\mathrm{cm})^{-1}$). This indicates only a moderate improvement of the performance of conventional microwave devices by employing cryogenic temperatures.

The most simple model for describing the electrodynamic response of a superconductor is based on the London equations [19, 13] and on the two-fluid model [20]. According to the London equations an applied alternating magnetic field induces an alternating supercurrent, which is non-dissipative. According to the two-fluid model normal-conducting charge carriers coexist except at $T = 0$. In contrast to a dc electric field, the current due to the normal-conducting charge carriers is not shunted by the supercurrent. The physical reason is the inertia of the superconducting charge carriers, which gives rise to a small electric field in the superconducting metal. Formally, the electrodynamic response of a superconductor can be described by a complex conductivity:

$$\sigma = \sigma_1 - i\sigma_2 \tag{2.10}$$

The real part of σ is the conductivity of the normal-conducting charge carriers:

$$\sigma_1(T) = \frac{e^2 N_n(T)}{\tau(T) m^*} \tag{2.11}$$

Eq. 2.11 corresponds to Eq. 2.7 modified by a temperature dependent density of normal-conducting charge carriers $N_n(T)$. The imaginary part of σ is the conductivity of the superconducting charge carriers

$$\sigma_2(T) = \frac{2e^2 N_s(T)}{\omega m^*} = \frac{1}{\omega \mu_0 \lambda_L^2} \tag{2.12}$$

with temperature dependent density of superconducting charge carriers $N_s(T)$. The quantity $\lambda_L = \sqrt{m^* \mu_0 / (2e^2 N_s)}$ is called London penetration depth of a superconductor. The London penetration depth describes the decay length of an applied magnetic field from the surface of a superconductor into the bulk, which is free of magnetic field due to the Meissner effect.

According to Eqs. 2.4, 2.10, and 2.12 the surface impedance of a superconductor is given by the following expression:

$$Z_s = \sqrt{\frac{i\omega\mu_0}{\sigma_1 - \frac{i}{\omega\mu_0\lambda_L^2}}} \tag{2.13}$$

Since in the two-fluid model $N_n(T)$ drops very fast with decreasing temperature, the ratio $\sigma_1/\sigma_2 = \frac{1}{2}(N_n(T)/N_s(T))(\omega/\tau^{-1}(T))$ is always smaller than one, except for a narrow range close to T_c. Under this condition the real and imaginary part of Z_s can be separated:

$$R_s \approx \frac{1}{2}\omega^2 \mu_0^2 \sigma_1 \lambda_L^3 \quad \text{and} \quad X_s \approx \omega\mu_0\lambda_L \tag{2.14}$$

In contrast to a normal-conducting metal, R_s shows a quadratic dependence on frequency. Just below T_c an initial drop of $R_s(T)$ occurs due to the strong temperature dependence of λ_L [13]. Below about $T_c/2$, $R_s(T)$ is dominated by the temperature dependence of σ_1. In the original work of Gorter and Casimir $N_n(T) = 1 - N_s(T)$ was predicted to depend on temperature as $(T/T_c)^4$ [20]. Between $T_c/2$ and T_c this was found to be in qualitative agreement with the experimental results. However, below about $T_c/2$ an exponential temperature dependence was found experimentally for many classical superconductors. A full understanding of the experimentally observed frequency and temperature dependences of the surface impedance was achieved within BCS theory, as described in the next section.

Finally, some constraints in using the concept of surface impedance are worth mentioning. In the microwave range measurements are performed with cavity or planar resonators (see Chapter 3). For cavity resonators the impedance approach is justified for the following reason. Consider Maxwell's equation $\vec{\nabla} \times \vec{H} = -\sigma \vec{E}$ (displacement current neglected) in cartesian coordinates as explained before with the z-direction oriented perpendicular to the surface of the cavity wall. At the surface ($z = 0$) $\vec{\nabla} \times \vec{H} = (\partial/\partial x, \partial/\partial y, \partial/\partial z) \times (0, H_y, 0) = (-\partial H_y/\partial z, 0, \partial H_y/\partial x)$. Since $\partial H_y/\partial z$ is of the order of H_y devided by the penetration depth (micron range) and $\partial H_y/\partial x$

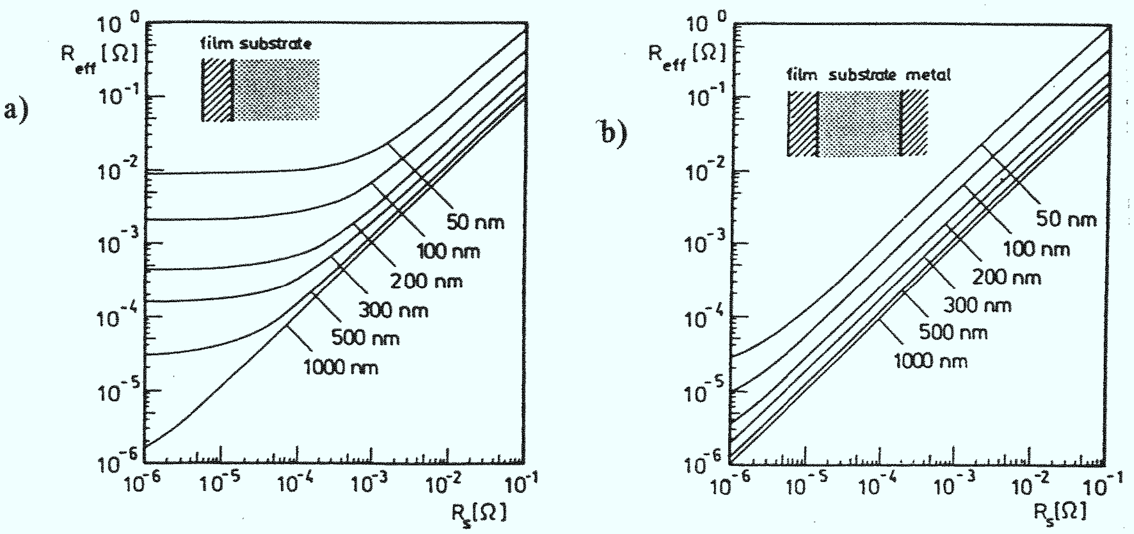

Fig. 2.1a,b: Surface resistance R_{eff} at given film thickness t_f from $t_f = 50$ to 1000 nm as a function of surface resistance at infinite film thickness (R_s), calculated numerically by impedance transformations at $f = 87$ GHz. For the penetration depth $\lambda_L = 260$ nm was used corresponding to $YBa_2Cu_3O_{7-x}$ at 77 K, the substrate permittivity is $\epsilon_r = 16$. In case of an infinitely extended substrate (a) the transmission losses are given by $R_{trans} = \epsilon_r^{1/2}(\omega\mu_0\lambda_L)^2/(Z_0 \sinh^2(t_f/\lambda_L))$, corresponding to the horizontal parts of the curves in Fig. 2.1a. In case of a finite, non-resonant substrate (Fig. 2b) transmission losses are suppressed and the results correspond to Eq. 2.15 (from [21]).

of the order of H_y devided by the vacuum wavelength (centimeter range), $\partial H_y/\partial x$ can be neglected. Therefore the electric field has only one component in x-direction, corresponding to a plane wave propagating in z-direction.

For the case of a thin film with thickness t_f in the order of or smaller than λ_L, the reflection of the electromagnetic wave at the film-substrate interface needs to be taken into account. Neglecting the transmission of electromagnetic energy through the film into the substrate the surface impedance of a superconducting film at finite thickness is well approximated according to Klein et al. [21]:

$$R_s = R_s(t_f \to \infty)(\coth(t_f/\lambda_L) - \frac{t_f/\lambda_L}{\sinh^2(t_f/\lambda_L)}) \quad \text{and} \quad X_s = X_s(t_f \to \infty)\coth(t_f/\lambda_L) \tag{2.15}$$

Eq. 2.15 is meaningful for the comparison of experimental data obtained on films with different thicknesses. It should be emphasized that Eq. 2.15 is not valid too close to T_c since it relies on the approximation $\sigma_1/\sigma_2 << 1$. Fig. 2.1a shows R_s at different values of the film thickness for a dielectric substrate which is extended to infinity in the direction perpendicular to the surface. Here, R_s is limited by transmission losses (horizontal parts of the curves). In reality, there is a metallic plate placed behind the substrate. If there are no resonances in the substrate transmission losses are strongly suppressed (Fig. 2.1b). However, a resonant background enhances the transmission losses. This has to be taken into consideration for substrates with very high permittivity like $SrTiO_3$ [21]. In the case of a metallic substrate (e.g. copper with a lead film) the superconducting film needs to be as thick as a few times λ_L in order to avoid a significant loss contribution from the substrate.

For planar resonators with film thicknesses in the order of λ_L the plane wave approximation is not fulfilled in the vicinity of edges. Therefore, the boundary value problem defined by the geometry of the particular planar resonator (e.g. microstrip resonator, see Subsection 3.1.4) needs to be solved taking into account the complex conductivity of a superconductor.

2.1.2 BCS approach

The strongest discrepancy between the prediction of Gorter and Casimir about the temperature dependence of the normal fluid density and experimental data for conventional superconductors was observed at temperatures below $T_c/2$. Here both $R_s(T)$ and $\delta\lambda_L(T) = \lambda_L(T) - \lambda_L(0)$ are determined by the energy gap according to $\exp(-\Delta/kT)$. Qualitatively, this temperature dependence becomes obvious in the two-fluid picture upon identifying the normal fluid with the thermally excited quasiparticles.

Within BCS theory the temperature dependence of λ_L at frequency zero is given by [22, 23]

$$\frac{1}{\lambda_L^2(T)} = \frac{1}{\lambda_L^2(0)}\left[1 - 2\int_{\Delta(T)}^{\infty} -\frac{\partial F(\epsilon)}{\partial\epsilon}\frac{\epsilon}{\sqrt{\epsilon^2 - \Delta(T)^2}}d\epsilon\right], \tag{2.16}$$

with $F(\epsilon)$ being the value of the Fermi function at ϵ. Eq. 2.16 holds true for the local limit, where the BCS coherence length ξ_0 is small in comparison to the mean free path l and λ_L. Except for a narrow range close to T_c, $\lambda_L(T)$ is independent of frequency for $\hbar\omega << \Delta$ and $\omega\tau << 1$ ($\tau = l/v_F$). For $T << T_c$ from Eq. 2.16 a more simple expression results [22]

$$\delta\lambda_L(T) = \lambda_L(T) - \lambda_L(0) = \lambda_L(0)\sqrt{\pi\Delta/2kT}\exp(-\Delta/kT) \tag{2.17}$$

which contains the expected $\exp(-\Delta/kT)$ dependence.

The complete theory of absorption of electromagnetic waves within BCS theory was worked out in 1958 by Mattis and Bardeen [24] and independently by Abrikosov, Gorkov, and Khalatnikov [25, 26]. These theories rely on a nonlocal relation between the current density and the vector potential, based on earlier ideas about the anomalous skin effect in normalconducting metals (see previous section). Computer programs to calculate the surface impedance in the framework of the Mattis-Bardeen theory for different values of l of the quasiparticles were worked out by Turneaure [28] and, independently, by Halbritter [29]. Moreover, Blaschke and Blocksdorf included strong electron-phonon coupling effects to calculate the surface impedance of Pb, Sn, and Nb [30]. The effects of smearing of the density of states due to gap anisotropy and impurity scattering were also considered by Blaschke et al. in order to fit surface resistance data of niobium over a wide frequency range [31].

It is beyond the scope of this review to discuss in detail these theories and their validity for the experimental results. However, it is useful to discuss the general dependences of Z_s on temperature, frequency, and mean free path. Zuccaro recently derived approximation formulas for σ_1/σ_n (σ_n is the conductivity in the normal state in the impurity scattering limit, i.e. scattering by phonons is negligible) for the local limit ($\lambda_L >> \xi_F$, see Eq. 2.24) and $\omega << 2\Delta/\hbar$ [32]. In the clean limit ($2\Delta/\hbar >> \tau^{-1}$ and $\omega\tau << 1$) the result is:

$$\frac{\sigma_1}{\sigma_n} = 2F(\Delta) - \frac{K}{2} + \left(1 - \tanh^2\left(\frac{\Delta}{2kT}\right)\right)\frac{\Delta}{2kT}\ln\frac{2}{\omega\tau} \tag{2.18}$$

Note that σ_1 shows an explicit dependence on the scattering rate τ^{-1}. For the dirty limit ($2\Delta/\hbar << \tau^{-1}$ and $\omega\tau << 1$) a similar result holds, which is independent of τ^{-1}:

$$\frac{\sigma_1}{\sigma_n} = 2F(\Delta) - K + \left(1 - \tanh^2\left(\frac{\Delta}{2kT}\right)\right)\frac{\Delta}{2kT}\ln\frac{8\Delta}{\hbar\omega} \tag{2.19}$$

In Eqs. 2.18 and 2.19 the quantity K is a converging sum given by:

$$K = 16kT\Delta^2\sum_{j=0}^{\infty}\frac{\omega_j\arctan(\omega_j/\Delta) - \Delta/2}{(\omega_j^2 + \Delta^2)^2} \quad \text{with} \quad \omega_j = (2j+1)\pi kT \tag{2.20}$$

For $T \leq 0.2\,T_c$ the value of the Fermi function F and K are negligible resulting in simple expressions for σ_1

$$\frac{\sigma_1}{\sigma_n} = \frac{2\Delta}{kT}\ln\left(\frac{2}{\omega\tau}\right)\exp(-\Delta/kT) \tag{2.21}$$

for the clean limit and

$$\frac{\sigma_1}{\sigma_n} = \frac{2\Delta}{kT}\ln\left(\frac{8\Delta}{\hbar\omega}\right)\exp(-\Delta/kT) \tag{2.22}$$

for the dirty limit, respectively. Experimentally, at temperatures below $T_c/2$, $R_s(T)$ of many classical superconductors exhibits an $\exp(-\Delta/kT)$ dependence according to Eqs. 2.14, 2.21, and 2.22, which is limited to low temperatures by a temperature independent residual surface resistance. As a result of strong electron-phonon coupling, for many superconductors Δ/kT_c is above the BCS value of 1.76, e.g. about 1.85 for niobium [31] and about 2.2 for Nb_3Sn [33]. Therefore, precise measurements

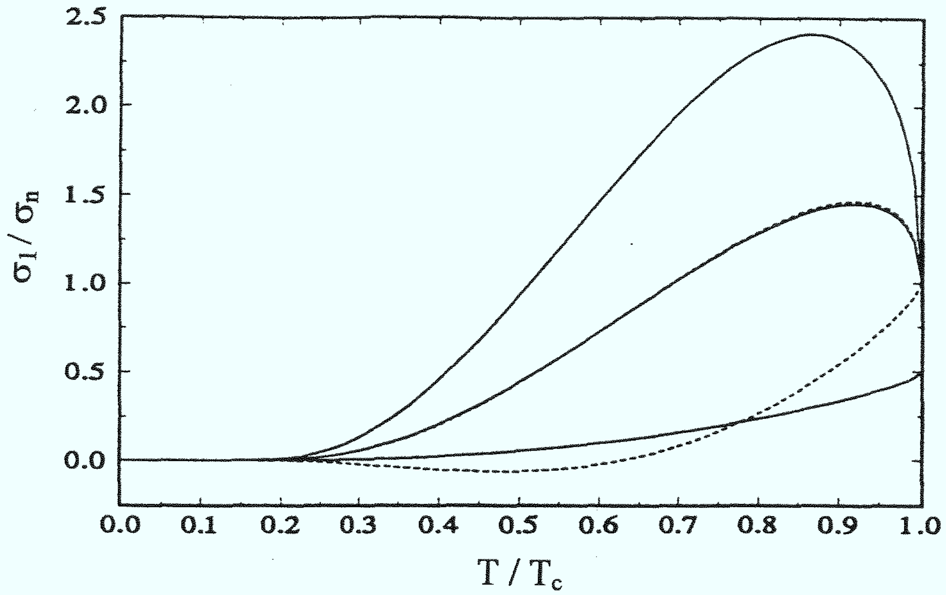

Fig. 2.2: Numerical BCS calculations in the local limit (solid lines) of the temperature dependence of σ_1/σ_n for angular frequencies $\omega = 10^9, 10^{10}, 10^{11}$ s^{-1} (from top to bottom) and approximative results according to Eqs. 2.18 and 2.19 (dotted lines) using $T_c = 92$ K, $\tau = 10^{-11}$ s, and $2\Delta/kT_c = 3.53$ (from [32]).

of $R_s(T)$ as well as $\delta\lambda_L(T)$ can be used to determine the value of the energy gap. The observed frequency dependence of R_s of classical superconductors deviates from an f^2 dependence according to the logarithmic divergence in Eqs. 2.21 and 2.22. The physical explanation (in the clean limit) is that at photon energies approaching Δ the net absorption rate for photons goes down, as the interacting quasiparticle is pushed by an energy amount $\hbar\omega$ away from the singularity in the BCS density of states due to the absorption of a photon. Above the singularity in the density of states the density of unoccupied states decreases continuously, leading to a reduced absorption.

It is worthwhile to discuss the temperature dependence of σ_1 close to T_c. According to Fig. 2.2 $\sigma_1(T)$ first increases from σ_n at T_c upon lowering the temperature. At about $0.9\,T_c$ $\sigma_1(T)$ exhibits a pronounced maximum which decreases in amplitude with increasing frequency. The absence of this so-called "coherence peak" or "Hebel-Slichter peak" in $\sigma_1(T)$ of HTS (see Section 4.2) can be interpreted as an indication of the invalidity of BCS theory for HTS. However, according to Marsiglio et al. [34] the coherence peak is suppressed for strong electron-phonon coupling. The physical reason is that in strong-coupling theory the phonons initiate pair breaking at elevated temperatures, which smears out the gap structure in the density of states (see Section 2.2.2).

The dependence of the surface impedance on the mean free path out of the local limit, however, is not straightforward. In contrast to the frequency and temperature dependences, $Z_s(l)$ is dominated by the momentum dependence of the absorption matrix element. An approximation formula for the penetration depth derived by nonlocal theory was given by Halbritter [35],

$$\lambda_L(T,l) \approx \lambda_L(T,\infty)\sqrt{1+\frac{\xi_F(\infty)}{l}} \tag{2.23}$$

which exhibits good agreement with experimental results [23]. The coherence length ξ_F also exhibits a mean free path dependence according to

$$\xi_F^{-1}(l) = \xi_F^{-1}(\infty) + l^{-1}. \tag{2.24}$$

The quantity ξ_F is related to the BCS coherence length ξ_0 by:

$$\xi_F(\infty) = \pi\xi_0/2 = \frac{\hbar v_F}{2\Delta} \tag{2.25}$$

According to Halbritter [35] the observed dependences of R_s on l can be described by:

$$R_s \propto \frac{\lambda(l)}{\xi_F(l)} \frac{1}{\sqrt{\hbar\omega/2\Delta + (\xi_F(l)/l)^2}}. \tag{2.26}$$

By introducing $x = \xi_F(\infty)/l$ and using Eqs. 2.23 and 2.24, Eq. 2.26 can be rewritten as

$$R_s \propto \frac{(1+x)^{3/2}}{\sqrt{\frac{\hbar\omega}{2\Delta} + (\frac{x}{1+x})^2}}. \tag{2.27}$$

Neglecting $\hbar\omega/2\Delta$ in Eq. 2.27, R_s exhibits a minimum at $x = 2/3$, which is shifted to smaller values of x for higher frequencies. Such minima have indeed been observed experimentally for a Pb-Bi alloy [23] and for niobium [36]. For HTS the mean free path is much larger than the coherence length, i.e. $x \to 0$. In this case R_s turns out to be proportional to x^{-1}. This corresponds to the prediction of the two-fluid model (Eq. 2.14). However, the τ dependence of σ_1 for the clean limit (Eq. 2.18) is not apparent in this approximation formula. Therefore numerical calculations are essential in order to describe experimental data properly.

2.2 Oxide superconductors

Since the discovery of superconductivity in oxide materials by Bednorz and Müller in 1986 [37] the investigation of the electrodynamic properties of these new materials has become important for two reasons. First, the question about the pairing mechanism and the pairing state of the superconducting ground state is still open ([38, 39] and references therein). In particular, pairing states with angular momentum not equal to zero would strongly affect the density of states, and thus the electrodynamic response (see Section 2.2.3). Secondly, according to the statement by Halbritter: "Defects define material" [40], the procedures for optimizing thin films for applications in microwave technology have received important input from Z_s investigations.

It is beyond the scope of this review to emphasize structural and electronic properties of the different HTS materials. Here only some relevant properties which are likely to be related to the peculiar microwave response are summarized. One common feature of all HTS cuprates is the quasi-two-dimensional character of the structural and electronic properties (for a review see [41, 42, 43] (structural properties) and [8] (electronic, normal-state and superconducting properties). The most important structural elements are CuO_2 planes (oriented parallel to the crystallographic *ab*-plane) which are separated by oxide layers providing charge carrier doping of the CuO_2 planes. The undoped cuprates (e.g. $YBa_2Cu_3O_{7-x}$ with $x = 1$) are antiferromagnetic insulators. Antiferromagnetism is due to electrons orginating from the $3d_{x^2-y^2}$ orbitals of copper and the $2p_{x/y}$ orbitals of oxygen in the CuO_2 planes. The metallic behavior and superconductivity is attained by doping the CuO_2 planes either with holes (*p*-type) or electrons (*n*-type). As an example, for $YBa_2Cu_3O_{7-x}$ hole-doping is achieved by oxygen loading. The additional oxygen atoms form copper-oxygen chains, which are entirely free of oxygen vacancies at $x = 0$. At $x \approx 0.12$ a maximum in T_c of 93 K is attained in $YBa_2Cu_3O_{7-x}$. Upon approaching $x = 0$ (overdoped regime) T_c drops slightly [44, 45]. In other HTS cuprates, e.g. $Tl_2Ba_2CuO_6$, overdoping is possible until T_c approaches zero [46].

As discussed in [8], it is now generally accepted that the metallic (=doped) state of the cuprates can be characterized as a quasi-two-dimensional Fermi liquid. The Fermi surface of the *p*-type cuprates is almost cylindrically shaped with a nearly quadratic cross section within the *ab*-plane [9]. In contrast to conventional metals, the Fermi energy and the Fermi velocity are as small as about 0.1 eV and 10^5 m/s, respectively [8]. However, due to the flatness of the energy bands at the level of the Fermi energy [9] the density of states at the Fermi level is quite high.

The normal-state properties are characterized by a linear temperature dependence of the resistivity ρ at optimum doping which becomes quadratic in the overdoped region [46, 47, 48]. The absolute ρ values are quite high in comparison to conventional metals. In the case of $YBa_2Cu_3O_{7-x}$ with $x \to 0$ the resistivity for currents parallel to the CuO_2 planes $\rho_{ab}(100K)$ is about 40 to 50 $\mu\Omega$cm [48]. The resistivity perpendicular to the CuO_2 plane $\rho_c(100K)$ about a factor of 40 larger [49]. This anisotropy is much higher for HTS compounds like $Bi_2Sr_2CaCu_2O_8$ with a larger CuO_2 plane-plane separation. Depending on the oxygen content of the BiO_2 planes a semiconducting $\rho(T)$ behavior and an intrinsic Josephson coupling of adjacent CuO_2 layers in the superconducting state was observed [50].

The superconducting state of the cuprates is characterized by large values of the London penetration depth. For $YBa_2Cu_3O_7$ $\lambda_{L,ab} \approx 140$ to 180 nm (e.g. [51]) and a factor of 5 larger in c-direction [52]. The coherence length $\xi_{F,ab}$ is 1.6 nm and only about 0.3 nm in c-direction [14]. These small values are due to the high critical temperature and the small Fermi velocity (Eq. 2.25 and [8]). There are two consequences of the small coherence length for the electrodynamic response. First, since $\lambda_L >> \xi_{F,ab}$ and mean free path l, the local limit is valid leading to a simplified description of the electrodynamic response within extended BCS approaches (see Subsection 2.2.2). Even for very clean samples with l being large in comparison to λ_L, effects from a nonlocal current-field relation are considered to be negligible due to the quasi-two-dimensional nature of the cuprates [53]. Secondly, as a consequence of the short coherence length the electrodynamic response turns out to be extremely sensitive to granularity.

To date, there is an ongoing controversy about the mechanism of superconductivity in the cuprates. On the one hand, the electron-phonon interaction may explain superconductivity, but the simple BCS approach is insufficient [8]. In Subsection 2.2.2 the results of theoretical approaches considering two-band behavior and inelastic electron-electron scattering due to a nested Fermi surface are reviewed. On the other hand, among the large number of suggested new mechanisms to date the antiferromagnetic spin fluctuation mechanism based on the antiferromagnetic nature of the undoped cuprates, as introduced by Schrieffer [54] and Monthoux [55], has been worked out in detail concerning predictions for Z_s. In particular, the consequences of a d-wave pairing state, which is suggested to result from superconductivity initiated by spin fluctuations, will be stressed in Subsection 2.2.3.

2.2.1 Phenomenological models

As described in detail in Chapter 4, the most striking discrepancy between the electrodynamic response of oxide and conventional superconductors is the occurrence of a high level of residual absorption. This means that except for the initial drop of $R_s(T)$ just below T_c due to the strong temperature dependence of λ_L (see Eq. 2.14) $R_s(T)$ exhibits a very weak temperature dependence and remains on a high level (in comparison to e.g. niobium) down to the lowest temperatures. The most simple explanation is to assume that the HTS compounds contain two conducting subsystems, with one of them remaining normal-conducting below T_c [56]. Assuming a temperature-independent mean free path for the normal-conducting component at $T << T_c$, a temperature-independent residual surface resistance $R_{res} = 1/2\, \omega^2 \mu_0^2 \sigma_1 \lambda_L^3(0)$ results according to Eq. 2.14 with $\sigma_1 = constant$.

There is evidence that in $YBa_2Cu_3O_{7-x}$ such an intrinsically normal-conducting subsystem is formed by the copper oxygen chains, whereas the CuO_2 planes are intrinsically superconducting: In untwinned $YBa_2Cu_3O_{7-x}$ single crystals, i.e. crystals where the CuO chains (aligned along the b-direction) are oriented in one direction throughtout the entire crystal), the normal-state resistivity [57], the plasma edge in optical absorption [45, 59], and the far-infrared reflectivity in the superconducting state [58] exhibit a strong ab-anisotropy. However, since $YBa_2Cu_3O_{7-x}$ exhibits metallic behavior in c-direction it becomes obvious that the interaction between the normal and superconducting subsystems cannot be neglected. First Tachiki and Takahashi [60, 61], and more recently, Liu and Klemm [62, 63] calculated the density of states of a two-band system allowing proximity coupling between the two systems. The main effect concerning the electrodynamic response is that below the energy positions of the peaks at $\epsilon = \pm\Delta$ the density of states remains finite down to the Fermi energy ($\epsilon = E - E_F = 0$). This may explain the occurrence of a finite tunneling conductivity at zero-bias voltage, as typically observed in tunneling experiments with $YBa_2Cu_3O_{7-x}$ [64]. As explained in Section 2.2.2, induced superconductivity in a normal-conducting subsystem can also lead to a finite energy gap in the density of states. For this "induced energy gap" the value of Δ/kT_c is much smaller than 3.52, as prediced by BCS theory (see Section 2.1.2). However, in this case only a small amount of magnetic impurities is required to obtain gapless behavior in the induced superconducting subsystem (see Section 2.2.2).

The effect of gaplessness on the temperature dependence of the complex conductivity of a superconductor will be analyzed within a phenomenological model. First, the temperature dependence of σ_2 can be calculated according to Eqs. 2.12 and 2.16:

$$\kappa(T) = \frac{\sigma_2(0) - \sigma_2(T)}{\sigma_2(0)} = -2\int_0^\infty \frac{\partial F(\epsilon)}{\partial \epsilon} D(\epsilon) d\epsilon \tag{2.28}$$

At $T << T_c$ $\kappa(T) \approx 2\delta\lambda_L(T)/\lambda_L(0)$ is dominated by low-energy excitations, i.e. by those parts of the density of states for which $\epsilon << \Delta$. Assuming $D(\epsilon) = A\epsilon^n$ with $n = 0, 1, 2, \ldots$ a power law behavior of $\kappa(T)$ results from Eq. 2.28:

$$\kappa(T) = Ac(n)(kT)^n \quad \text{with} \quad c(n) = \frac{1}{n}\int_1^\infty \frac{(\log(x))^{n-1}}{(1+x)x} dx, \quad n = 1, 2, 3\ldots \tag{2.29}$$

The quantities $c(n)$ are numerical constants with $c(0) = 1$ and $c(1) = 0.693$. The real part of the conductivity, however, is related to the density of states according to Fermi's Golden Rule [23]:

$$\frac{\sigma_1(T)}{\sigma_n} = \frac{2}{\hbar\omega}\int_0^\infty (F(\epsilon) - F(\epsilon + \hbar\omega))D(\epsilon)D(\epsilon + \hbar\omega)d\epsilon \approx -2\int_0^\infty \frac{\partial F(\epsilon)}{\partial \epsilon} D^2(\epsilon) d\epsilon \tag{2.30}$$

In Eq. 2.30 the effects of direct quasiparticle excitation by the high-frequency photons are neglected, which appears to be justified at temperatures for which $\hbar\omega << kT$. Within this approximation σ_1 remains frequency-independent (at $T << T_c$) according to the second expression in Eq. 2.30. Inserting $D(\epsilon) = A\epsilon^n$ in Eq. 2.30 results in a power law behavior of σ_1 with an exponent twice as large as for $\kappa(T)$:

$$\frac{\sigma_1(T)}{\sigma_n} = A^2 c(2n)(kT)^{2n}, \quad n = 1, 2, 3, \ldots \tag{2.31}$$

In the case of $n = 0$, both σ_1 and σ_2 become temperature-independent and finite at $T = 0$. This situation corresponds to a temperature independent normal fluid remaining at $T \to 0$. For $n > 0$ σ_1 and σ_2 exhibit a different temperature behavior. The case $n = 1$ is of particular interest, as it corresponds to the prediction for a d-wave pairing state (see Subsection 2.2.3). Here σ_2 exhibits a linear and σ_1 a quadratic temperature dependence. It is furthermore interesting to consider the case $D(\epsilon) = A + B\epsilon^n$ ($n > 0$), which roughly corresponds to the density of states for normal and superconducting subsystems in proximity contact in the presence of magnetic pair breaking (see Subsection 2.2.2):

$$\kappa(T) = A + Bc(n)(kT)^n \quad \text{and} \quad \frac{\sigma_1(T)}{\sigma_n} = A^2 + 2ABc(n)(kT)^n + B^2c(2n)(kT)^{2n} \tag{2.32}$$

For the case $A >> B/(kT)^n$ the temperature dependence of $\sigma_1(T)$ is dominated by T^n, as for κ. In turn, the observation of similar T dependences for σ_1 and κ indicates a high value of the density of states at the Fermi energy.

Until now, only the low-temperature region of the surface impedance has been discussed. Due to the high critical temperatures of the oxide superconductors the scattering rate of the quasiparticles τ_q^{-1} is expected to be temperature dependent below T_c. This is simply a consequence of the fact that the normal-state resistivity decreases with decreasing temperature down to T_c. Bonn et al. first suggested to fit the experimental data by [65]

$$\sigma(\omega, T) = \frac{1}{\omega\mu_0\lambda_L^2}[\frac{n_q(T)\tau_q(T)\omega}{1 - i\omega\tau_q(T)} + in_s(T)] \tag{2.33}$$

with $n_q(T)$ being the temperature-dependent normalized density of the quasiparticles and $n_s(T)$ the normalized density of superconducting charge carriers. This ansatz contains a Drude-type conductivity for the quasiparticles. In addition to Eqs. 2.11 and 2.12, Eq. 2.33 contains a high-frequency correction describing the relaxation of the quasiparticles, similar to Eq. 2.7. Bonn et al. used Eq. 2.33 to determine τ_q^{-1} from $\sigma_1(T)$ and $\sigma_2(T)$ measured at one frequency, assuming the validity of the normalization condition $n_q(T) + n_s(T) = 1$ from the two-fluid model. However, according to the dependences of σ_1 and σ_2 on the density of states, as discussed in the last paragraph, the normalization condition does not hold true and therefore this analysis may lead to wrong $\tau_q^{-1}(T)$ dependences at $T << T_c$. In particular, it is impossible to estimate the elastic impurity limit $\tau_q^{-1}(T \to 0K)$ of the scattering rate by this analysis.

Alternatively, $\tau_q^{-1}(T)$ can be determined from $\sigma_1(T)$ without utilizing the normalization condition if data sets at two different frequencies ω_1 and ω_2 are available. According to Eq. 2.33 the ratio $\sigma_1(\omega_1, T)/\sigma_1(\omega_2, T)$ is independent of $n_q(T)$ [66]:

$$\frac{\sigma_1(\omega_1, T)}{\sigma_1(\omega_2, T)} = \frac{1 + \omega_2^2\tau^2(T)}{1 + \omega_1^2\tau^2(T)} \tag{2.34}$$

It needs to be emphasized that Eq. 2.33 is not based on microscopic calculations. However, this model exhibits very good agreement with experimental results and is very intuitive for understanding the dependence of the measured surface impedance on the scattering rate (see Sections 4.1 and 4.2).

In addition to intrinsic properties of the cuprates, which may explain the experimental results on the surface impedance, possible extrinsic sources of microwave losses will be discussed. The most-simple-to-describe kind of imperfection are normal-conducting inclusions with conductivity $\sigma_{n,i}$ and volume fraction A. These inclusions lead to an additional conductivity $\sigma_1 = \alpha\sigma_{n,i}$ according to the two-fluid model. This simple expression holds true for the case that the typical dimensions of the inclusions are large in comparison to the coherence length and small in comparison to λ_L. The first condition guarantees that the proximity effect does not reduce the volume fraction A. If the size of the inclusions comes in the order of λ_L, the penetration depth of the electromagnetic field will be enhanced in the vicinity of the inclusions. This was modelled theoretically by Walker and Scharnberg by assuming uniaxially superconducting grains embedded in a normal-conducting background using an effective medium approach [67]. The main result was that the additional conductivity due to the inclusions can be significantly larger than $\alpha\sigma_{n,i}$.

The effects of residual granularity on the surface impedance was first worked out within a weak-coupling grain model by Hylton et al. [68] and others (for a review see [69]). It is well established that grain boundaries in HTS exhibit weak-link behavior. Grain boundary Josephson junctions, which are nowadays widely used for artificial Josephson devices, exhibit current-voltage characteristics in good agreement with the predictions of the RSJ (resistively shunted Josephson junction) model [16]. Within this model the most important parameters determining each Josephson junction are the critical current density j_c and the product of critical current I_c and shunt resistance R. In the case of grain boundaries with grains aligned parallel to their c-axis and tilted by an angle θ within the ab-plane, j_c and I_cR were found to depend strongly on θ. In particular, in the case of $YBa_2Cu_3O_{7-x}$ films at $T = 4.2\,K$, j_c decreases with increasing θ from the bulk value of up to $5 \cdot 10^7\ A/cm^2$ at $\theta \approx 0°$ by about 4 orders of magnitude at $\theta = 45°$ [16]. The maximum I_cR values attained at small θ values are about 10 millivolts [15, 70].

Hylton et al. [68] assumed that HTS films can be modeled as a network of grain boundaries with an average lateral dimension a of each grain. In this model the additional surface resistance due to losses generated by the current across the resistive shunts of the junction is given by:

$$R_s(T, H_{rf}) = \omega\mu_0\lambda_{eff}(T)\left(\frac{\lambda_J(T)}{\lambda_{eff}(T)}\right)^2 \frac{\hbar\omega}{4eI_c(T)R}[1 + (\frac{j_{rf}}{j_c(T)})^2] \tag{2.35}$$

In Eq. 2.35 H_{rf} is the high-frequency magnetic field, which in cavity resonators (see Section 3.1.1) is related to the high-frequency current density j_{rf} at the surface of the superconductor by $j_{rf} = H_{rf}/\lambda_{eff}(T, j_{rf})$. The quantity λ_{eff} is the effective penetration depth, which is related to the London penetration depth λ_L as well as to

λ_J, which is the effective continuum penetration depth due to the network of grain boundary junctions alone:

$$\lambda_{eff}(T, H_{rf}) = \sqrt{\lambda_L^2(T) + \lambda_J^2(T, H_{rf})} \qquad (2.36)$$

with

$$\lambda_J(T, H_{rf}) = \sqrt{\frac{\hbar}{a2ej_c(T)\mu_0}[1 - (\frac{j_{rf}}{j_c(T)})^2]}$$

In Eqs. 2.35 and 2.36 the term in parantheses was introduced by Nguyen et al. [71] to describe the H_{rf} dependence of the surface impedance at rf current densities being small in comparison to the critical current density j_c of the Josephson junction.

For high-quality epitaxial films of $YBa_2Cu_3O_{7-x}$ large angle grain boundaries can be avoided. However, due the ab-twinning in $YBa_2Cu_3O_{7-x}$ films small angle grain boundaries with $\theta \approx 1.5°$ remain at average distances of 50 to 100 nm [48]. Assuming $j_c = 3 \cdot 10^7$ A/cm^2, I_cR approaching the Amgeakar-Baratoff limit $(I_cR)_{max} = \pi\Delta/2e \approx 30$ mV($\Delta = 20$ mV), and $a = 100$ nm $\lambda_J = 90$ nm results. This leads to $\lambda_{eff} = 170$ nm according to Eq. 2.36, assuming $\lambda_L = 140$ nm. From Eq. 2.35 a surface resistance of 1.4 $\mu\Omega$ at 10 GHz results. This is already a considerably high value in comparison to niobium with minimum R_s values in the $10^{-9}\ \Omega$ range. However, it is not clear yet whether twin boundaries exhibit weak link behavior at all. Another type of imperfection in $YBa_2Cu_3O_{7-x}$ thin films which may be responsible for granularity are antiphase boundaries resulting from the spiral growth around a dislocation [72]. Typically, antiphase boundaries are located at the edges of adjacent growth spirals which are about 100 nm in diameter [73, 74]. If the film is grown on a single crystalline cubic substrate with a lattice constant being about one third of the c-axis lattice parameter of $YBa_2Cu_3O_{7-x}$ (e.g. $SrTiO_3$), two adjacent growth spirals may nucleate on two different terraces of the substrate surface. Such terraces are due to the finite misorientation (with respect to a crystallographic axis) of the substrate surface. Therefore, two adjacent $YBa_2Cu_3O_{7-x}$ growth spirals are often dislocated by $nc/3$, $n = 1, 2, 3, \ldots$ in c-direction, giving rise to antiphase boundaries. In this case the microwave losses should be of the same order as for the twin boundaries. According to Eqs. 2.35 and 2.36, the temperature dependence of the surface impedance is determined by $j_c(T)$. For grain boundary junctions $j_c \propto 1 - (T/T_c)^\alpha$ holds true with A ranging between 1 (at $T << T_c$) and 2 (close to T_c) [15, 75]. Hence the slope of $Z_s(B_{rf})$ increases strongly with temperature.

The situation becomes more complicated if H_{rf} exceeds the magnetic field level at which vortices begin to penetrate into the Josephson junctions or into the bulk (extrinsic or intrinsic H_{c1}). Sridhar et al. [76] first applied Bean's model [13] to calculate the surface resistance as a function of rf power. This model is applicable for planar transmission line structures (see Subsection 3.2.4), where j_{rf} is strongly enhanced at the edges (usually prepared by photolithography) of the employed thin film. If j_{rf} exceeds j_c (i.e. H_{rf} exceeds H_{c1}) at an edge, vortices are created and pinned (see Subsection 2.2.4). Upon further increasing the microwave power the region with $j_{rf} = j_c$ (current-induced critical state) propagates from the edge towards the inner part of the film. As the result of this analysis R_s increases quadratically with magnetic field up to about a few hundred Oerstedt and stronger above, in qualitative agreement with experimental data (see Section 4.5) In contradiction to the predictions from the weak-coupling grain model (Eq. 2.35) here $R_s(H_{rf}) - R_s(0)$ scales linearly with frequency.

2.2.2 Extended BCS approaches

In order to tailor microscopic calculations in the framework of BCS theory to the superconducting cuprates, several pecularities need to be taken into account. First, according to photoemission data on $Bi_2Sr_2CaCu_2O_8$ the Fermi surface for electron states with momentum parallel to the *ab*-plane is square-like (Fig. 2.3) [9] leading to a strong enhancement of the inelastic electron-electron scattering rate in comparison to a circular Fermi surface. The reason for this enhancement is that all scattering processes are allowed which involve electron momentum states $\vec{k}$ before and $\vec{K}$ after the collision, for which $\vec{Q} = \vec{k} - \vec{K}$ is equal to the diagonal of the Fermi surface (nesting condition). Rieck et al. calculated the normal and superconducting properties of a nested Fermi liquid (NFL-theory) [10, 77]. This theory yields a linear temperature dependence of the resistivity and a quasilinear decrease of the infrared reflectivity with frequency, as observed experimentally for $YBa_2Cu_3O_{7-x}$ [10]. The dominance of electron-electron scattering within the NFL theory also determines the microwave conductivity in the superconducting state. Due to the decrease of the density of quasiparticles below T_c the quasiparticle scattering rate τ_q^{-1} drops

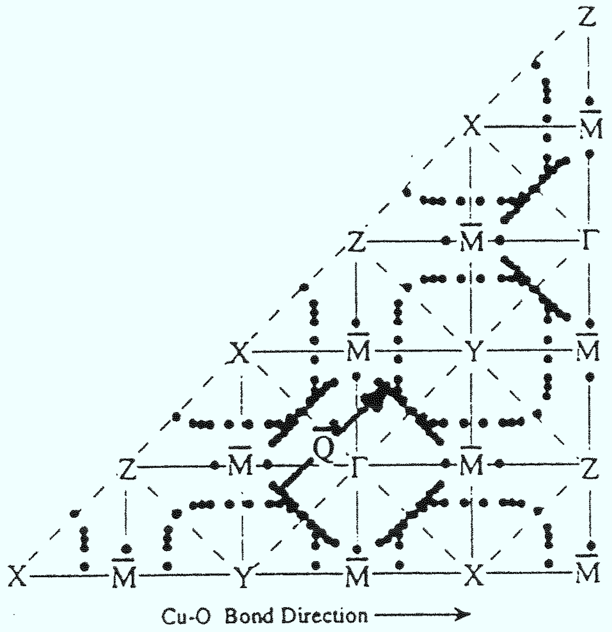

Fig. 2.3: Fermi surface of $Bi_2Sr_2CaCu_2O_{8+\delta}$ as determined from angle resolved photoemission data. The nesting vector $\vec{Q}$ is indicated as an arrow (from [9]).

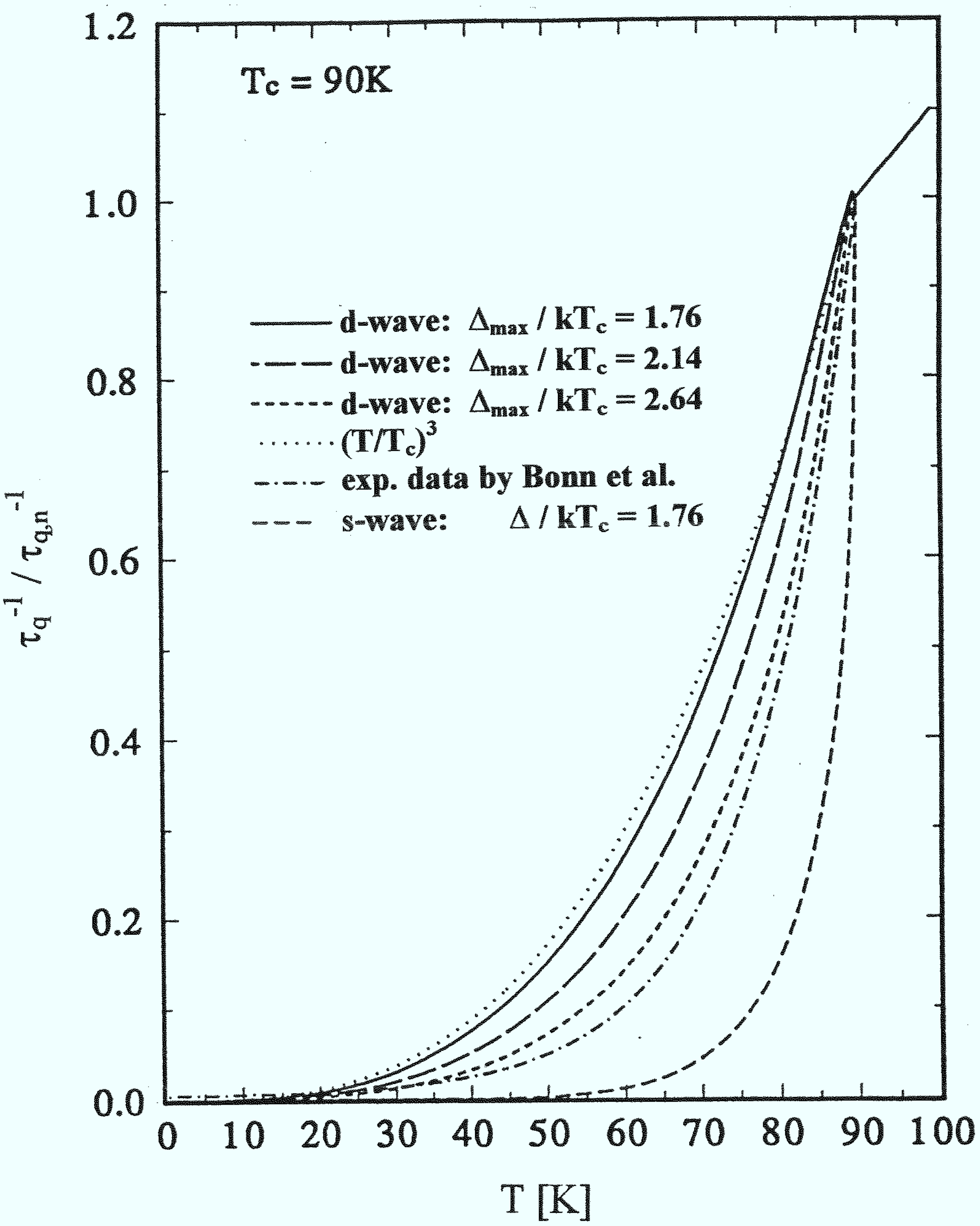

Fig. 2.4: Quasiparticle scattering rate (normalized to its value $\tau_{q,n}^{-1}$ above T_c) due to electron-electron scattering calculated within nested Fermi liquid theory for an isotropic *s*-wave order parameter with $\Delta/kT_c = 1.76$ (weak coupling) and a *d*-wave order parameter with different Δ/kT_c values, in comparison to experimental data by Bonn et al. [65] (see Section 4.2). For comparison, a T^3 dependence, which is typical for phonon scattering, is given (from [77]).

rapidly (Fig. 2.4). The steepness of this drop depends on the symmetry of the order parameter and the values of the reduced energy gap Δ/kT_c. For d-wave symmetry a more moderate decrease of τ_q with temperature results, because the quasiparticles with $\vec{k}$-vectors close to the directions of the nodes (see Subsection 2.2.3) have a very small pairing energy and therefore contribute to inelastic scattering processes down to very low temperatures. According to Fig. 2.4 the d-wave results are in better agreement with the experimental data discussed in Section 4.2 (however, for a strongly anisotropic s-wave order parameter with Δ_{min} close to zero in at least one direction of momentum space the results are supposed to be similar to d-wave). Similar results for the temperature dependence of the quasiparticle scattering rate below T_c were obtained by Quinlan et al. [11] using a model based on spin fluctuation scattering, which inherently leads to a d-wave superconductivity (see Subsection 2.2.3). The main consequence of the rapid drop of τ_q^{-1} for the electrodynamic properties is a pronounced maximum in $\sigma_1(T)$, which results from the competition of the increasing quasiparticle lifetime with the decreasing quasiparticle density (Eq. 2.33). This is in strong contrast to classical superconductors.

The layered structure of the oxide superconductors gives rise to another peculiarity of the electrodynamic response. In the case of $YBa_2Cu_3O_{7-x}$ the normal-conducting subsystem formed by the CuO chains (see Subsection 2.2.1) may become superconducting. According to a theory by Kresin and Wolf in the framework of strong-coupling BCS theory a superconducting state can be induced into the chains by the proximity effect and phonon mediated charge transfer from the CuO_2 planes to the CuO chains [81, 82]. The parameters of these calculations are the electron-phonon coupling constants Λ_i, $i = a, b$ for subsystems a and b with $\Lambda_b = 0$, i.e. the subsystem b is intrinsically normal-conducting. The phonon-mediated charge transfer is described by a coupling constant $\Lambda_{a,b}$ and the internal proximity effect is determined by the overlap of the wave functions $\Psi_{a,b}$ in a and b. Finally, also the ratio of the densities of states $\alpha = D_b/D_a$ above T_c of both subsystems turns out to have a strong effect on the normalized density of states in the superconducting state.

For a detailed discussion of the results the reader is referred to a recent issue of the monographs in Physics [8] and references therein. Here only the influence of the relevant parameters on the density of states and the consequences for the electrodynamic response will be discussed on a qualitative level. As the most important result, both coupling channels lead to a finite energy gap Δ_b in the density of states of both subsystems, which is smaller than the energy gap Δ_a of subsystem a without interaction between the two subsystems (Fig. 2.5a,b). This implies a dominant $\exp(-\Delta_b/kT)$ low temperature dependence of $R_s(T)$ and $\Delta\lambda_L(T)$. This is in contradiction to the results of Tachiki and Takahashi [83] and of Klemm et al. [63], where the intrinsically normal-conducting subsystem always gives rise to a finite density of states down to $\epsilon = 0$.

In the density of states of subsystem a the peak at $\epsilon = \Delta_a$ only moves slightly to lower energies upon increasing either $\Lambda_{a,b}$ or $\Psi_{a,b}$, but the density of states of subsystem a remains finite down to Δ_b (Fig. 2.5a at $T = 10$ K and Fig. 2.5b with $\Gamma_m = 0$). In contrast, the density of states of subsystem b exhibits a strong peak at

Δ_b and a shoulder at Δ_a. The value of Δ_b increases from zero both with increasing $\Lambda_{a,b}$ and $\Psi_{a,b}$. Upon increasing A, the spectral weight of the density of states of system a is shifted from the peak at Δ_a to the energy range between Δ_b and Δ_a. For the density of states of system b, only the height of the peak at Δ_b decreases. This is important since the occurrence/nonoccurrence of a double peak structure in tunneling experiments for $YBa_2Cu_3O_{7-x}$ and $YbBa_2Cu_3O_7$ [64, 79, 84] may reflect the different density of states for the CuO chains and the CuO_2 planes. In contrast, the effect on T_c is the opposite for the two coupling channels. The proximity channel decreases T_c whereas the phonon-mediated charge transfer channel increases T_c due to an increase of phase space for electron-phonon interaction.

Fig. 2.5a,b shows the effects of finite temperature and magnetic impurities localized in subsystem b on the density of states of both subsystems. The magnetic impurities are characterized by a magnetic scattering rate Γ_m. Obviously, Δ_b is reduced upon increasing the magnetic scattering rate without strongly affecting the density of states of subsystem a. At an impurity concentration where T_c has practically not changed, the density of states of both subsystems becomes gapless. In the case of $YBa_2Cu_3O_{7-x}$, pair breaking in the CuO chains is expected as a result of oxygen vacancies. Kresin and Wolf estimated an oxygen deficiency of $x \approx 0.15$ for gapless behavior [82]. At such low oxygen deficiencies the critical temperature of $YBa_2Cu_3O_{7-x}$ is still about 90 K. According to Fig. 2.5a gaplessness also results from pair breaking by phonons at finite temperatures. Adrian et al. [85] performed calculations of the penetration depth as a function of Γ_m. At $\Gamma_m = 0$, $\delta\lambda_L$ exhibits an $\exp(-\Delta_b/kT)$ behavior at $T << T_c$ which is converted to a linear and subsequently to a quadratic behavior upon increasing the concentration of magnetic impurities. As will be discussed in Section 4.3, this may explain the experimental results for $YBa_2Cu_3O_{7-x}$ at different values of the oxygen deficiency x.

Fig. 2.5c shows the real part of the conductivity as a function of temperature for different frequencies (in units of temperatures) at $\Gamma_m = 0$. Note that the coherence peak apparent in Fig. 2.2 is not present as a result of pair breaking by phonons. The physical origin of the maximum is the decrease of the phonon scattering rate below T_c. Upon increasing Γ_m the height of the peak decreases as a result of an increasing temperature-independent scattering rate, as expected from the modified two-fluid model of Bonn et al. (Eq. 2.33). The density of state effects apparent in Fig. 2.4a, however, only affect the $\sigma_1(T)$ behavior at $T << T_c$. In particular, in the gapless state a residual conductivity occurs as a result of the finite density of states at the Fermi energy (see Eq. 2.32).

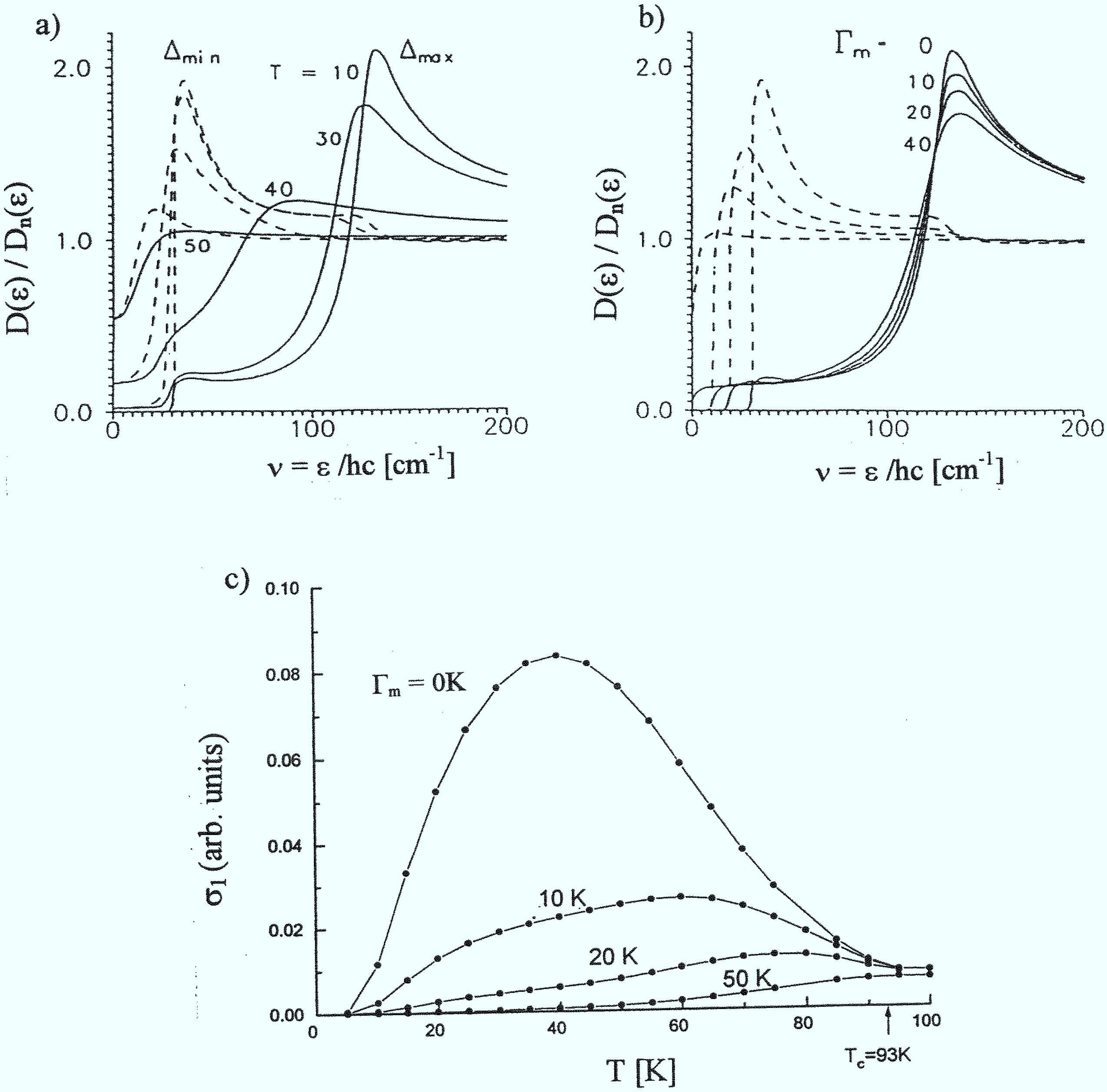

Fig. 2.5: Normalized (with respect to the normal-conducting state) density of states in the two-band model, calculated by Golubov (a and b) [78]. Fig. 2.5a shows the density of states for Γ_m=0 (Γ_m in units of temperatures, i.e. devided by k) at different temperatures, Fig. 2.5b at T =10 K and different Γ_m values. The solid and dashed lines represent the densities of states of the charge carriers localized in the CuO$_2$ planes CuO chains, repectively. The energy scale is given in units of wavenumbers. The fixed parameters of these computations are $\Lambda_a = 3$, $\Lambda_b = 0$, $\Lambda_{a,b}$ =0.5, and $\alpha = 1$. This selection of parameters leads to T_c =93 K, density of states peak positions $2\epsilon_{p,a}/kT_c = 5.6$ and $2\epsilon_{p,b}/kT_c = 1.0$, respectively, in good agreement with tunneling data for YBa$_2$Cu$_3$O$_{7-x}$ [79]. The real part of the conductivity (c) was calculated for f = 3 GHz by Golubov [80].

2.2.3 *d*-wave pairing state

The most important features of the electrodynamic response of superconductors with $d_{x^2-y^2}$ symmetry of the order parameter can be understood within the phenomenological models presented before taking into account the calculated density of states $D(\epsilon)$ for $d_{x^2-y^2}$ pairing. Similar to the s-wave (=BCS-like) density of states there is a peak at the maximum of the order parameter $|\Delta_{max}|$ along the Fermi surface. However, the most striking descrepancy from the s-wave is a linear $D(\epsilon)$ behavior for $\epsilon << \Delta_{max}$ given by $D(\epsilon) = \epsilon/\Delta_{max}$ (Fig. 2.6). According to Eqs. 2.29 and 2.31 this leads to a linear T dependence of $\delta\lambda_L$ and a quadratic T dependence of σ_1 and hence of R_s.

Moreover, elastic impurity scattering leads to pair breaking of Cooper pairs with low binding energy. As a result, the linear dependence of $D(\epsilon)$ is cut off at $\epsilon = \hbar\tau_q^{-1}$ (energy corresponding to a momentum change Q due to a scattering event by $\epsilon = \hbar^2Q^2/2m^*$). The most important consequence is a finite density of states of $\hbar\tau_q^{-1}/\Delta$ at $\epsilon = 0$ and hence a finite density of normalconducting charge carriers at $T \to 0$. This density is of the order $ND(\epsilon = 0) = N\hbar\tau_q^{-1}/\Delta_{max}$ with N being the total charge carrier density. Therefore the resulting conductivity at $T \to 0$

$$\sigma_0 = \frac{\hbar e^2 N_0}{m^*\Delta_{max}} = \frac{\hbar}{\Delta_{max}\mu_0\lambda_L^2} \tag{2.37}$$

turns out to be independent of τ_q^{-1}. Using Eq. 2.14, the intrinsic residual surface resistance of a d-wave superconductor is expected to be of the order

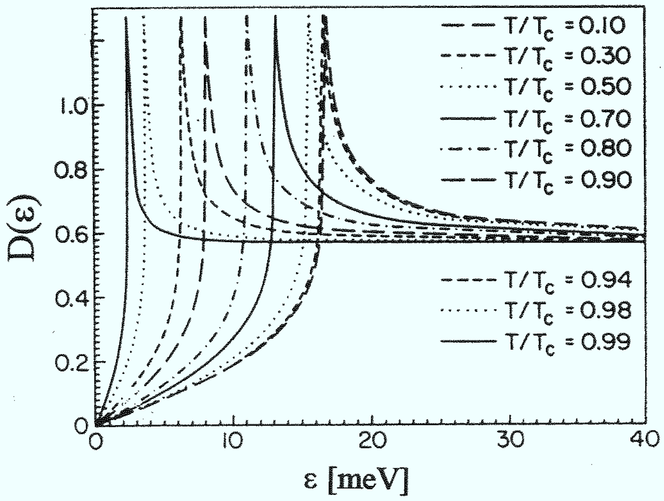

Fig. 2.6: Density of states in the weak-coupling limit for a $d_{x^2-y^2}$ pairing state at different reduced temperatures. Note the linear energy dependence of the density of states near the Fermi energy ($\omega = 0$). (from [55]).

$$R_{s,0} = \frac{\omega^2 \hbar \mu_0 \lambda_L}{2\Delta_{max}}, \tag{2.38}$$

in agreement with results of numerical calculations [86, 87]. Assuming $\Delta_{max} = 30$ meV (corresponding to $\Delta_{max}/kT_c = 3.9$) and $\lambda_L(0) = 140$ nm, $R_{s,0} = 8\ \mu\Omega$ results at a frequency of 10 GHz.

The electromagnetic response of superconductors with a higher order angular momentum pairing state was calculated in the framework of BCS theory either for point nodes or line nodes in the gap by Klemm et al. in order to fit experimental results for heavy-fermion superconductors [88]. Analytical results for $\lambda_L(T)$ and $\sigma_1(T)$ for a $d_{x^2-y^2}$ superconductor at $T << T_c$ were given by Hirschfeld et al. [86, 87]. All the following analytical expressions for a d-wave superconductor are based on the limit of strong scattering (unitary limit). Calculations for the limit of weak scattering (Born approximation) show completely different temperature dependences, most of them in strong contradiction to experimental results [32, 89]. The justification of the unitary limit, however, has not been yet worked out clearly.

As a result of impurity scattering $\lambda_L(T)$ exhibits a transition at $T = T^*$ from linear above to quadratic T dependence below T^* [86, 87]:

$$\lambda_L(T) = \lambda'_L(0) + \frac{aT^2}{T^* + T} \tag{2.39}$$

with

$$T^* \approx 0.83\sqrt{\Gamma\Delta_{max}} \quad \text{and} \quad \lambda'_L(0) \approx \lambda_L(0)(1 + 0.79\sqrt{\Gamma\Delta_{max}})$$

In Eq. 2.39 $\Gamma = \hbar\tau_{res}^{-1}/2$ is determined by the elastic impurity limit of the quasiparticle scattering rate $\tau_q^{-1}(T \to 0) = \tau_{res}^{-1}$, the quantity a is a parameter of the order of 1. Eq. 2.39 only holds true for low frequencies with ($\omega\tau_{res} << 1$). At high frequencies and low impurity scattering rates with $\omega\tau_{res}$ approaching unity relaxation effects give rise to a less strong $\lambda_L(T)$ dependence [32] (see next paragraph).

The conductivity σ_1 exhibits a quadratic temperature dependence below T^* (gapless regime), limited by the residual conductivity σ_0 (Eq. 2.37):

$$\sigma_1(T) = \sigma_0[1 + (\pi^2/12)(T/\gamma)^2], \quad \text{with} \quad \gamma \approx 0.63\sqrt{\Gamma\Delta_{max}} \tag{2.40}$$

For $T > T^*$ and for frequencies small in comparison to the scattering rate, or explicitly, for $\hbar\omega << \Gamma\Delta_{max}/T$, a nearly quadratic T dependence results:

$$\sigma_1(T) \approx \frac{2}{3}\sigma_0[\frac{kT}{\Delta_{max}}]^2 \log^2(4\Delta_{max}/kT) \tag{2.41}$$

Except for the logarithmic divergence, the same expression for $\sigma_1(T)$ results from the phenomenological model assuming $A = 1/\Delta_{max}$, $\sigma_0 = \sigma_n$, and $n = 1$ in Eq. 2.31.

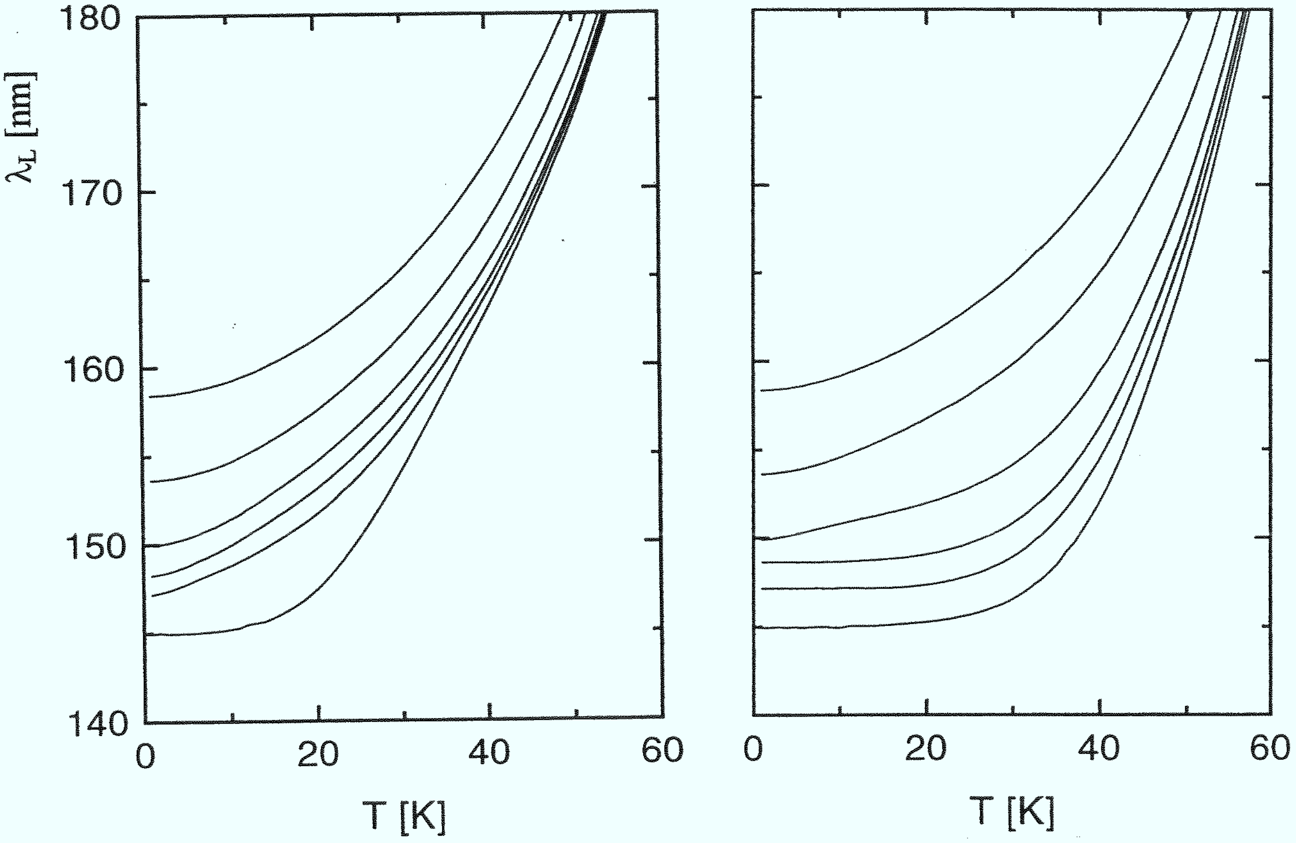

Fig. 2.7: Calculated temperature dependence of the penetration depth λ_L at 19 GHz (left) and 87GHz (right) for a d-wave superconductor using $\lambda_L(0) = 145$ nm, $2\Delta_{max}/kT_c = 6.0$, $T_c = 92.5$ K, and a temperature-dependent quasiparticle scattering rate according to Eq. 4.1 in Section 4.1 using $\tau_{res}^{-1}/10^{11}$ s^{-1} = 20, 10, 4, 2, 1, 0 (from top to bottom) as the elastic impurity limit.

Fig. 2.7 a,b shows the calculated temperature dependence of the penetration depth λ_L at 19 GHz (a) and 87 GHz (b) for a d-wave superconductor using $\lambda_L(0) = 145$ nm, $2\Delta_{max}/kT_c = 6.0$, $T_c = 92.5$ K. For the temperature-dependent quasiparticle scattering rate $\tau_{res}^{-1} = \tau_{in}^{-1} + \tau_{res}^{-1}$ the results from Fig. 2.4 (fit to Hardy data) were used for the inelastic scattering rate $\tau_{in}^{-1}(T)$, the impurity scattering rate was varied according to $\tau_{res}^{-1}/10^{11}$ s^{-1} = 20, 10, 4, 2, 1, 0 (from top to bottom). Fig. 2.8 a, b shows $R_s(T)$ at 19 GHz (a) and 87 GHz (b) calculated with the same parameters as λ_L in Fig. 2.7a,b. In contrast to the approximation formula Eq. 2.39, the linear temperature dependence of λ_L for the clean d-wave superconductor vanishes with increasing frequncy. This is a result of quasiparticle relaxation (similar to a Drude conductivity, see Eq. 2.33) at temperatures below which $\omega\tau_q(T) = 1$ holds. Therefore, the temperature below which λ_L becomes temperature-independent increases with increasing frequency. This relaxation effect also leads to a weakening of the $R_s(T)$ slope at $T << T_c$, which is similar to a thermally activated behavior (as usually expected for a finite energy gap, i.e. s-wave).

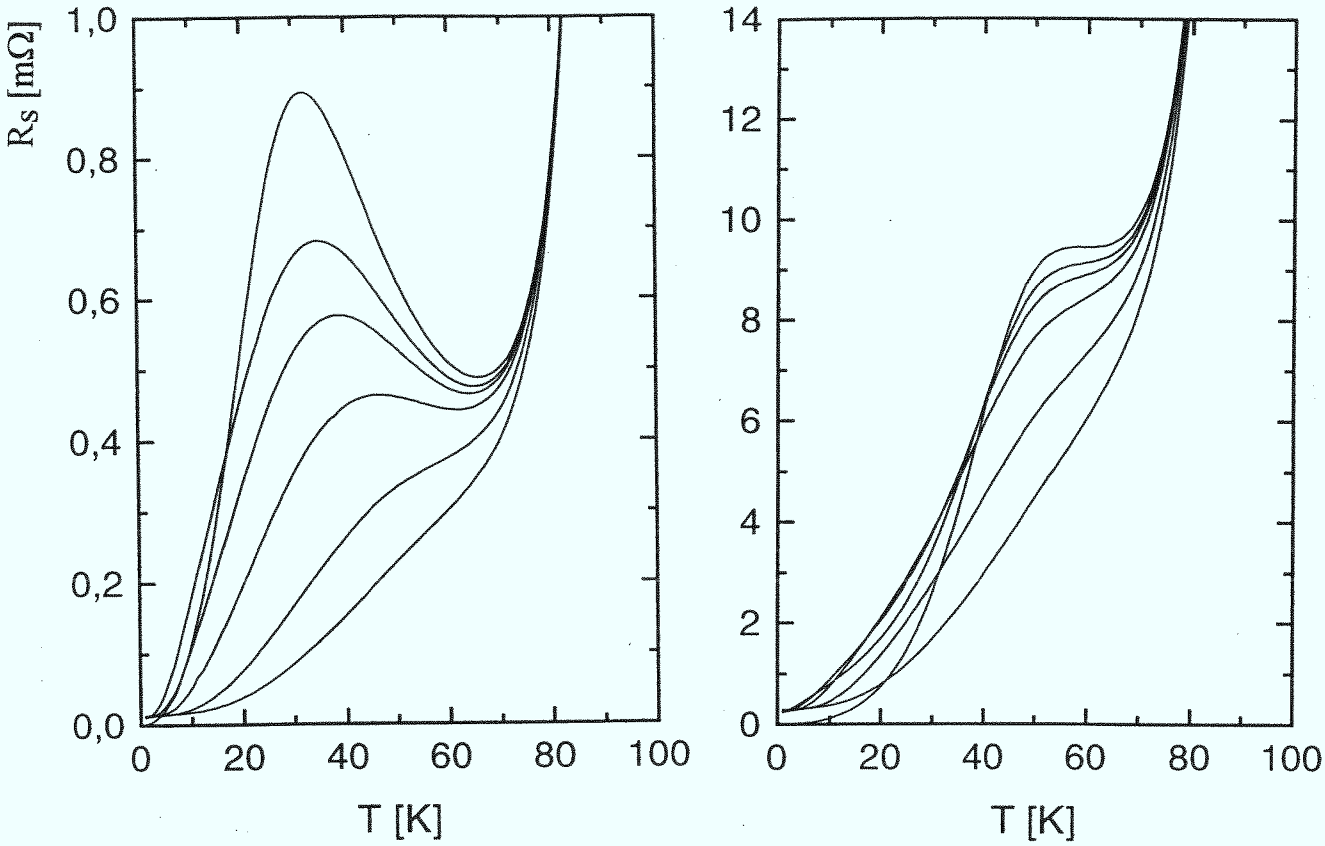

Fig. 2.8: $R_s(T)$ at 19 GHz (left) and 87 GHz (right) calculated with the same parameters as λ_L in Fig. 2.6a,b using $\tau_{res}^{-1}/10^{11}\ \mathrm{s}^{-1} = 20, 10, 4, 2, 1, 0$ (from bottom to top).

As already discussed in Subsection 2.2.2, the frequency and temperature dependence of $R_s(T)$ at elevated temperatures up to T_c reflects the decrease of the quasiparticle scattering rate which is introduced phenomenologically into the weak-coupling theory on the basis of experimental results. As a possible scenario leading to a d-wave pairing state superconductivity generated by exchange of antiferromagnetic spin fluctuations has been worked out in detail [55, 90, 91, 92, 93]. Assuming that antiferromagnetic spin fluctuations rather than phonons provide the dominant contribution to inelastic quasiparticle scattering, a strong temperature decrease of the quasiparticle scattering rate just below T_c results [11]. Similar to phonon-mediated superconductivity, strong-coupling calculations are required for the modeling of σ_1 and λ_L beyond $T << T_c$ adequately. For the d-wave, the strong anisotropic s-wave, and the two-band scenario the effect of phonons and spin fluctuations will be pair breaking at elevated temperatures, which is expected to result in a two-fluid-model-like behavior of σ_1 above a certain temperature.

Finally, as a result of a d-wave pairing state there is also a small nonlinearity of the surface impedance. Generally, the intrinsic penetration depth exhibits a dependence on rf power associated with pair breaking at finite current densities. Microscopically, pair breaking results from a shift of the quasiparticle energy by an amount $\delta\epsilon = mv_F v_s \approx \Delta H/H_c$ with v_s being the velocity of the quasiparticles associated with the supercurrent $j_s = eN_s v_s$, H the magnetic field associated with the supercurrent, and $H_c \approx \sqrt{H_{c1}H_{c2}} \approx 3$ T $/\mu_0$ (assuming $\mu_0 H_{c1} \approx 100$ mT and $\mu_0 H_{c2} \approx 100$ T) being the thermodynamic critical magnetic field. For an isotropic s-wave superconductor velocity-induced pair breaking results in a quadratic dependence of the London penetration depth on a magnetic field applied parallel to the surface [94]

$$\frac{1}{\lambda_L(T,H)} = \frac{1}{\lambda_L(T,H=0)}\left[1-\frac{1}{3}\alpha(T)\left[\frac{H}{H_c(T)}\right]^2\right] \tag{2.42}$$

with $\alpha > 0$ and $\alpha(T) \to 0$ for $T \to 0$. For a superconductor with $d_{x^2-y^2}$ symmetry pair breaking is even possible at $T \to 0$, because of quasiparticles with low binding energy around the direction of nodes in $\Delta(\vec{k})$. For $H > kTH_c/\Delta$ a linear field dependence results from the linear energy dependence of the density of states

$$\frac{1}{\lambda_L(T,H)} = \frac{1}{\lambda_L(T,H=0)}\left[1-\alpha\frac{2}{3}\frac{H}{H_c(T)}\right] \tag{2.43}$$

with $\alpha = 1(1/\sqrt{2})$ for $\vec{H}$ parallel to the direction of a node (antinode) of $\Delta(\vec{k})$. It is emphasized that Eqs. 2.42 and 2.43 are valid explicitly for static magnetic fields oriented parallel to the surface. However, as long as the photon energy $\hbar\omega$ is small in comparison to $\Delta_{max}H/H_c$, the field dependence is expected to be the same. As an example, at $\mu_0 H = 10$ mT the corresponding frequency at which the two energies are equal is 24 GHz.

To date, the effect of current-induced pair breaking on the real part of the conductivity has not been worked out. From the two-fluid model, however, the magnitude of the effect can be estimated assuming that current-induced pair breaking, which reduces the number of Cooper pairs and thereby enhances λ_L, gives rise to an additional normal-conducting fluid. The density of this fluid $N_n(H) = N_s(0) - N_s(H) = m^*/(2e^2\mu_0)(\lambda_L^{-2}(0) - \lambda_L^{-2}(H))$ (see Eq. 2.12) is proportional to H/H_c according to Eq. 2.43. Therefore, using Eqs. 2.11, 2.12 and 2.14, the field dependence of the surface resistance of a superconductor with $d_{x^2-y^2}$ symmetry at $T << T_c$ can be estimated by:

$$\Delta R_s(H) = R_s(H) - R_s(0) \approx \frac{1}{2}\omega^2\mu_0\lambda_L\tau\frac{H}{H_c} \tag{2.44}$$

For high-purity $YBa_2Cu_3O_{7-x}$ single crystals or thin films with small defect density ($\lambda_L = 150$ nm, $\tau^{-1} \approx 10^{-11}$ s^{-1}, see Section 4.1), and $\mu_0 H_c$=3 T, the slope of $R_s(H) - R_s(0)$ with H is 1.2 $\mu\Omega$/mT at $f = 10$ GHz. For large scattering rates (gapless regime, see Section 2.2.3) one expects a quadratic field dependence [95].

2.2.4 The mixed state

The electrodynamic response of oxide superconductors in the mixed state was treated by Coffey and Clem [96] and Brandt [97] to account for the effects of vortex pinning, viscous vortex drag, and flux creep on the surface impedance in ambient static magnetic fields applied perpendicular to the plane where the high frequency currents flow. From the vortex equation of motion Coffey and Clem derived an analytical expression for the surface impedance assuming a periodic pinning potential with one single activation energy U_0 [96, 98]:

$$\frac{Z_s}{i\omega\mu_0} = \sqrt{\frac{\lambda_L^2 + \lambda_C^2[\frac{f(\nu)-i\epsilon(\nu)(\omega_p/\omega)}{1+i(\omega/\omega_p)f(\nu)}]}{1+2i(\lambda_L^2/\lambda_n^2)}} \tag{2.45}$$

with

$$f(\nu) = \frac{I_0^2(\nu)-1}{I_0(\nu)I_1(\nu)} \quad \text{and} \quad \epsilon(\nu) = \frac{1}{I_0^2(\nu)}$$

In Eq. 2.45 $\nu = U_0(T,B)/kT$, and $I_0(\nu)$ and $I_1(\nu)$ are modified Bessel functions of the first kind. Two of the three relevant screening lengths in Eq. 2.45 are the London penetration depth in the absence of vortices λ_L and the normal-fluid skin depth λ_n, which is normalized to account for the surface fraction H/H_{c2} filled by vortex cores:

$$\lambda_n = \sqrt{\frac{2\rho(T)H}{\mu_0\omega H_{c2}}} \tag{2.46}$$

In Eq. 2.46 $\rho(T)$ is the normal-state resistivity of the quasiparticles in the vortex core and H_{c2} the upper critical field. The characteristic length associated with the vortex dynamics is the Campbell penetration depth λ_C

$$\lambda_C = \sqrt{\frac{H\phi_0}{\alpha_p}} \tag{2.47}$$

describing the electromagnetic field penetration due to the reversible motion of vortices within their pinning potentials. In Eq. 2.47 ϕ_0 is the magnetic flux quantum, and α_p the proportionality factor between restoring pinning force and vortex displacement, known as the Labusch parameter. The characteristic frequency of vortex dynamics is the pinning frequency $\omega_p = \alpha_p/\eta$ with η being the vortex viscosity.

Neglecting the effects of thermal agitation in Eq. 2.45 ($f(\nu) = 1, \epsilon(\nu) = 0$) and the losses associated with the normal fluid in the vortex cores ($B << B_{c2}$), α_p and η can be determined experimentally from Z_s:

$$\frac{Z_s}{i\omega\mu_0} = \sqrt{\lambda_L^2 + \frac{\lambda_C^2}{1+i\omega/\omega_p}} \tag{2.48}$$

For frequencies small in comparison to the pinning frequency $\omega/\omega_p << 1$ simple expressions for R_s and X_s result:

$$X_s \approx \omega\mu_0\sqrt{\lambda_L^2+\lambda_C^2} \quad \text{and} \quad R_s \approx \frac{\mu_0\omega^2}{2\omega_p}\frac{\lambda_C^2}{\sqrt{\lambda_C^2+\lambda_L^2}} \tag{2.49}$$

For very high magnetic fields corresponding to several tesla, λ_C is large in comparison to λ_L, which results in a linear dependence of both R_s and X_s on the magnetic field amplitude. According to Eq. 2.49 the additional surface resistance originating from the damped motion of vortices within their pinning potentials gives rise to quadratic dependence on frequency. As shown in Section 4.6, this is in contradiction to the experimental observation. The main effect of the thermally activated flux creep, which is included in Eq.2.45, is an increase of R_s at low frequencies. This increase gives rise to a frequency dependence of R_s which is significantly weaker than f^2.

For frequencies much larger than the pinning frequency ($\omega/\omega_p >> 1$ in Eq. 2.48) the vortices behave as if they were not pinned. In this case Eq. 2.48 becomes independent on α_p. For $T \rightarrow T_c$ λ_L diverges resulting in $Z_s = \omega\mu_0\lambda_n/2(1+i)$ which corresponds to the skin effect of normal metals (Eq. 2.8). At higher temperatures above the irreversibility line collective motion of vortices can give rise to a completely different behavior [99, 100].

Chapter 3

Experimental techniques

The main difficulty in measuring the surface impedance of superconductors in the microwave range is the low surface resistance R_s in comparison to that of normal-conducting metals. For conventional superconductors it is convenient to build cavities from bulk material, as e.g. niobium, or to coat a metallic bulk cavity with a polycrystalline film, as e.g. a niobium cavity with Nb_3Sn coating. Since in oxide superconductors the microwave losses are very low only for currents within the ab-plane, techniques for determining the in-plane surface impedance of epitaxial films and bulk single crystals are essential. In the microwave range below about 100 GHz such techniques need to be resonant techniques. In the millimeter- and submillimeter-wave range transmission techniques for thin films have turned out to be most sensitive.

3.1 Resonant techniques

Resonant techniques rely on the facts that, first, the quality factor of an electromagnetic resonator consisting partially of the HTS sample under investigation is determined by its surface resistance. Secondly, changes of the resonance frequency are related to changes of the penetration depth.

3.1.1 Cavity resonators

Typically, one endplate of a cylindrically shaped cavity machined from copper is replaced by a thin film sample [3, 21, 101, 102, 103]. The cavity should be excited in a transverse electric mode ($TE_{m,n,p}$-mode with E_z=0). The indices m, n, p represent the number of nodes in the field distribution in the ϕ, ρ and z-direction of a cylindrical coordinate system. Hence $z = 0$ indicates rotational symmetry of the electromagnetic fields. For TE_{0np} modes in a perfectly cylindrical shaped cavity there is no current flow from the cylinder wall to the endplate and hence no losses due to the joint between the HTS film and the cavity wall.

The surface resistance R_s of the thin film sample can be determined from the un-

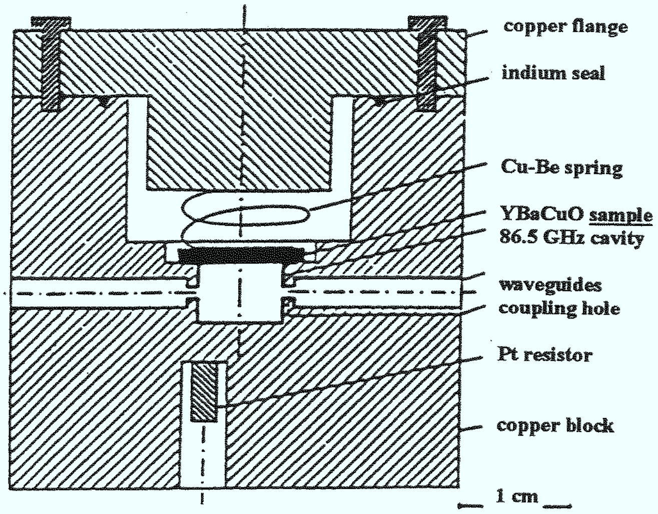

Fig. 3.1: Cavity resonator for the determination of the surface impedance of HTS films at 87 GHz according to Klein et al. [3].

loaded quality factor Q_0

$$\frac{1}{Q_0} = \frac{R_{s,c}}{G_c} + \frac{R_s}{G_s} \tag{3.1}$$

with geometric factors G_A defined as

$$G_A = \omega\mu_0 \frac{\int\limits_V \vec{H}^2(\vec{x}) d^3\vec{x}}{\int\limits_A \vec{H}^2(\vec{x}) d^2\vec{x}} \tag{3.2}$$

for surface sections $A = s$ for the sample surface exposed to the electromagnetic fields and $A = c$ for the remaining inner surface of the cavity. In Eq. 3.2 $\vec{H}(\vec{x})$ is the magnetic field distribution of the resonant mode, V the volume of the cavity, and $R_{s,c}$ the surface resistance of the cavity walls. A relation similar to Eq. 3.1 exists for changes of the surface reactance X_s which can be determined from changes of the resonance frequency f:

$$\frac{\Delta f}{f} = \frac{\Delta X_s}{2G_s} + \gamma(T) \tag{3.3}$$

The additional term $\gamma(T)$ is dominated by the thermal expansion of the cavity. Absolute values of X_s cannot be determined by cavity techniques, since the tolerances of the cavity dimensions are large in comparison to the penetration depth.

The sensitivity of the endplate replacement technique is limited by losses in the cavity walls and joint losses. Small joint losses in TE_{0np} modes may result from perturbations of the cylinder symmetry by coupling holes. Since R_s of a superconductor is expected to scale like f^2 (Eq. 2.14), this technique has turned out to be quite sensitive for $f > 50$ GHz. Besides sensitivity considerations, above about 50 GHz the thin film samples do not need to be larger than one centimeter in diameter. Above about 150 GHz mechanical tolerances become a severe problem, in particular for the coupling apertures.

In order to achieve ultimate accuracy a careful calibration of the cavity background losses is essential, firstly, with a niobium sample at $T \leq 4$ K to determine the cavity background quality factor at $T \leq 4$ K ($R_{s,c}/G_c$ in Eq. 3.1), and secondly, with a sample made from the same material as the cavity, to determine the temperature dependence of the cavity background quality factor. Klein et al developed a cylindrical copper cavity operated in the TE_{013} mode (Fig. 3.1) [3] which provides a sensitivity of ± 1 mΩ for R_s at 87 GHz corresponding to ± 13 $\mu\Omega$ at 10 GHz assuming f^2 frequency scaling [104].

3.1.2 Shielded dielectric resonators

Fig. 3.2 shows a schematic drawing of a shielded dielectric resonator for surface impedance measurements of thin film samples. Basically, a sapphire cylinder is attached to one HTS film (lower endplate in Fig. 3.2) and arranged symmetrically with respect to the cylinder axis inside a cylindrical metallic shielding cavity. The crystallographic c-axis of the sapphire cylinder is aligned along the cylinder axis. This orientation provides an isotropic permittivity of ϵ_r=9.4 for electric fields oriented perpendicular to the cylinder axis [107]. The second endplate arranged at a distance h above the cylinder can either be normal-conducting or formed by a second HTS thin film sample. The unloaded quality factor [105]

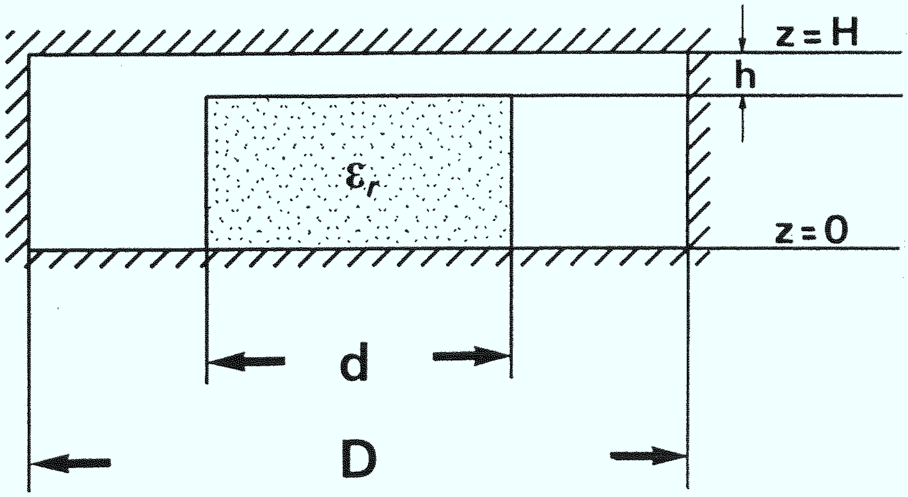

Fig. 3.2: Schematic drawing of a cylindrical shielded dielectric resonator (ϵ_r = permittivity). Either the lower endplate ($z = 0$) or both endplates ($z = 0$ and $z = H$) is made from HTS films (from [105]).

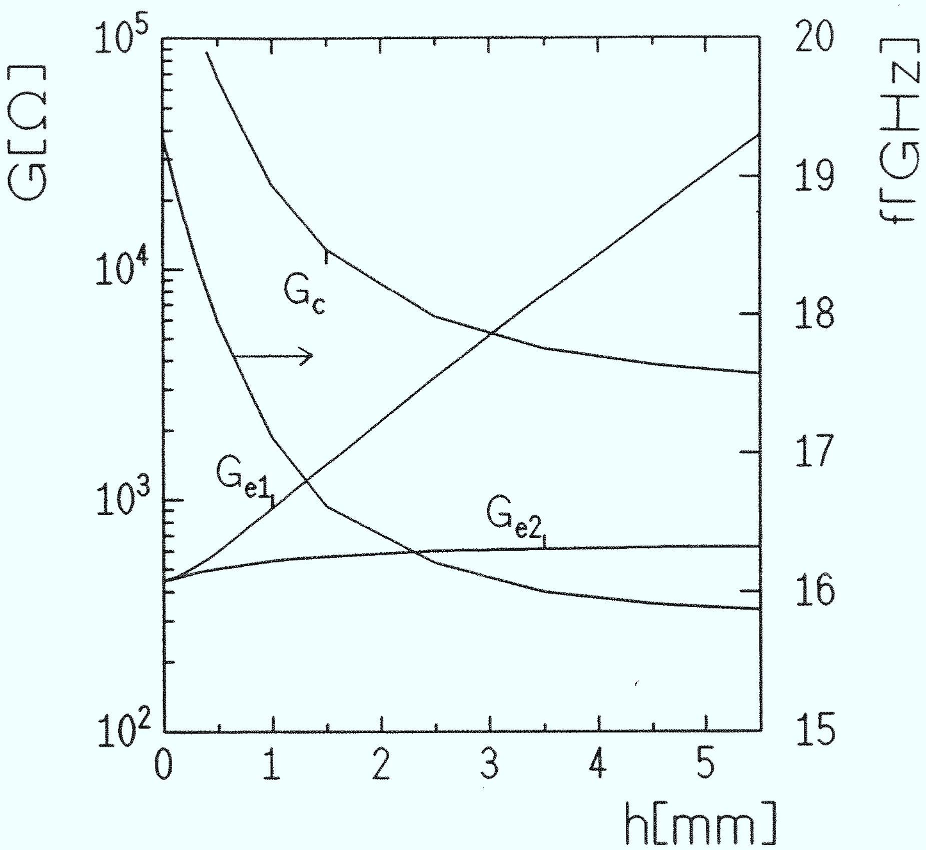

Fig. 3.3: Calculated geometric factors and resonant frequency as a function of gap width h for $D = 15$ mm, $d = 2h = 7$ mm, and $\epsilon_r = 9.4$ (see Fig. 3.2).

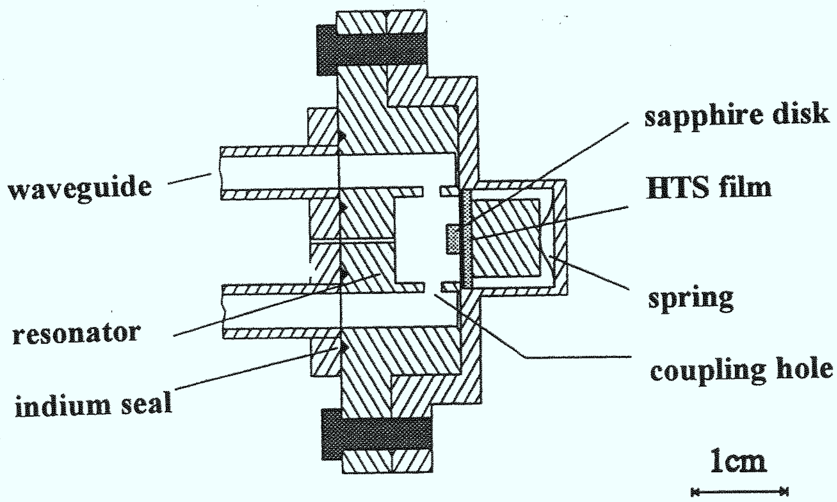

Fig. 3.4: Shielded dielectric resonator for surface impedance measurements on HTS films at 37 GHz (from [106]).

$$\frac{1}{Q_0} = \frac{R_{s,e1}}{G_{e1}} + \frac{R_{s,e2}}{G_{e2}} + \frac{R_{s,c}}{G_c} + \kappa \tan\delta \tag{3.4}$$

is determined by losses in the two endplates $e1$ (z=0 in Fig. 3.2) and $e2$ ($z = H$ in Fig. 3.2), by losses in the cylinder wall of the shielding cavity c and by dielectric losses in the sapphire cylinder determined by the filling factor $\kappa \leq 1$ and by the loss tangent $\tan\delta = \epsilon_{r,2}/\epsilon_{r,1}$ (see Subsection 2.1.1). For electric fields oriented perpendicular to the c-axis $\tan\delta$ of high purity sapphire is below 10^{-7} at $T < 70$ K and frequencies up to about 70 GHz [108, 109]. The main advantage of shielded sapphire dielectric resonators in comparison to cavity resonators is that the background losses, i.e. the contribution $R_{s,c}/G_c$ to $1/Q_0$, can be reduced to a negligible amount if the mode and the geometry are selected properly.

In order to understand how the losses of the normal-conducting cylinder walls of the shielding cavity are suppressed it is intuitive to consider a boundary along the x-axis between two media (a and b) with permittivity $\epsilon_{r,a} = \epsilon_r > 1$ and $\epsilon_{r,b} = 1$ in the xy-plane of a cartesian coordinate system. Let us assume a plane wave propagating parallel to the boundary (in x-direction) with electric field $E_z \propto A(y)\exp(i\beta x)$ polarized perpendicular to the xy-plane (z-direction). The Helmholtz wave equation leads to the following differential equations for the spatial dependence of the field amplitude perpendicular to the boundary $A(y)$ in regions a and b, respectively:

$$[\frac{\partial^2}{\partial y^2} + k_0^2\epsilon_r - \beta^2]A(y) = 0 \quad \text{and} \quad [\frac{\partial^2}{\partial y^2} + k_0^2 - \beta^2]A(y) = 0 \tag{3.5}$$

Under the conditions $k_0^2\epsilon_r - \beta^2 > 0$ and $k_0^2 - \beta^2 < 0$ ($k_0 = \omega/c$), which are equivalent to $k_0^2 < \beta^2 < k_0^2\epsilon_r$, $A(y)$ exhibits a sinusoidal y-dependence in region a and decreases exponentially outside the dielectric region (region b). Similar equations hold true for a cylindrically shaped dielectric waveguide with circular cross section excited in a TE_{0n} mode (Fig. 3.2): here the electric field is oriented parallel to the circular boundary, and the wave propagates along the guide (z-direction). Upon replacing $\partial^2/\partial y^2$ in Eq. 3.5 by the radial part of the Laplacian in cylindrical coordinates $\partial^2/\partial\rho^2 + 2/\rho \cdot \partial/\partial\rho$, the electromagnetic fields outside the dielectric rod decrease according to the modified Bessel function $K_n(\rho)$ in radial direction, i.e. exponentially for large ρ values. Hence a TE_{0np} resonator with negligible loss contribution from the cylinder walls can be formed by using two HTS films as endplates ($h = 0$ in Fig. 3.3). Upon increasing the width h of the gap between the sapphire disk and the upper endplate the loss contribution of the latter decreases gradually, but the losses in the cylinder wall increase. For this more general case, the electromagnetic fields can be modeled as an infinite sum of TE_{0n} modes of the shielded dielectric rod in region I ($0 \leq z < H - h$ in Fig. 3.2) and of TE_{0n}-modes of the circular metallic waveguide in region II ($H - h < z \leq H$ in Fig. 3.2) using a mode-matching technique [105]. Fig. 3.3 shows the calculated geometric factors G_{e1}, G_{e2}, and G_c as a function of h for a sapphire ($\epsilon_r = 9.4$) disk with $d = 7$ mm, $h = 3.5$ mm arranged in a shielding cavity with $D = 10$ mm. Obviously, G_{e1} is almost independent of h whereas G_{e2} increases monotonically. This indicates the possibility of using a normal-conducting endplate at larger h values in order to determine Z_s of one single film. However, for larger h G_c decreases resulting in a Q limitation by the cylinder walls.

Fig. 3.4 shows a shielded dielectric resonator used for Z_s determination of a single superconducting film at 37.3 GHz according to Klein and Scholen [106]. The ultimate quality factor at $T \leq 10$ K is 170000, limited by losses in the copper walls. The resulting sensitivity for R_s is $\pm 100\,\mu\Omega$, limited by a reproducibility of the measured quality factor of ±1% upon subsequently reassembling the resonator with the sample under investigation. A similar system was built by Klein et al. for 18.9 GHz with a sensitivity of $\pm 50\,\mu\Omega$ below 30 K [110]. Kobayashi et al. first used two HTS film as endplates of a sapphire without any gap ($h = 0$), followed by many other groups [111, 112, 113]. At 5.5 GHz Shen et al. achieved quality factors above 10^7 [112]. Such high values are possible, since in this configuration the background losses are neglegible. However, here the average surface impedance of two HTS films is probed simultaniously. To overcome this drawback, Diete et al. used a sapphire disk attached to a niobium sample, both thermally isolated by a small gap h from the HTS film under investigation [114]. This technique requires a high degree of mechanical stability in order to avoid irreproducible radiation losses due to the gap. As an alternative, Zuccaro and Klein [116] used a small gap of the order of one millimeter between the sapphire disk and the upper HTS films. In this case the loss contribution of the upper film is only 10% with repect to the losses of the lower film. Upon exchanging the two films between two subsequent measurements one can determine both $R_s(T)$ and $R_s(H_{rf}$ for each film.

The high quality factors make sapphire-shielded dielectric resonators with two HTS film endplates favorable for measurements of the dependence of R_s on the rf magnetic field. For such measurements the resonator is operated as a two-port device with the input-coupling antenna adjusted to critical coupling, i.e. the reflection coefficient of the resonator is zero at the resonance frequency. The output antenna, which is used to determine the resonance curve, is adjusted to very weak coupling. In order to operate the resonator at high levels of rf power it is essential to employ a measurement technique where the rf power is pulsed. Typically, short pulses of 10-100 μs length are used. The unloaded quality factor Q_0 and power dissipated in the resonator P_0 are determined from the insertion loss and the absolute level of rf power radiated from the output-coupling antenna. The maximum value of the rf magnetic field H_{max} on the surface of the HTS film is proportional to the squareroot of the electromagnetic field energy stored in the resonator W, which can be determined from the socalled circulating power P_0Q_0 according to $\omega W = P_0Q_0$. Finally, the proportionality factor between H_{max} and P_0Q_0 needs to be determined using a numerical field simulation software, e.g. the computer code "MAFIA [118]". With sapphire dielectric resonators with Q_0 values of 10^6, typically 50-100 W of microwave power are required in order to achieve rf-field levels of the order of the lower critical field $\mu_0 H_{c1} \approx 100$ mT. This indicates, that the high quality factors are essential to perform such measurements with commercial travelling-wave tube amplifiers.

3.1.3 Quasioptical resonators

Among the quasioptical resonators semi-confocal resonators have been used successfully for Z_s determination in the millimeter-wave range. A semi-confocal resonator is formed by two oppositely facing metallic mirrors, one being spherically curved and the other plane. The plane mirror is formed by the HTS film under investigation and is positioned at a distance b from the curved mirror. In the semi-confocal arrangement b is equal to the radius of curvature of the curved mirror. Semi-confocal resonators exhibit sufficiently low diffraction losses if the diameter of the HTS film is as large as a few times the beam waist radius. The beam waist radius w_b defines the spatial dependence of the electromagnetic fields on the surface of the plane mirror in radial direction according to $\exp(-\rho^2/w_b^2)$ [122]:

$$w_b = \sqrt{\frac{bc}{2\pi f}} \tag{3.6}$$

As an example, at $f = 100$ GHz and $b = 3$ cm w_b is 3.7 mm, i.e. above about 100 GHz this technique is applicable for $1 \cdot 1\text{cm}^2$ films. Martens et al. first used a 36 GHz semi-confocal resonator for R_s measurements of large-area HTS films [123]. At Conductus company a semi-confocal resonator system for spatially resolved R_s determination at 94 GHz was developed [124]. The sensitivity is limited by losses in the curved mirror if it is machined from a normal-conducting metal. In principle, a very high sensitivity is achievable if the curved mirror is machined from niobium. In this case the HTS film must be heated separately from the curved niobium mirror, which needs to be held at helium temperatures. Presently, such a system is operated at the University of Houston [125].

3.1.4 Planar resonators

Planar resonators are of great importance for surface impedance measurements and as part of HTS microwave devices like filters and antennas. Basically, planar resonators consist of a transmission line of length l, prepared by photolithography from an HTS film. Resonances occur at frequencies $f_n = nc_{ph}/(2l)$ with $n = 1, 2, 3...$ and c_{ph} being the phase velocity of the transmission line. Both straight and s-shaped transmisson lines have been used, as well as ring resonators forming a closed transmission line. The transmission lines are either coplanar lines (Fig. 3.5a), striplines (Fig. 3.5b), or microstriplines. Coplanar resonators require only one single film whereas for microstripline and stripline resonators one, respectively two unpatterned HTS groundplanes are required to reduce radiation losses sufficiently. The quality factor of a stripline resonator can be approximated by

$$\frac{1}{Q} = \frac{\pi Z_L^2 \epsilon_{r,eff} h f}{Z_0 c R_s} + \tan\delta \tag{3.7}$$

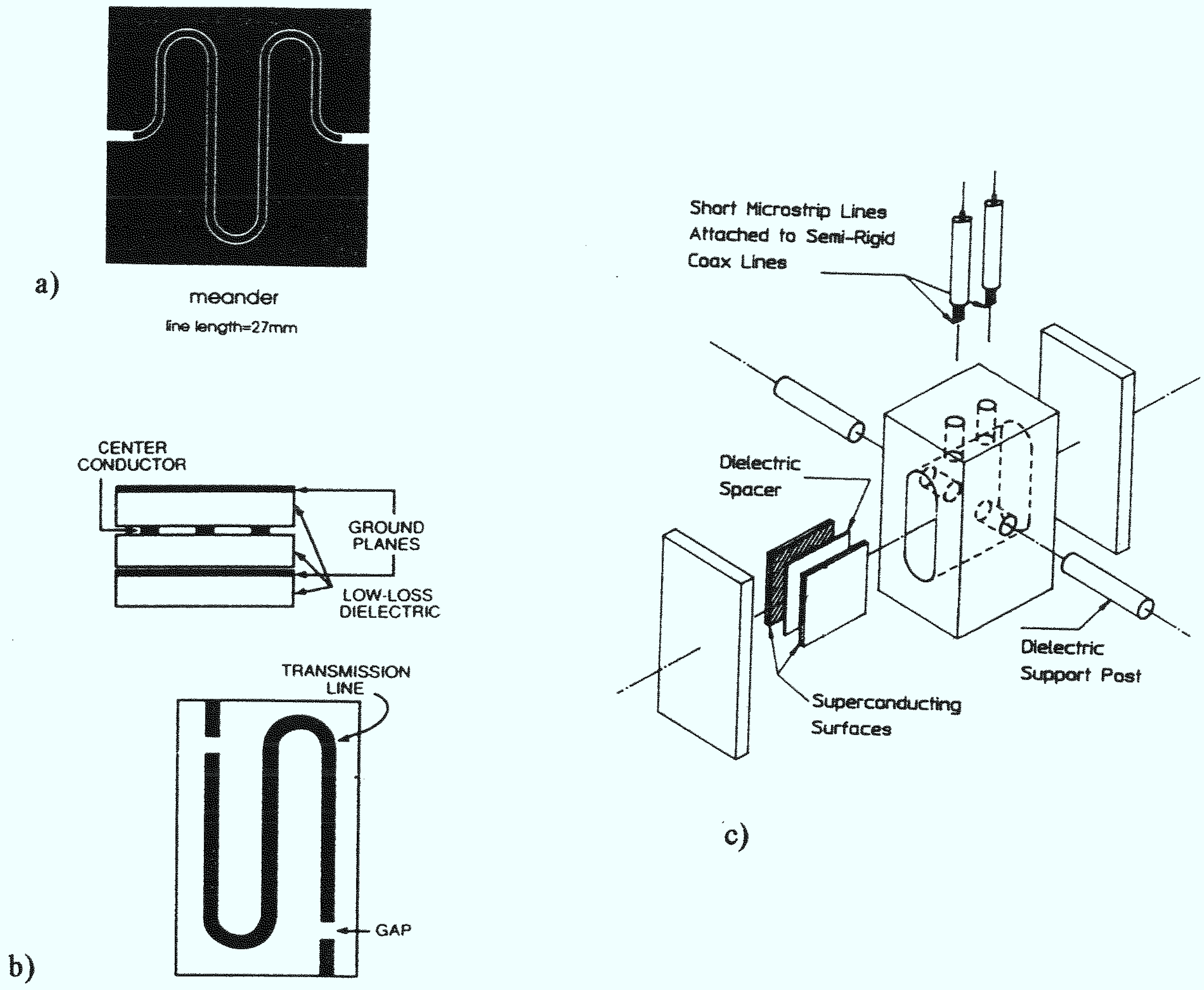

Fig. 3.5: Meander coplanar resonator (a, from [126]), stripline resonator (b, from [127]), and parallel plate resonator (c, from [128]) for surface impedance measurements of HTS films.

with Z_L being the line impedance, h, $\epsilon_{r,eff}$ and $\tan\delta$ the thickness, effective permittivity and loss tangent of the substrate. Eq. 3.7 is valid for $w >> h$ (w = width of stripline), more general analytical formulas can be taken from [129].

A severe difficulty for the rigorous determination of the surface impedance by transmission line resonators arises from the strong current enhancement in the edge region of the line. As shown by a numerical analyis of the electromagnetic fields, which involves the complex conductivity of superconductors, the current at the edge is about 10 times larger than at the center of the conductor and decreases on the length scale of the penetration depth (Fig. 3.6) [130]. For coplanar lines this field enhancement is even stronger [126].

According to Eq. 3.7, for a stripline resonator with h = 1 mm, $\epsilon_r \approx 10$ (sapphire,

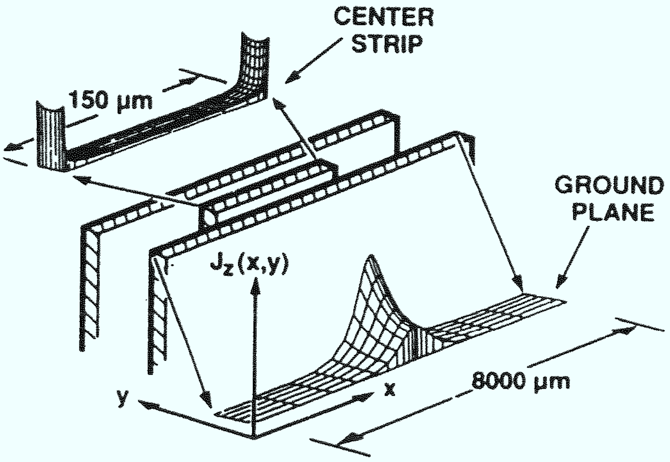

Fig. 3.6: Result of numerical calculation showing the stripline current distribution for a superconductor with $\lambda_L = 160$ nm and film thickness of 300 nm. The current density $J_{x,y}$ in the center conductor is about 10 times larger with respect to that in the ground plane (from [127]).

MgO), and $R_s = 0.5$ mΩ (typical for epitaxial $YBa_2Cu_3O_{7-x}$ films at 77 K and 10 GHz (see Section 4.1), the Q-contribution of the HTS films is about 14000 and typically up to one order of magnitude higher at 4 K. In order not to be limited by dielectric losses the substrates for the HTS films should have $\tan\delta$-values below 10^{-5}. Materials which fulfil this requirement and additionally provide conditions favorable for the growth of the HTS films are single crystalline $LaAlO_3$ with $\epsilon_r = 23.4$ [105, 131, 132], MgO with $\epsilon_r = 9.7$ [131], and sapphire with $\epsilon_r = 9.4$ and 11.2 for the $ab-$ and c direction, respectively [108, 131]. Although sapphire is challenging due its extremely low $\tan\delta$ the anisotropic ϵ_r makes the design of resonators and filters complicated. In particular the fact that HTS films are usually grown on the so-called r-plane of sapphire, which is tilted by 57.6° with respect to the plane of constant ϵ_r of the permittivity ellipsoid [133].

The parallel plate resonator first used by Taber et al. is a two-dimensional stripline resonator which allows to determine the surface impedance of unpatterned films [128]. Here the resonator is formed by a sandwich of two HTS-coated substrates with a thin dielectric plate arranged between the HTS-coated sides of the substrates (Fig. 3.5c). The ultimate sensitivity of a few microohms at 10 GHz was achieved using a 10 μm thin Teflon sheet as a dielectric plate. Similar to the dielectric resonator with superconducting endplates, only the average Z_s of two films can be determined. A disadvantage of this technique is the small dynamic range of measurable R_s values of about two orders of magnitude. This is because close to T_c the quality factors become as low as a few hundred. At such low quality factors interference with housing resonances and crosstalk between the coupling antennas hamper the determination of the resonator quality factor.

As discussed in Section 4.5, the rf current enhancement in stripline resonators affects the observed dependences of the surface impedance on the rf magnetic field. Recently, Chaloupka et al. employed the TM_{010} mode in a two-dimensional circular disk-shaped microstrip resonator [114]. For this mode there is no current enhancement at the edges, since the rf-current is oriented in radial direction. Such resonators provide quality factors of several 10^5 and therefore allow the determination of $R_s(H_{rf})$ simlar to shielded dielectric resonators. However, in order to achieve such high quality factors reproducibly, the ground plane and the circular disk need to be formed by a substrate which is coated by an HTS film one each side. In turn, this drawback makes this resonator attractive as an extreme compact element for bandpass filters operating at high levels of rf power [115].

3.1.5 Cavity perturbation techniques

The cavity endplate replacement technique described in Subsection 3.1.1 is a perturbation technique in the sense that the finite conductivity of the HTS film under investigation is treated as a perturbation of the resonant frequency of the employed eigenmode of the cavity. The cavity perturbation techniques discussed in this subsection rely on the smallness of the sample in comparison to the cavity. Therefore this technique is appropriate for bulk single crystals. As shown in Fig. 3.7a-c, the HTS sample is glued to a sapphire cold finger, and positioned in a high magnetic field region of a superconducting host cavity. The host cavities are in many cases cylindrical cavities either machined from high purity niobium or from copper with lead coating. Typical background quality factors Q_b of such cavities (without sample) are in the 10^7 to 10^9 range. For the case of aligning the ab-plane of the HTS sample in the direction of the unpertubated cavity field, the surface resistance can be determined from the measured quality factor Q_s by

$$1/Q_s - 1/Q_b = \frac{R_s H_s^2 A_s}{2\omega W} \tag{3.8}$$

with H_s being the unpertubated rf magnetic field at the position of the sample and A_s the surface area of the sample. It is important to note that this technique always gives a contribution of the rf response along the c-axis (typical thickness of bulk single crystals is 50 to 100 μm). On the other hand, a possible in-plane surface impedance anisotropy can be determined by exposing the crystal with different orientations with respect to the cavity electromagnetic field. For that purpose Wehler et al. constructed a cylindrical niobium cavity with the sample attached to a rotatable sapphire piston in the cylinder wall (Fig. 3.7a, [134, 135]). Bonn et al. used a split ring resonator at 1.5 GHz to attain a sensitivity as high as ±0.1 nm for measurements of small changes of the magnetic field penetration depth with temperature (Fig. 3.7c, [137, 138]). The standard configuration used nowadays in many laboratories is a cylindrical TE_{011} cavity with the HTS sample placed in the center with the unperturbated magnetic field aligned along the cylinder axis (Fig. 3.7b). This technique can also be used for small thin film samples, since there is (ideally) no electric field at the sample surface.

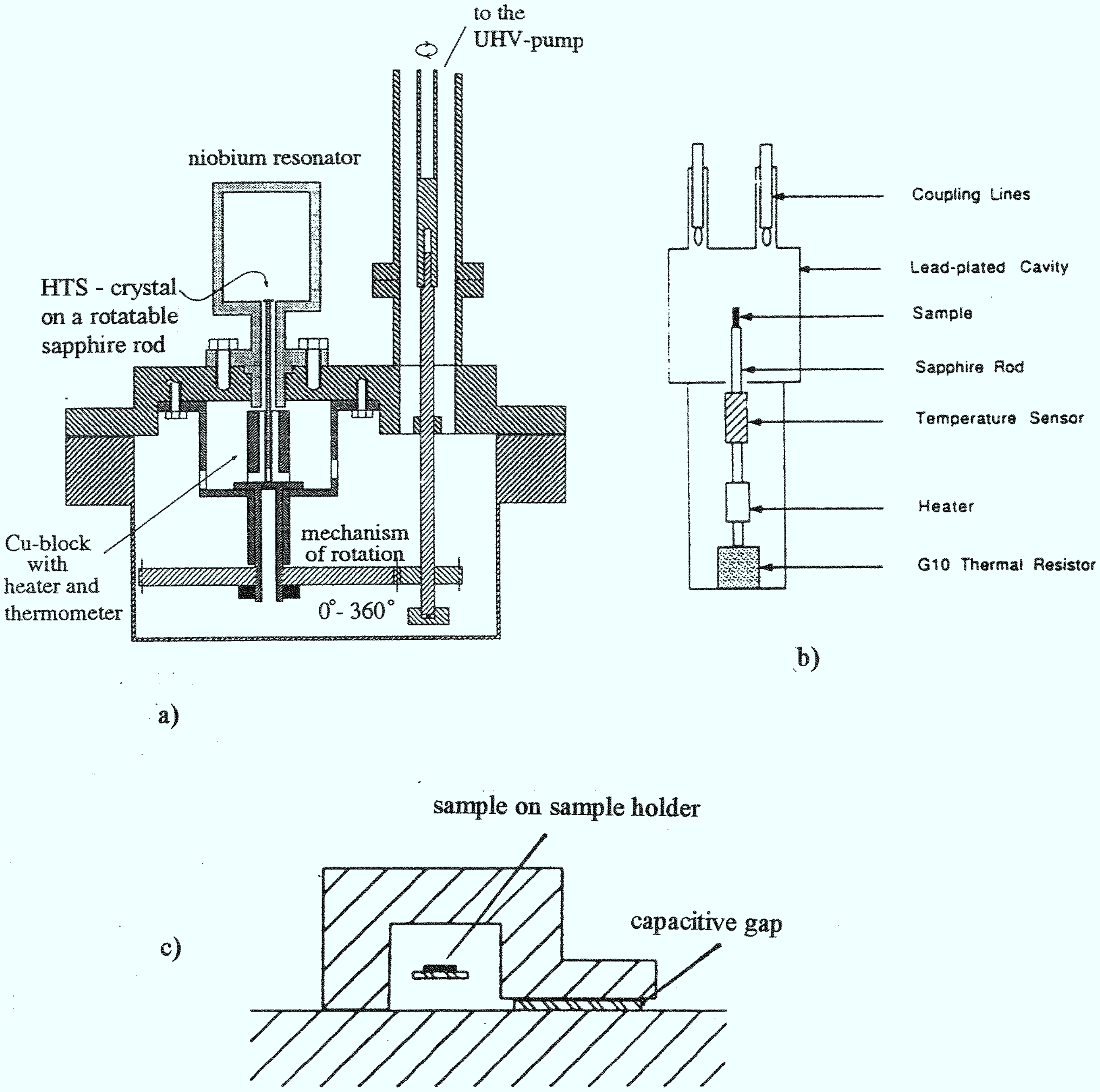

Fig. 3.7: Experimental setups to determine the surface impedance of bulk single crystals: a) 25 GHz TE_{013}-niobium host cavity with rotatable sample holder for anisotropy measurements (from [134, 135]), b) 9.6 GHz TE_{011}-host cavity (from [136]), and c) 900 MHz split ring resonator for precise $\lambda_L(T)$ determination (from [137, 138]).

3.2 Nonresonant techniques

Nonresonant techniques rely on single path transmission or a single reflection of an electromagnetic wave. Therefore the smallness of the surface resistance of high-quality HTS samples makes nonresonant techniques only suitable at very high frequencies above a few hundred Gigahertz.

3.2.1 Reflectivity measurements

Reflectivity measurements have been performed at far-infrared frequencies using Fourier spectroscopy. The reflectivity $|R|^2$ or absorptivity $A = 1 - |R|^2$ determined by this technique is related to the surface impedance by Eq. 3.9, which results from the continuity of the electric and magnetic fields of the plane wave at the surface:

$$|R|^2 = |\frac{Z_s - Z_0}{Z_s + Z_0}|^2 \approx 1 - \frac{4R_s}{Z_0} \tag{3.9}$$

The approximative expression for $|R|^2$ in Eq. 3.9 becomes valid for $R_s, X_s << Z_0 = 376\,\Omega$, which holds up to the optical frequency range. The lowest accessible frequencies for Fourier spectroscopy are in the range of 300 GHz corresponding to wave numbers of $10\,\text{cm}^{-1}$. At such low frequencies $|R|^2$ is close to unity, which limits the accuracy of R_s determination in the superconducting state. In particular, there is a source of systematic error due to the uncertainty by which the reflectivity of the reference sample (usually a gold film) is known. The main strength of Fourier spectroscopy, however, is the determination of the energy gap by direct quasiparticle excitation at $\omega = 2\Delta/\hbar$. Gap-like structures in HTS films and bulk single crystals have indeed been observed at wave numbers of about $400\,\text{cm}^{-1}$ corresponding to $2\Delta/kT_c \approx 8$. The detailed discussion of such experiments and the investigation of phonon excitations by far-infrared spectroscopy are beyond the scope of this article, but are treated in a review by Renk [5].

Reflectivity measurements with far-infrared lasers were performed by Cohn et al. [139] to determine R_s of HTS films. At low frequencies this technique provides a somewhat higher accuracy than Fourier spectroscopy, since more intensity is available. However, in comparison to resonant techniques the accuracy is quite poor since at $T << T_c$ $|R|^2$ is too close to unity.

3.2.2 Transmission spectroscopy

Transmission of an electromagnetic wave through a thin HTS film has turned out to be a powerful tool to determine the frequency dependence of the surface impedance in the millimeter- and submillimeter-wave range. For simplicity, we consider a plane electromagnetic wave passing through a superconducting layer of thickness t_f and neglect the effects of the substrate. The direction of propagation is perpendicular

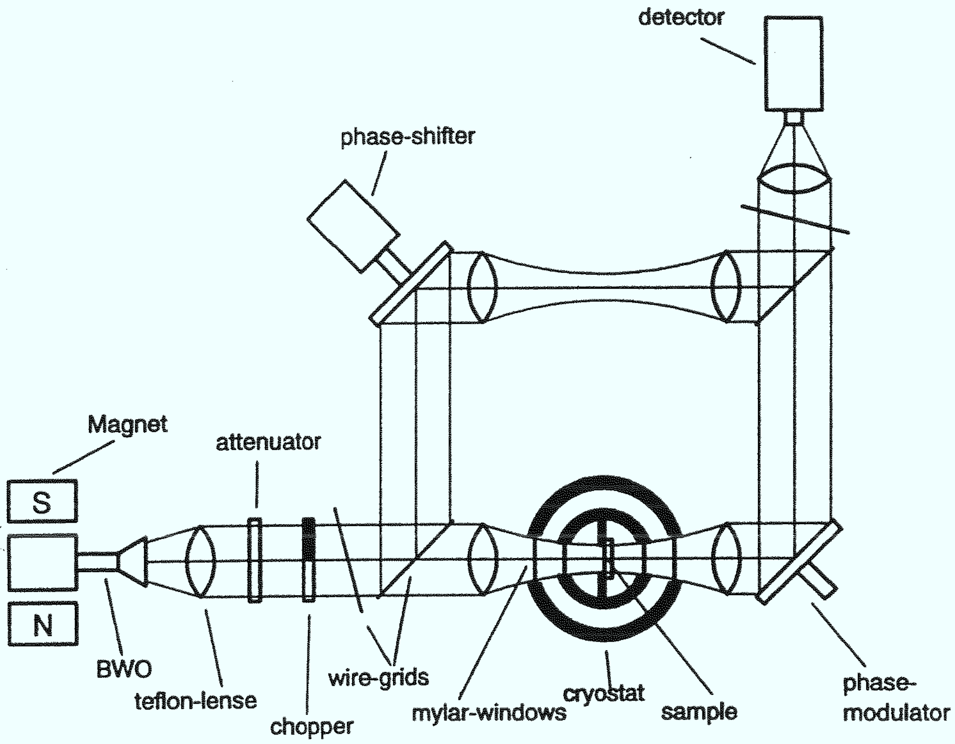

Fig. 3.8: Quasioptical spectrometer for submillimeter-wave transmission spectroscopy (from [66]).

to the surface. Within the approximation $\sigma_1 << \sigma_2$ (Eq. 2.14) a simple analytical expression for the complex transmission coefficient $T = |T|\exp(i\delta\phi)$ with $|T|^2$ being the power attenuation and $\delta\phi$ the phase shift of the electromagnetic wave is given by [66].

$$|T|^2 = \left(\frac{2\lambda_L\omega}{c\sinh(t_f/\lambda_L)}\right)^2 \quad \text{and} \quad \delta\phi = -\frac{\pi}{2} + \sigma_1\omega\mu_0\lambda_L^2 = -\frac{\pi}{2} + \frac{2R_s}{\omega\mu_0\lambda_L} \qquad (3.10)$$

In contrast to normal-conducting metals, the power attenuation is independent of the absorption (within the approximation $\sigma_1 << \sigma_2$). Absolute values of λ_L can be determined from $|T|^2$ by this technique using Eq. 3.10, if the film thickness is known. As an example, for an $YBa_2Cu_3O_{7-x}$ film ($\lambda_L = 150$ nm) of 100 nm thickness the power attenuation is $8 \cdot 10^{-9}$ and $8 \cdot 10^{-7}$ at 10 and 100 GHz, respectively. These small numbers indicate that the application of a transmission technique is only useful for very thin films and high frequencies. The latter is of particular relevance for the determination of σ_1 or R_s from the phase shift. The best achievable $\delta\phi$ resolution of $\pm1°$ [133] results in an R_s resolution of ±1 mΩ at 100 GHz according to Eq. 3.10. Since R_s scales like f^2, the resolution increases linearly with increasing frequency.

Another limitation at low frequencies is the beam radius, which cannot be smaller than the Gaussian beam waist (Eq. 3.6, b = half distance between two lenses with focal length $b/2$). This limits the applicability of this technique for 1×1 cm^2 films to frequencies above about 170 GHz.

Fig. 3.8 shows the experimental setup for the determination of the (sub)millimeter-wave properties of HTS thin films in the frequency range from 170 to 700 GHz used by Dähne and Klein. This so-called backward-wave oscillator (BWO) spectroscopy was originally developed by Volkov et al. [140]. A quasioptical beam of a few milliwatts in power is generated by a tunable backward-wave oscillator. The beam is focused by Teflon lenses on the sample, which is arranged in an optical cryostat with Mylar windows. To avoid parasitic transmission by reflection from the windows the inner parts of the cryostat are coated with microwave-absorbing varnish. $|T|^2$ is determined from the measured amplitude attenuation in comparison to the attenuation measured with an empty aperture of the same size as the sample. The phase shift of the sample is determined by interference of two beams with one of them passing through the sample and the other along a reference branch of the spectrometer (Mach-Zehnder configuration). Fig. 3.9 shows $|T|^2$ (a) and $\delta\phi c/f$ (b) over the usable tuning range of one of the backward wave oscillators for an $YBa_2Cu_3O_{7-x}$ film of 60 nm thickness deposited on a $NdGaO_3$ substrate. The oscillations apparent in Fig. 3.9a,b are due to multiple reflections at the substrate surfaces. From the periodicity of these oscillations the permittivity of the substrate ($\epsilon_r = 22.5$ for $NdGaO_3$) can be determined. The values calculated by Eq. 3.10 correspond to the minima in the $|T|^2$ spectra. The loss tangent of this particular substrate was found to be small enough to have minor effects on the spectra. However, generally the determination of the film conductivity from the spectra requires the determination of the complex permittivity of the uncoated substrate from a separate measurement. Substrates with internal twin structure like $LaAlO_3$ give more irregular spectra which hamper the performance of this technique.

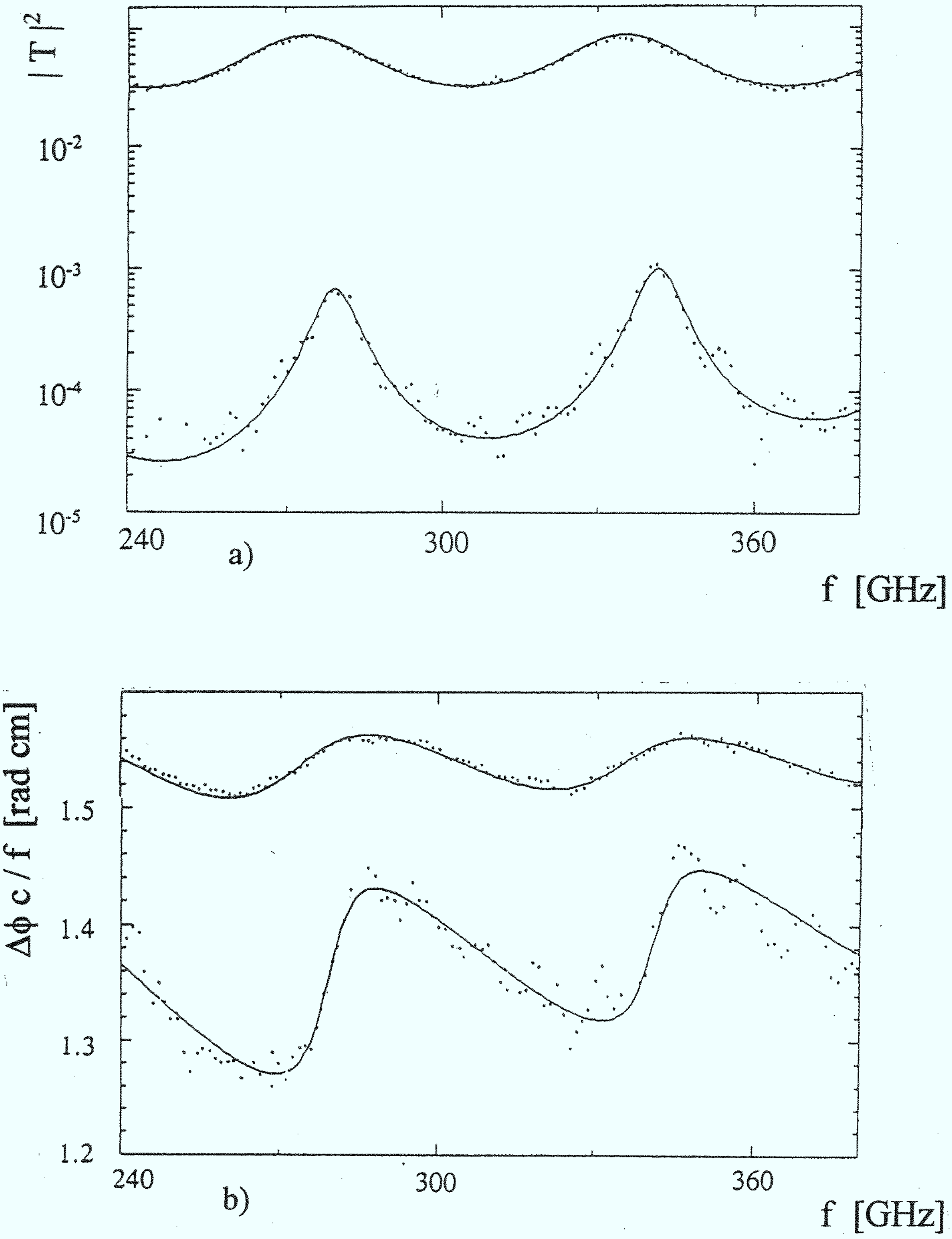

Fig. 3.9: Power attenuation (a) and phase shift (b) versus frequency of a 50 nm $YBa_2Cu_3O_{7-x}$ film on a 0.5 mm thick $NdGaO_3$ substrate at 300K (upper curve) and 6 K (lower curve). The dots represent the data points and the lines are fits to the data (from [66]).

3.2.3 Calorimetric measurements

Miller et al. used a calorimetric technique to determine the absorptivity from the radiation-induced temperature increase of an $YBa_2Cu_3O_{7-x}$ thin film sample between 1.5 and 21 THz [141, 142]. This technique is a useful extension of the far-infrared techniques to the low-frequency limit. The systematic uncertainty of this technique relies on the heat capacity of the substrate and the heat flow via the bonding wires. Recently, Basov et al. developed a calorimetric technique based on an amplitude-modulated far-infrared laser at 0.9 THz [143]. It should be emphasized that calorimetric techniques can only be used to determine the real part of the surface impedance.

3.2.4 Time domain spectroscopy

In principal, time domain spectroscopy is an elegant technique because of its ability to determine $Z_s(f)$ over a large frequency range from less than 50 GHz up to about 1 THz from one single spectrum per temperature value. Two different variants have been used to investigate HTS films, both for the first time at the AT&T Bell Laboratories. In both variants a picosecond light pulse is generated by a titanium-sapphire (or dye) laser, which is converted into a picosecond electrical pulse by a photoelectric switch. In the first variant the pulse is guided along an HTS coplanar line and detected after propagation [144]. In the second variant the electrical pulse is transformed into a quasioptical beam by a planar antenna [145, 146]. After passing through a thin unpatterned HTS film similar to the transmission spectroscopy described in Subsection 3.2.2, the beam is retransformed into a pulse by a second planar antenna, and then detected in a way similar to that of the first variant. The surface impedance as a function of frequency is determined by Fourier analysis of the transmitted pulse, which is dispersed upon passing through the HTS film. The accuracy of this technique, however, is quite poor in comparison to frequency domain spectroscopy.

Chapter 4

Surface impedance of $YBa_2Cu_3O_{7-x}$

Among the high-T_c cuprates the majority of the available microwave surface impedance data concern $YBa_2Cu_3O_{7-x}$. The first surface resistance measurements on bulk single crystals performed by Rubin et al. [147] and epitaxial thin films performed by Klein et al. [3] in 1988 revealed $R_s(77\,\mathrm{K})$ values approaching the resolution limit of the measurement systems. This resolution limit was already much below the surface resistance of copper, indicating a potential for the applicability of HTS films for passive microwave devices. Meanwhile the quality of films and bulk single crystals has been improved, but there are imperfections like lattice distortions, grain boundaries and point defects even in the best samples. However, in spite of some scattering of the data for different samples there are some general trends which are worth comparing to the theoretical models described in Chapter 2. Moreover, correlations of the surface impedance to imperfections like oxygen vacancies have brought insight into the physical origin of microwave absorption.

4.1 Temperature and frequency dependence of the surface resistance

.

In Fig. 4.1 typical $R_s(T)$ curves of epitaxial $YBa_2Cu_3O_{7-x}$ films measured at different frequencies are shown. All these films provide a high degree of c-axis orientation, i.e. the high frequency currents are oriented parallel to the ab-plane. The films have an oxygen stoichiometry close to O_7, i.e. the oxygen deficiency x is in general smaller than 0.1. The different deposition techniques are reviewed elsewhere [150, 151]. However, for a discussion of the surface impedance of films and single crystals some general aspects of HTS material preparation need to be discussed here. Epitaxial thin films (and bulk single crystals) are always grown close to the $YBa_2Cu_3O_{7-x}$ decomposition line in the oxygen partial pressure – temperature phase diagram [152]

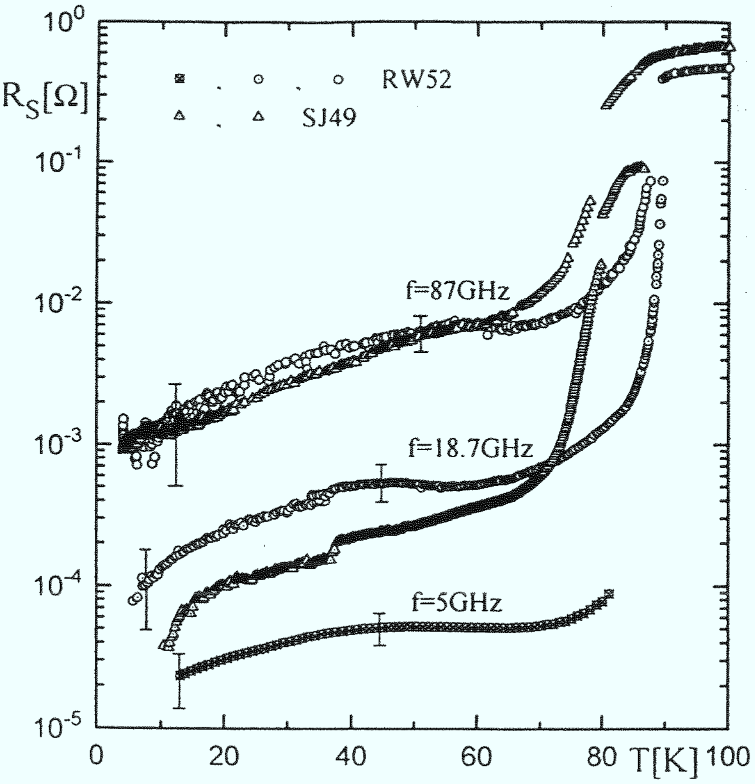

Fig. 4.1: Temperature dependence of R_s of c-axis oriented epitaxial $YBa_2Cu_3O_{7-x}$ films prepared by high-oxygen-pressure sputtering (RW52) and by electron beam evaporation (SJ49) at different frequencies (from [148])

(with the exception of post-annealed films, which in most cases are granular and therefore exhibit much higher microwave losses). The temperature above which $YBa_2Cu_3O_{7-x}$ decomposes decreases with decreasing oxygen (O_2) partial pressure from about 920°C at 1 bar. Among the different deposition techniques, the high-oxygen-pressure sputtering technique is operated at the highest oxygen pressure of a few millibar and therefore the highest growing temperature of about 760°C [48]. Pulsed laser ablation is performed at an oxygen pressure of about 0.1 mbar, and off-axis sputtering and evaporation techniques at about one order of magnitude lower pressure values, implying growing temperatures around 650°C for the latter [150, 151]. For all these techniques the film growth takes place in a temperature-pressure regime where the crystal structure of $YBa_2Cu_3O_{7-x}$ is tetragonal and the compound is not superconducting. The transition to the superconducting orthorhombic phase with $x \to 0$ is achieved by a slow cooling down from the deposition temperature to room temperature in one bar of oxygen or/and by post-annealing in activated oxygen. However, for films grown at an oxygen pressure below about 0.1 mbar even for fully oxygenated films ($x \to 0$) T_c is typically a few degrees lower and the c-axis lattice parameter is enlarged by a few tenths of a percent [153]. Bulk single crystals are grown at a pressure of 1 bar of O_2. Here the main difficulty is to achieve full and homogeneous oxygenation during the post-annealing treatment, since the

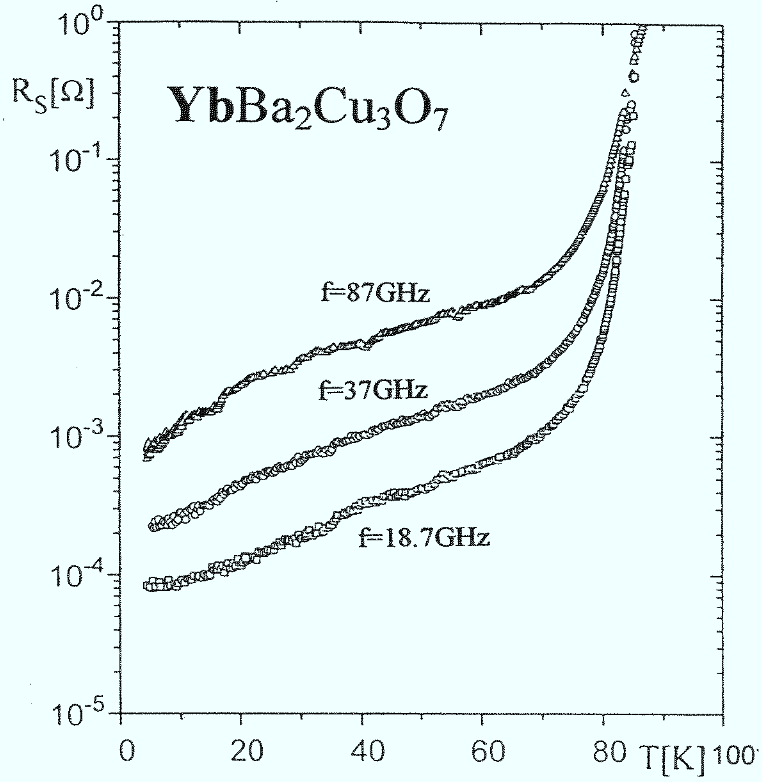

Fig. 4.2: Temperature dependence of R_s of c-axis oriented epitaxial $YbBa_2Cu_3O_{7-x}$ films prepared by high-oxygen-pressure sputtering at different frequencies (from [106]).

oxygen diffusity in $YBa_2Cu_3O_{7-x}$ at 400 to 500°C is very low. Therefore, most of the crystals possess oxygen deficiencies x of about 0.1. For microwave devices it is very important that films up to three inches in diameter with good microwave properties can be grown now by various sputtering techniques (see e.g. [155, 156]), homogeneous coatings up to 9 inches are even possible using a thermal evaporation technique [157].

According to Fig. 4.1, the film prepared by high-oxygen-pressure dc sputtering (sample RW52) exhibits a steep decrease of $R_s(T)$ just below T_c, a plateau-like behavior and a further reduction starting smoothly from the plateau at a temperature which increases with increasing frequency. The film prepared by thermal evaporation (sample SJ49) does not show the plateau at 18.7 GHz. At 87 GHz, where the plateau for the sputtered film already appears very close to the steep increase of $R_s(T)$ below T_c, both films exhibit a similar $R_s(T)$ behavior below 60 K. This is remarkable, because the two films differ strongly in T_c.

For all the deposition techniques discussed below, the surface resistance at 77 K converges to about 250 $\mu\Omega$ at 10 GHz. The frequnecy scaling behavior below about 100 GHz is given by $f^{1.8}$, at higher frequencies the frequency dependence becomes slightly weaker. It is worth emphasizing that for values of the film thickness below about 500 nm the surface resistance at 77 K is enlarged significantly according to Eq. 2.15.

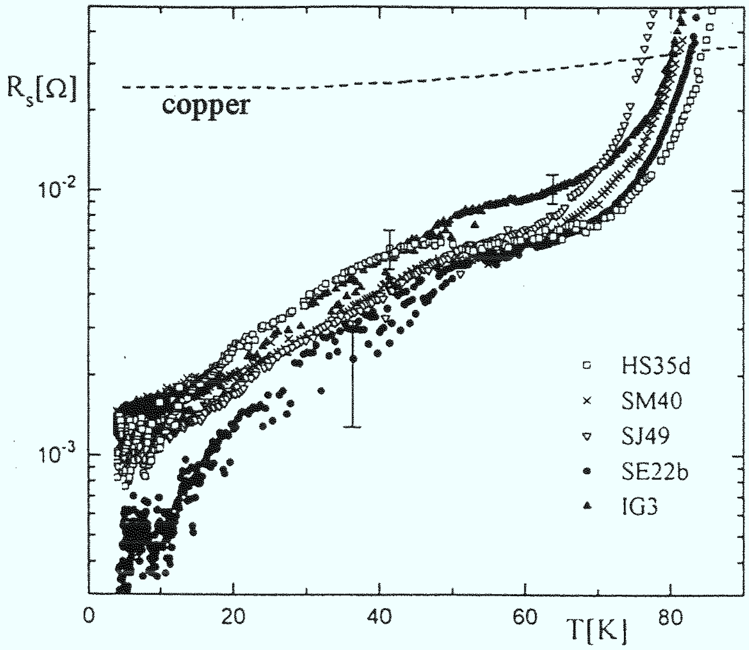

Fig. 4.3: Comparative study of $R_s(T)$ at 87 GHz for epitaxial c-axis oriented films prepared by different growing techniques: high-oxygen-pressure dc sputtering (HS35d), thermal evaporation (SM40), pulsed-laser deposition (SJ49), electron-beam evaporation (SE22b), and chemical vapor deposition (IG3) (from [148]).

Before giving a possible interpretation of the observed temperature dependences of R_s, some results are worth to be described in detail. Fig. 4.2 shows $R_s(T)$ of $YbBa_2Cu_3O_{7-x}$ thin films prepared by the same sputtering technique as sample RW52 in Fig. 4.1. Apparently, there is no plateau in $R_s(T)$, similar to the film prepared by thermal evaporation shown in Fig. 4.1. Again, the 87 GHz data seem to follow a universal $R_s(T)$ curve. The latter is even more obvious from Fig. 4.3 showing $R_s(T)$ from a comparative study of a large number of HTS films prepared by different growing techniques at 87 GHz. As shown in Fig. 4.4, the most pronounced plateau in $R_s(T)$ was observed for some bulk single crystals (labeled Bonn et al. [65]) and films prepared by high-oxygen-pressure sputtering (labeled Klein et al. [162]), in strong contrast to films prepared by off-axis sputtering (labeled Ma et al. [163]). However, as discussed in Section 4.3, there is a striking difference in the low-temperature behavior of R_s between bulk single crystals and films prepared by high-oxygen-pressure sputtering. For the bulk single crystals it was found that the $R_s(T)$ plateau disappears gradually upon doping the single crystal with Zn in the concentration range of 0.1% (Fig. 4.5).

The general trend apparent in the data described in Figs. 4.1-4.5 can be understood qualitatively with the extended two-fluid model by Bonn et al. (see Eq. 2.33), taking into account a sample-dependent impurity scattering rate τ_{res}^{-1}. Fig. 4.6a,b shows $R_s(T)$ at $f = 1, 10, 20, 50, 100$ GHz (from top to bottom) scaled by f^2 to 10 GHz

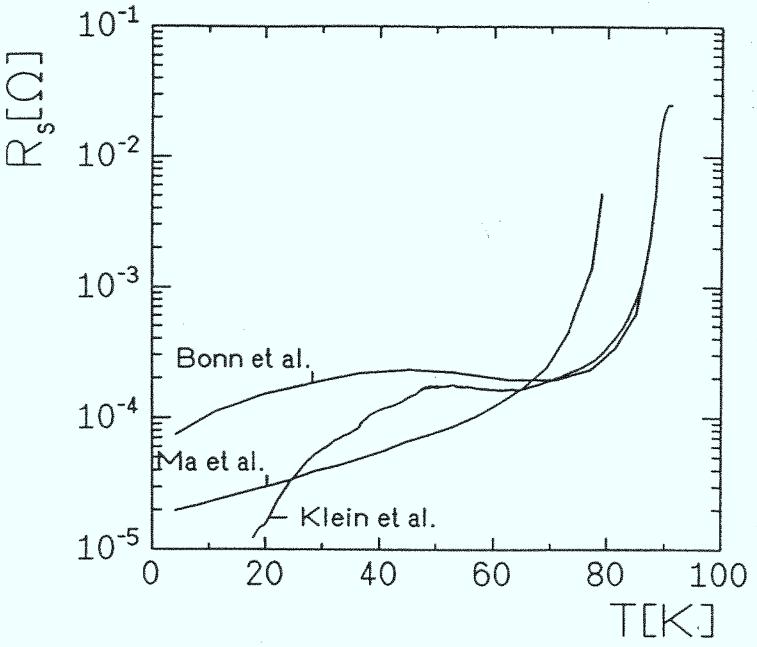

Fig. 4.4: $R_s(T)$ scaled by f^2 to 10 GHz for bulk single crystals (Bonn et al., f=35 GHz [65]), films prepared by high-oxygen-pressure sputtering (Klein et al., f=19 GHz [162]), and by off-axis sputtering (Ma et al., f=10 GHz [163]). The results of Klein et al. are corrected for finite thickness according to Eq. 2.15 (from [149]).

calculated from Eqs. 2.33 and 2.13 using $\lambda_L(0) = 150\,\mathrm{nm}$ and $n_q(T) = 1 - n_s(T) = (T/T_c)^2$. The main contribution to the temperature dependence of R_s is due to the temperature dependence of the quasiparticle scattering rate, which exhibits a strong temperature decrease just below T_c. From the analysis of surface impedance data on bulk single crystals by Eq. 2.33 Bonn et al. found an exponential temperature dependence of τ_q^{-1} [65] (see Fig. 2.4)

$$\tau_q^{-1} = 6 \cdot 10^9 s^{-1} \exp\left(\frac{T}{12\mathrm{K}}\right) + \tau_{res}^{-1} \tag{4.1}$$

which will be discussed in the next section. Using a residual scattering rate of e.g. $\tau_{res}^{-1} = 7 \cdot 10^{10}\,\mathrm{s}^{-1}$ the plateau-like behavior of $R_s(T)$ at low frequencies and the shift of the plateau to higher temperatures upon increasing the frequency are well described (Fig. 4.6a). In the case of a higher scattering rate of $10^{12}\,\mathrm{s}^{-1}$, however, the plateau disappears (Fig. 4.6b). The curves above about 50 GHz do not differ qualitatively for both values of τ_{res}^{-1}. In summary, these calculations indicate that the observed variation in the temperature and frequency dependence of R_s are likely to be related to different τ_{res}^{-1} values. However, so far it is only a classification scheme for $YBa_2Cu_3O_{7-x}$ films, and one can try to find qualitative relations between τ_{res}^{-1} and structural properties. Firstly, at $T = T_c$ the scattering rate τ_q^{-1} can be calculated according to Eq. 2.33 ($n_q = 1, n_s = 0$) from the dc conductivity of $2.5 \cdot 10^6\ (\Omega\mathrm{m})^{-1}$ for high-quality epitaxially grown $YBa_2Cu_3O_{7-x}$ films (corresponding to a dc resistivity

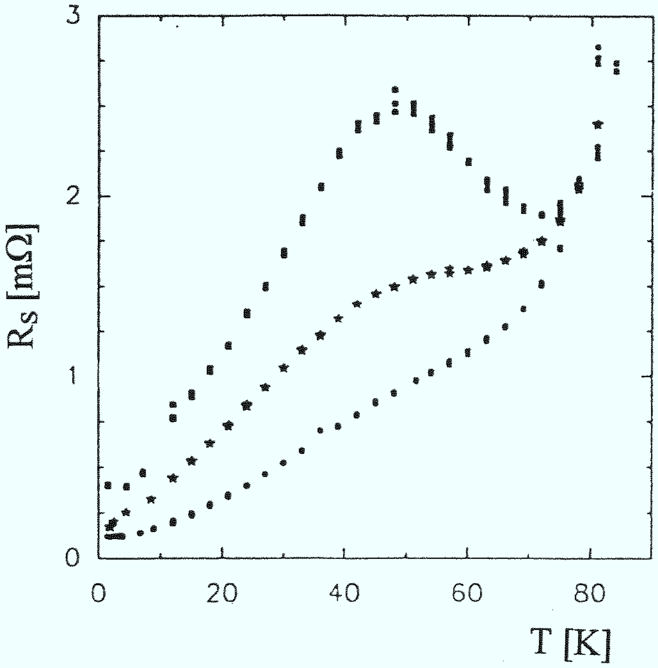

Fig. 4.5: $R_s(T)$ of bulk single crystals of $YBa_2Cu_3O_{7-x}$ at 34.8 GHz at different levels of Zn doping: pure (solid squares), 0.15% (stars), 0.31% (solid circles), (from [138]).

of 40 $\mu\Omega$). Using $\lambda_L = 150$ nm for the penetration depth τ_q^{-1} comes out to be $1.4 \cdot 10^{13}$ s^{-1}. This indicates a strong decrease of $\tau_q^{-1}(T)$ below T_c in order to reach the τ_{res}^{-1} values used for the calculations shown in Fig. 4.6a and b. The latter provide an estimate of the mean free path l at $T \to 0$. Using the relation $l = v_F/\tau_{res}^{-1}$ with $v_F \approx 2 \cdot 10^5$ m/s being the Fermi velocity of $YBa_2Cu_3O_{7-x}$ l comes out to be 2.8 μm and 200 nm for the curves in Fig. 4.6a and b, respectively. Since there is no estimate about the relation between defect density and mean free path (which depends on the kind of defect) only qualitative statements of correlations of measurable structural properties to the mean free path can be made. An indication of smaller mean free path values of films prepared by evaporation in comparison to those prepared by sputtering (Fig. 4.1) and bulk single crystals (Fig. 4.4) results from the enlargement of the c-axis lattice parameter in films prepared at lower temperatures and lower oxygen pressure. This enlargement can be explained by Y and Ba cation exchange, accompanied by oyxgen vacancies [153]. In $YbBa_2Cu_3O_{7-x}$ the small ionic radius of Yb^{3+} (0.098 nm in comparison to that of Y^{3+} (0.1015 nm [154]) gives rise to Yb vacancies even in bulk material [153]. Yb vacancies are a possible reason for the high degree of lattice strain observed in $YbBa_2Cu_3O_{7-x}$ films [106]. This lattice strain is assumed to increase the residual scattering rate. Finally, referring to Fig. 4.5, Zn substitutes for Cu in the CuO_2 planes [158] are considered to decrease the scattering rate as well, consequently reducing the height of the maximum in $R_s(T)$.

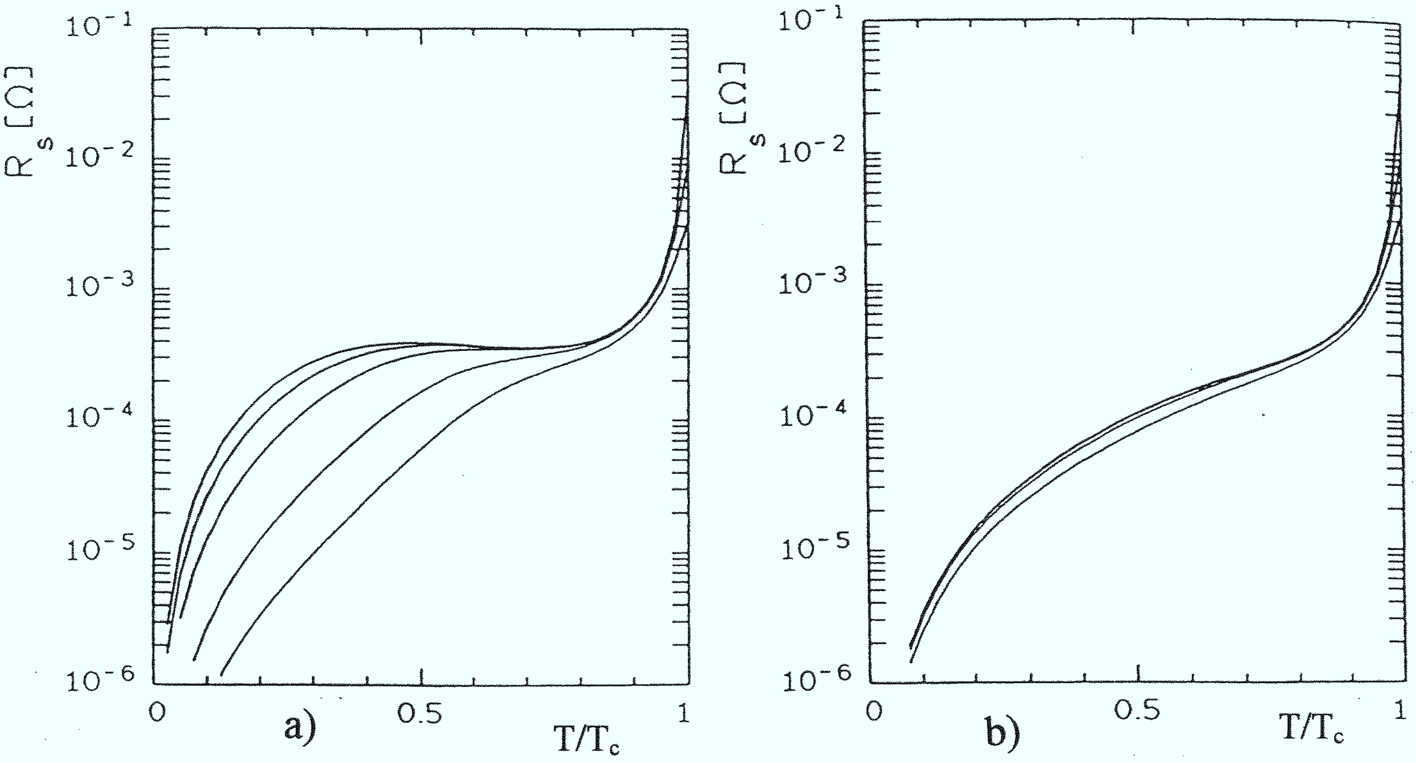

Fig. 4.6a,b: $R_s(T/T_c)$ at 1, 10, 20, 50, 100 GHz scaled by f^2 to 10 GHz calculated from Eq. 2.33 and 2.13 using $\tau_{res}^{-1} = 7 \cdot 10^{10}\,\mathrm{s}^{-1}$ (a) and $\tau_{res}^{-1} = 1 \cdot 10^{12}\,\mathrm{s}^{-1}$ (b) (for detailed explanation see text).

4.2 Dynamic conductivity and quasiparticle scattering rate

From the results shown in the previous section there is experimental evidence for a strong decrease of the quasiparticle scattering rate below T_c, as suggested by Bonn et al. within their modified two-fluid model [65]. However, questions arise about the validity of this model, as it is not based on microscopic calculations. In particular, as explained in Section 2.2.1, the normalization condition $n_q(T) + n_s(T) = 1$ might not be fulfilled. Therefore, measurements of $\sigma_1(T)$ over a large range of frequencies up to values above $\omega\tau_q = 1$ are very important.

Fig. 4.7 shows $\sigma_1(T)$ from 165 GHz to 600 GHz (measured by the submillimeter-wave transmission spectroscopy described in Section 3.2.2) of an $YBa_2Cu_3O_{7-x}$ thin film of 60 nm thickness grown epitaxially on $NdGaO_3$ by high-oxygen-pressure dc sputtering. It should be emphasized that such very thin films have more defects than thicker films [48], and so far microwave surface resistance measurements at 19 GHz have not revealed a pronounced plateau. Nevertheless, the films exhibit a maximum in $\sigma_1(T)$, which is shifted to higher temperatures upon increasing the frequency. (Obviously, according to Eq. 2.14 a maximum in $\sigma_1(T)$ implies a plateau in $R_s(T)$. The $R_s(T)$ data shown e.g. in Fig. 4.4 lead to a maximum in σ_1 which is much higher than the

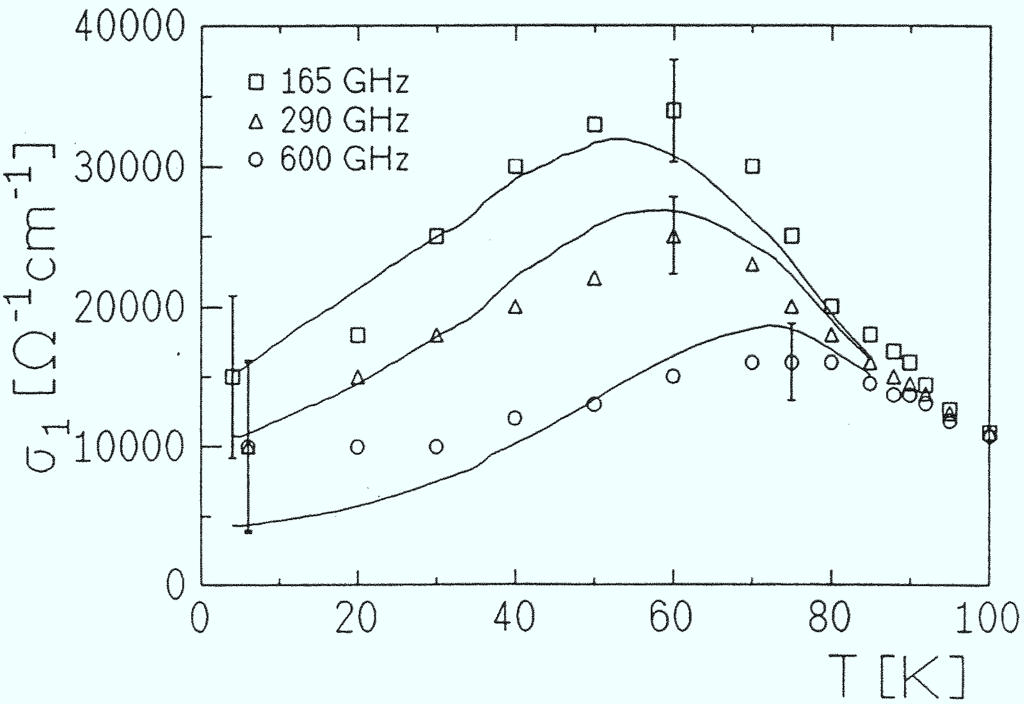

Fig. 4.7: Real part of the dynamic conductivity versus temperature of a 60 nm thick $YBa_2Cu_3O_{7-x}$ film. The solid lines represent a fit of Eq. 2.33 ($n_q(T)$ replaced by $n_q(T) + n_{res}$, see text) using $\tau_q(T)$ from Fig. 4.9 (solid line), $n_q(T) = 1 - n_s(T)$ from an additional $\lambda_L(T)$ measurement at 19 GHz, and $n_{res} = 0.2$ (from [159]).

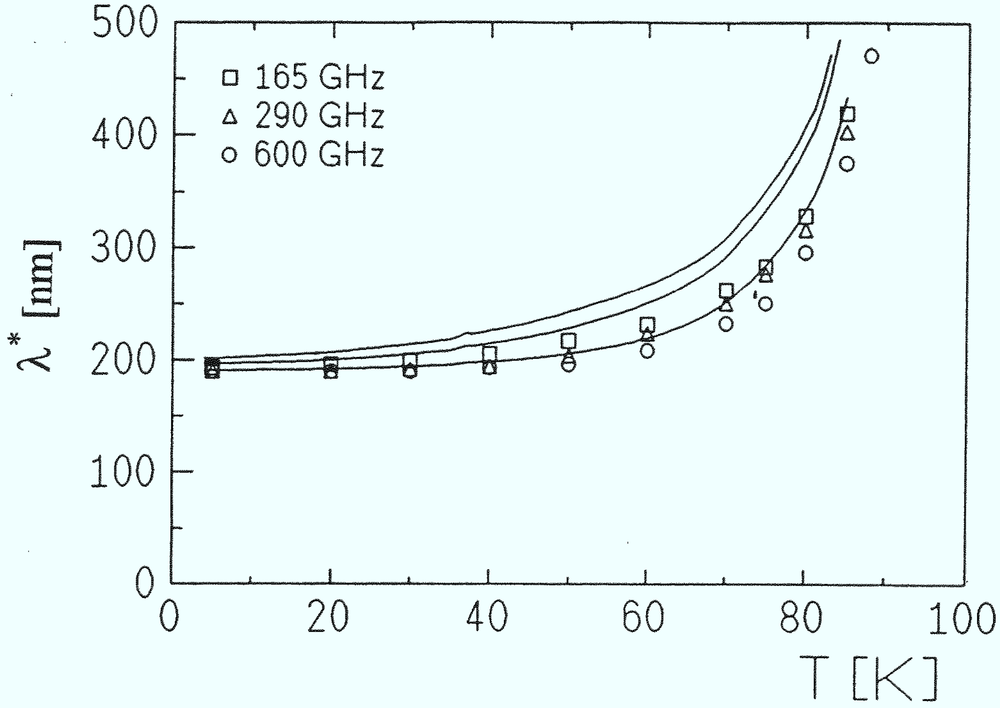

Fig. 4.8: Temperature dependence of the penetration depth $\lambda^* = 1/\sqrt{\omega\mu_0\sigma_2}$ for the same sample as shown in Fig. 4.7 and fits of Eq. 2.33 (solid lines) using the same parameters as in Fig. 4.7 (from [159]).

maxima shown in Fig. 4.7.) Fig. 4.8 shows the $\lambda^*(T) = 1/\sqrt{\omega\mu_o\sigma_2(T)}$-values for the same sample measured by the submillimeter-wave spectroscopy. (The quantity λ^* is a measure of the imaginary part of the conductivity and is slightly larger than the magnetic field penetration depth $X_s/(\omega\mu_0)$ at temperatures close to T_c, see Eqs. 2.13 and 2.14.) From the modified two-fluid model a frequency dependence of λ^* is expected, since the denominator in Eq. 2.33 provides a frequency-dependent contribution to the imaginary part of σ. Similar to Eq. 2.34, the frequency dependence of λ^* at high frequencies can be used to determine τ_q^{-1} independently of $n_q(T)$ (in contrast to Eq.2.34, here the normalization condition is required). According to Fig. 4.9, the analysis based on σ_1 and λ^* as well leads to similar $\tau_q^{-1}(T)$ curves, which decrease more weakly in temperature in comparison to the curve determined by Bonn et al. (dashed line). Below about $T_c/2$, Eq. 2.33 is not applicable because of residual losses apparent in the $\sigma_1(T)$ data in Fig. 4.7. In order to get an appropriate fit of Eq. 2.33 to the experimental $\sigma_1(\omega, T)$ and $\lambda^*(\omega, T)$ data (full lines in Fig. 4.7 and 4.8), $n_q(T)$ needs to be replaced by $n_q(T) + n_{res}$. This additional parameter appears to be justified under the assumption of additional unpaired charge carriers with temperature-independent density n_{res} and the same temperature-dependent scattering rate as the quasiparticles. The $\tau_q^{-1}(T)$ data represented by the solid line in Fig. 4.9 were used for the fit. Within the experimental errors the σ_1 data are well described, but the λ^* data exhibit a weaker frequency dependence in comparison to

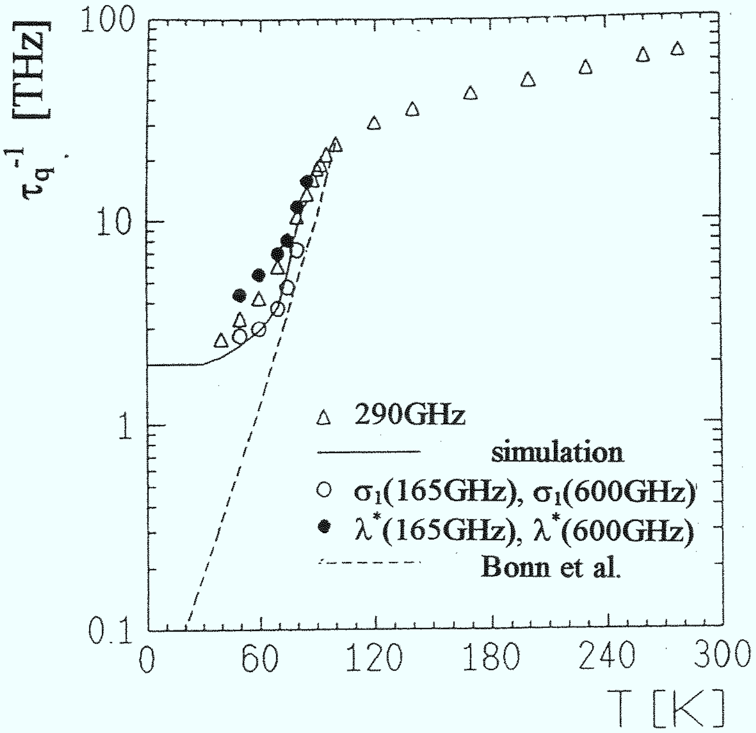

Fig. 4.9: Temperature dependence of τ_q^{-1} as determined by Eq. 2.34 from the σ_1 data, and similarly from the λ^* data shown in Figs. 4.7 and 4.8. The dotted lines represent results from Bonn et al. on bulk single crystals [65], the values given by the solid line were used for the fits shown in Figs. 4.7 and 4.8 (from [159]).

the model. Interestingly, for a second sample with slightly higher peaks in $\sigma_1(T)$ the discrepancies are more pronounced even for σ_1. This is a hint that for samples with lower residual scattering rate density of state effects, which are not considered in the two-fluid model, become more important.

From a microscopic point of view the two-fluid model is justified only in the gapless regime (see Section 2.2.1). Gaplessness at elevated temperatures is initiated by pair breaking due to phonons (or other thermal excitations), as predicted within the two-gap picture of Kresin and Wolf (see Fig. 3.5a in Section 2.2.2) and is very likely for a strongly anisotropic *s*-wave or *d*-wave order parameter. Experimentally, there is evidence for pair breaking since tunneling [160] and far-infrared reflectivity data [58] indicate a "filling up" of the "gap" (i.e. an energy range below a pronounced maximum in the density of states) upon increasing the temperature above about 30 K. Therefore, in order to discuss density of state effects in surface impedance data, the temperature dependences at $T << T_c$ will be analyzed in the next section.

Besides employing the two-fluid model several attempts were made to fit $R_s(T)$ data within microscopic theories. Within *d*-wave models $R_s(T)$ measured for bulk single crystals was fitted successfully from 4 K to T_c, if an exponential temperature decrease of τ_q^{-1} (Eq. 4.1) plus a residual surface resistance is introduced phenomenologically into the theory [87, 89, 32]. It should be emphasized that the explanation of this exponential decrease by spin fluctuations (see Section 2.2.2) does not mean that spin fluctuations generate superconductivity. The strong temperature decrease of $R_s(T)$ at $T << T_c$ observed for the films prepared by high-oxygen-pressure sputtering, however, cannot be explained by the *d*-wave model. Therefore, so far no conclusion about the symmetry of the order parameter can be drawn from surface impedance measurements.

4.3 Low temperature studies of R_s and λ_L

The low temperature regime of R_s and λ_L is strongly sample-dependent. The results reported in the literature range from $\exp(-\alpha T)$ over quadratic to linear dependences. In spite of these discrepancies, the literature data indicate a finite limitation of R_s at $T << T_c$, which scales slightly weaker with frequency than f^2. Fig. 4.10 from [148], which also contains some results of polycrystalline bulk material (open symbols), shows a respresentative collection of the lowest $R_{res} = R_s(T \leq 4.2\ K)$ values for $YBa_2Cu_3O_{7-x}$ thin films (solid symbols) and bulk single crystals (crosses). The similarity of the R_{res} values to R_s of niobium has to be considered as accidental, because niobium exhibits a strong temperature dependence of R_s at 4 K, i.e. for niobium R_s at 4 K is not dominated by residual losses. The level of the residual surface resistance of approximately 25 $\mu\Omega$ at 10 GHz is about a factor of three above the intrinsic limitation for a *d*-wave superconductor (Eq. 2.38, Section 2.2.3) and more than a factor of 10 above the limit given by residual granularity (see Section 2.2.1). Assuming gaplessness, one can estimate the normalized (with respect to $T = T_c$) number of unpaired charge carriers (or density of states at the Fermi energy). Using $R_{res} = 25\ \mu\Omega$ at 10 GHz and $\lambda_L = 150$ nm the residual conductivity $\sigma_{res} = 2R_{res}/(\omega^2\mu_0^2\lambda_L^3)$ (see Eq. 2.14) comes out to be $2.3 \cdot 10^6\ (\Omega m)^{-1}$, which is about its value at $T = T_c$. According to the calculations shown in Fig. 4.6a,b the quasiparticle scattering rate decreases by values between one and three orders of magnitude, depending on the quality of the sample. This means the observed residual losses can be explained by a normalized density of unpaired charge carriers of the order of 10^{-3} to 10^{-1}.

As already described in Section 4.1, films prepared at low oxygen pressure and temperature generally exhibit an $R_s(T)$ behavior without plateau. Fig. 4.11 and 4.12 show the low temperature behavior of σ_1 and $\delta\lambda_L = \lambda_L(T) - \lambda_L(0)$ of such films (grown by off-axis sputtering). Similar to recent results on films prepared by thermal evaporation [165], λ_L is quadratic in temperature with small deviations below 5 K and σ_1 is linear in temperature. It is obvious that pure *s*-wave superconductivity cannot explain these temperature dependences. The *d*-wave model, however, gives a quadratic T dependence for σ_1 and λ_L for high values of τ_{res}^{-1}. This is in contradiction to the results shown in Figs. 4.11 and 4.12. According to Fig. 2.8 a linear dependence of σ_1 only results for the parameter range of $\omega\tau_{res} \approx 1$, corresponding to τ_{res}^{-1} values of about $1.6 \cdot 10^{-10}\ s^{-1}$ at f =10 GHz. This already implies a pronounced plateau in $R_s(T)$. However, the linear T dependence of R_s and λ_L observed for bulk single crystals with pronounced R_s plateau (see Fig. 4.16, Section 4.4) is in favor of the

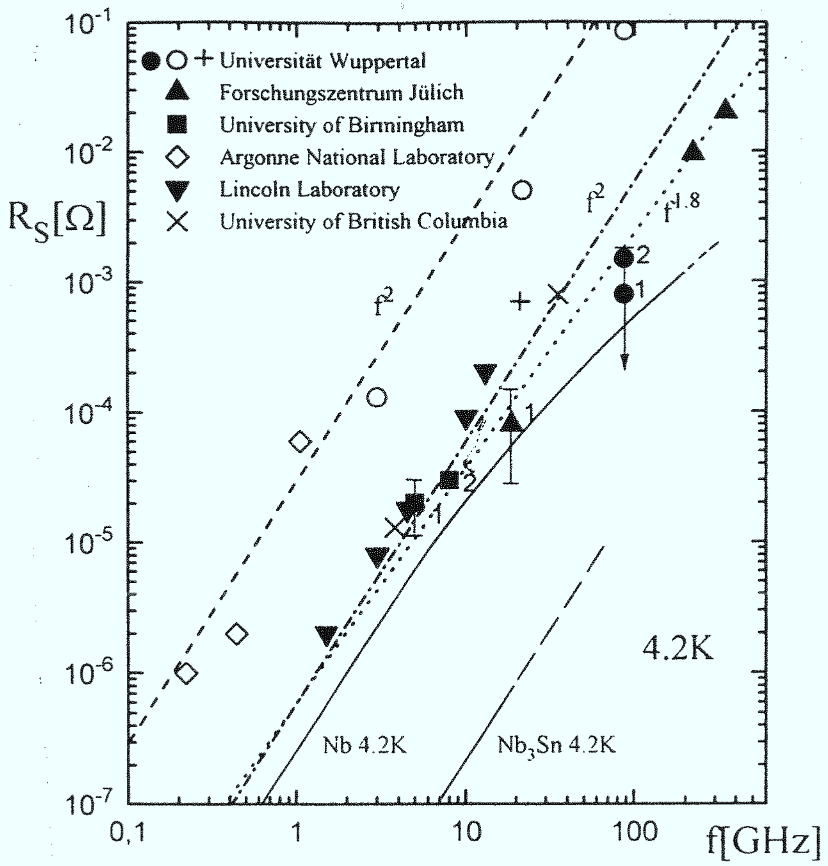

Fig. 4.10: Representative collection of the lowest $R_{res} = R_s(T \leq 4.2\ \mathrm{K})$ values for epitaxial $\mathrm{YBa_2Cu_3O_{7-x}}$ thin films (solid symbols), bulk single crystals (crosses), and polycrystalline material (open symbols), marking the laboratories where the samples were prepared. The solid lines represent $R_s(4.2\ \mathrm{K})$ of niobium and $\mathrm{Nb_3Sn}$ (from [148]).

d-wave scenario.

The experimental data of thin films prepared by high-oxygen-pressure sputtering indicate a small, but finite energy gap, and therefore seem to be in contradiction to *d*-wave superconductivity. Fig. 4.13 from [162] shows the low temperature regime of $R_s(T)$ of two fully oxygenated ($x \to 0$) $\mathrm{YBa_2Cu_3O_{7-x}}$ films (triangles and squares). These results are consistent with an $\exp(-\Delta/kT)$ dependence of $R_s(T)$ (see Eq. 2.22) with Δ values ranging from 5 meV to 10 meV. At higher temperatures the $R_s(T)$ curves of these films exhibit a pronounced plateau indicating low values of τ_{res}^{-1} (see Fig. 4.4). A possible explanation for the observed temperature dependences within the *d*-wave model is relaxation effects, which give rise to a flat $R_s(T)$ dependence at $T << T_c$ (see Fig. 2.28).

The crosses in Fig. 4.13 show $R_s(T)$ of an oxygen-deficient film of $\mathrm{YBa_2Cu_3O_{7-x}}$ with $x \approx 0.2$ prepared by post-annealing at reduced oxygen pressure from an initially fully oxygenated film. Obviously, R_s exhibits a linear T dependence, similar

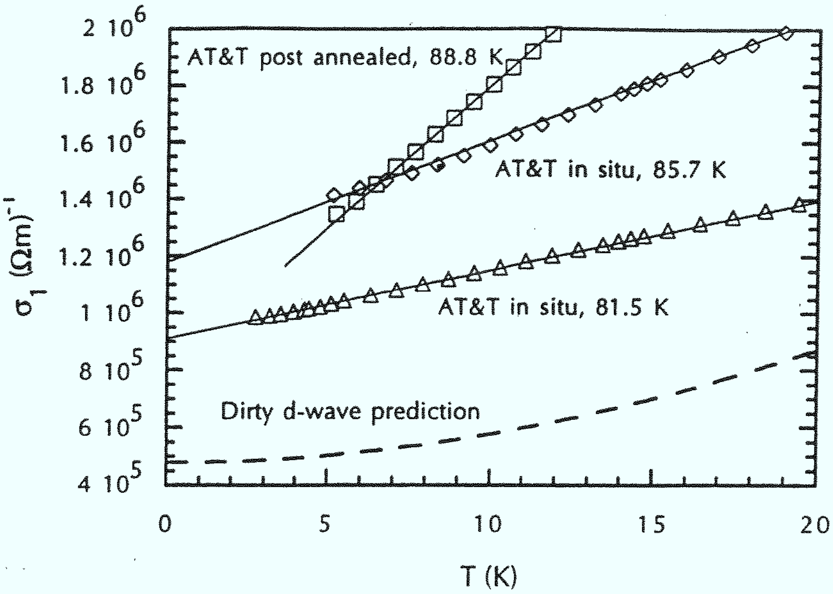

Fig. 4.11: Low temperature regime of σ_1 for films prepared by off-axis sputtering (triangles and rhombuses). The dashed line represents a calculation within d-wave theory for a high scattering parameter of $\gamma = 20$ K. The squares correspond to a granular film prepared by a post-annealing procedure (from [161]).

to the slightly oxygen-deficient single crystals. The temperature dependence of the penetration depth at $T << T_c$ was measured for the same films and is plotted in Fig. 4.14. The solid line labeled by 1 represents a fit of strong-coupling calculations within the two-band model of Kresin and Wolf, based on electron-phonon interaction and an s-wave order parameter [85] (see Section 2.2.2). The parameters of the fit were chosen to give the experimentally observed T_c of 90 K. The coupling parameter between chains and plains ($\Lambda_{a,b}$, see section 2.2.2) does not severely affect T_c, but fixes the value of the induced energy gap Δ_b at about 6 meV. The induced energy gap defines the $\exp(-\Delta_b/kT_c)$ temperature dependence of $\delta\lambda_L$ at $T << T_c$. The solid lines labeled by 2 to 4 were calculated upon introducing pair breaking by magnetic scattering with scattering rates Γ_m (in equivalent temperatures, see Subection 2.2.2) of 30 K (2), 60 K (3) and 90 K (4). Above Γ_m =90 K the slope of $\delta\lambda_L$ decreases and $\delta\lambda_L(T)$ becomes quadratic in temperature [85]. The linear dependence of curve (4) corresponds to the onset of gaplessness, i.e. the density of states at the Fermi energy becomes finite. This was estimated to be at an oxygen deficiency of $x \approx 0.1$. Qualitatively, these calculations can explain the discrepancy between the exponential T dependences observed for films prepared by high-oxygen-pressure sputtering and the linear dependences observed for bulk single crystals. In contrast, films prepared by thermal evaporation exhibit a quadratic temperature dependence of $\delta\lambda_L$, independent of the oxygen deficiency x [165]. One possible explanation is that cation disorder creates gaplessness in the CuO_2 planes. Independent of sample quality, however, $\lambda_L(T \rightarrow 0)$ increases gradually upon increasing x from $x = 0$, without plateaus as apparent in the dependence of T_c on x [51]. This observation

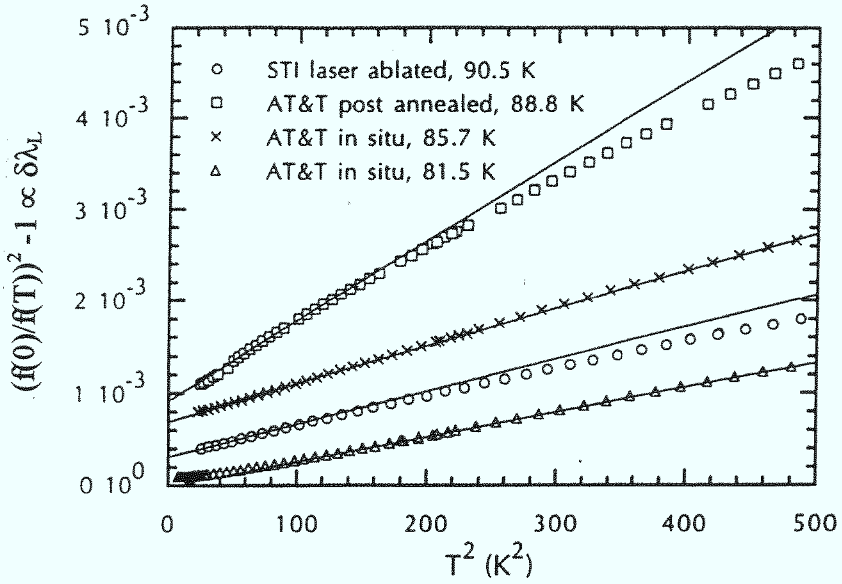

Fig. 4.12: Low temperature regime of $\delta\lambda_L$ (proportional to change of resonance frequency f) a function of T^2 for the same films as shown in Fig. 4.11 (from [161]).

supports the contribution of the CuO chains to the total density of states and their active role for the microwave response.

This active role is also clearly demonstrated by Fig. 4.15, which shows $R_s(T)$ at 19 GHz of an oxygen-deficient $YBa_2Cu_3O_{7-x}$ film with $x \approx 0.2$ after post-annealing at temperatures between 250 and 100°C and subsequent quench cooling. At such low annealing temperatures the oxygen content of the CuO chains is not affected, as indicated by similar T_c values in the $R_s(T)$ curves. However, the ordering of oxygen vacancies is expected to be improved at lower annealing temperatures, if the oxygen mobility is high enough [164, 166, 167]. The observation of a reduction of $R_s(T)$ upon improving the oxygen ordering indicates that the dominant effect of the CuO chains is not a reduction of the mean free path, but a reduction of the density of states at the Fermi energy. Qualitatively, this is expected from Fig. 2.5b if one assumes that magnetic pair breaking becomes stronger if the oxygen vacancies are disordered.

Orbach et al. studied the x dependence of R_s of oxygen deficient $YBa_2Cu_3O_{7-x}$ within the 90 K plateau for films prepared by laser ablation, which typically provide intermediate τ_{res}^{-1} values [167]. Basically, R_s first increases and then decreases with increasing x. This indicates that a complicated combination of CuO-chain density of states and quasiparticle scattering rate determines the surface resistance of oxygen-deficient $YBa_2Cu_3O_{7-x}$.

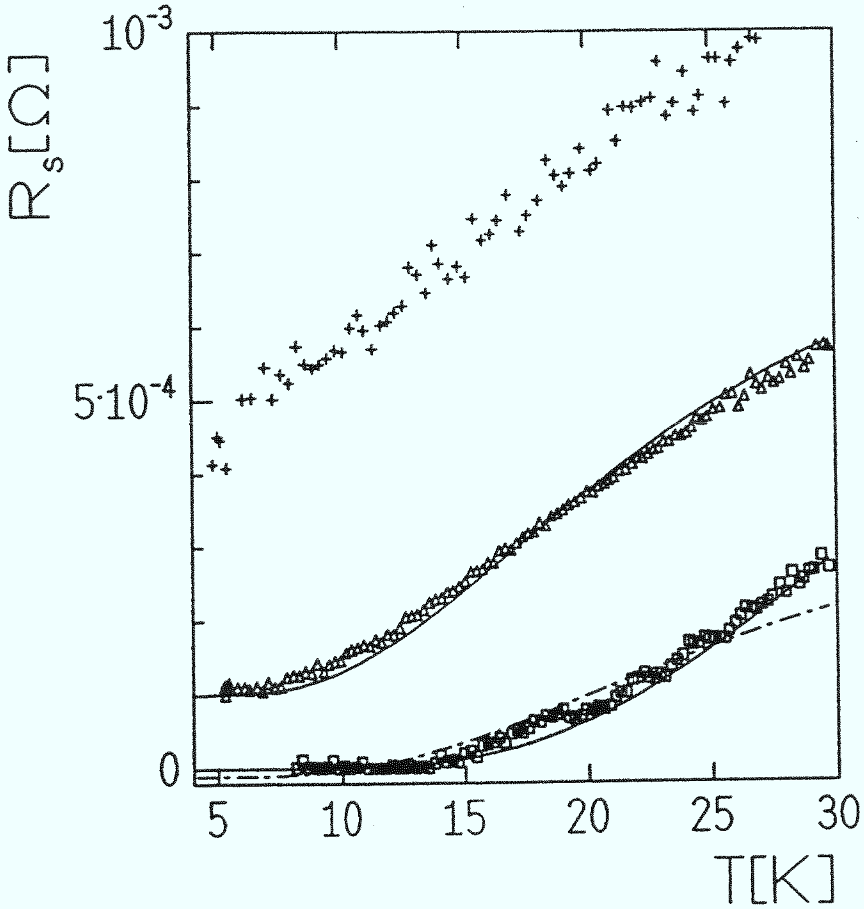

Fig. 4.13: Low temperature regime of $R_s(T)$ for $YBa_2Cu_3O_{7-x}$ thin films prepared by high-oxygen-pressure dc sputtering with $x \rightarrow 0$ (fully oxygenated, squares and triangles) and $x \approx 0.2$ (oxygen-deficient, crosses). The solid/dashed-dotted lines represent fits of the low temperature BCS approximation (Eq. 2.22) using energy gaps between 5 and 10 meV (from [162]).

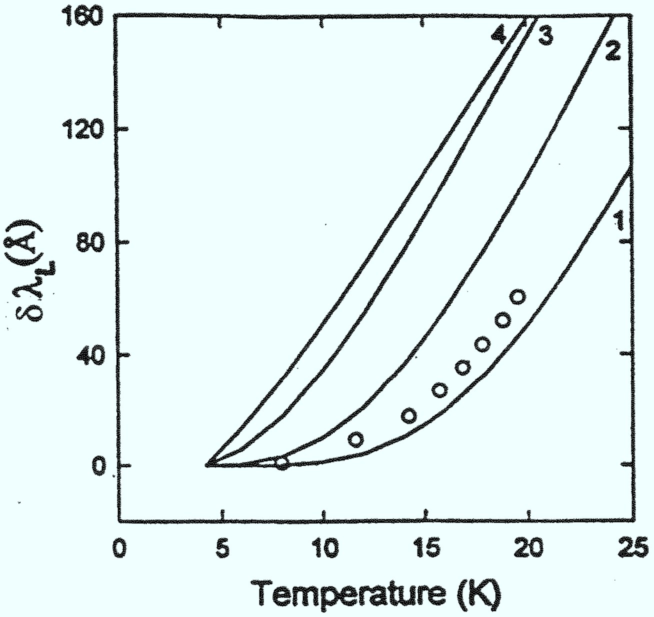

Fig. 4.14: Low temperature regime of $\delta\lambda_L$ measured for the sample labeled by squares in Fig. 4.13. The solid line labeled by 1 represents a fit of strong coupling calculations within the two-band model of Kresin and Wolf, based on electron-phonon interaction and an s-wave order parameter. The solid lines labeled by 2 to 4 were calculated upon introducing pair breaking by magnetic scattering with scattering energies Γ_m (in equivalent temperatures) of 30 K (2), 60 K (3) and 90 K (4) (see text, from [85]).

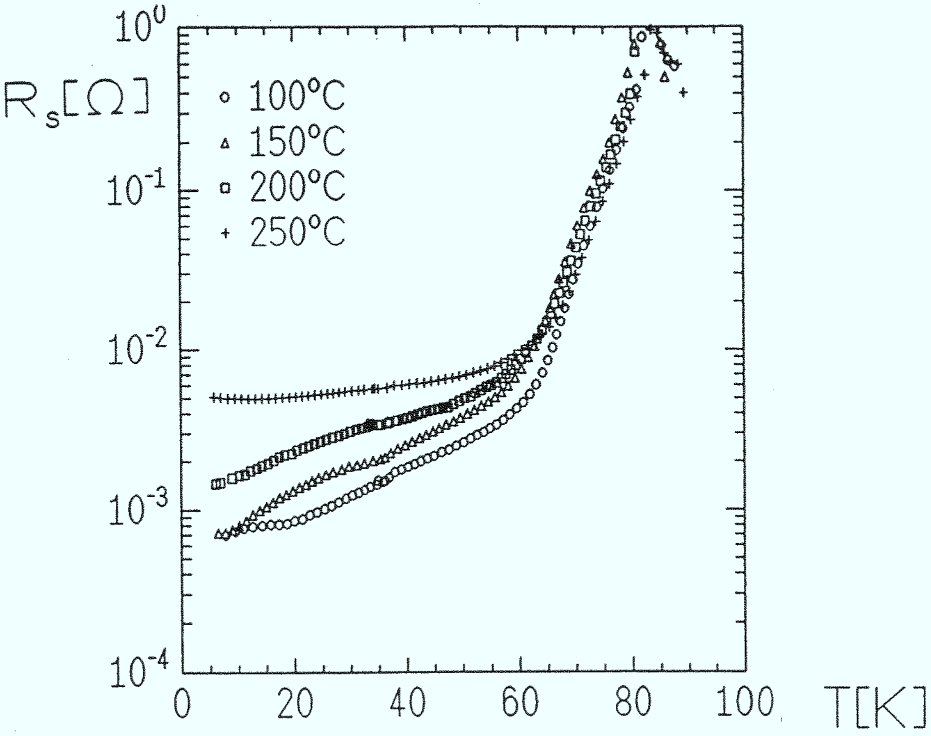

Fig. 4.15: $R_s(T)$ at 19 GHz of an oxygen-deficient $YBa_2Cu_3O_{7-x}$ film with $x \approx 0.2$ after post-annealing at 250°C (crosses), 200°C (squares), 150°C (triangles), and 100°C (circles) and subsequent quench cooling (from [164]).

4.4 Anisotropy of the surface impedance

The layered structure of the cuprates results in a strong anisotropy of the transport properties (see Section 2.2). In particular, for $YBa_2Cu_3O_{7-x}$ the London penetration depth is a factor of five larger for screening currents perpendicular to the ab-plane [52]. This already implies an anisotropic surface impedance. The surface impedance for rf currents along the c-direction can either be determined by measuring an a-axis oriented $YBa_2Cu_3O_{7-x}$ film with any of the available techniques [169] (see Chapter 3) or by measuring a bulk single crystal by a cavity perturbation technique (Section 3.1.5) with the c-axis perpendicular and parallel to the rf-magnetic field. The a-axis oriented films investigated by Hylton [169] exhibit a granular microstructure with the c-axis aligned either along the [100] or the [010] direction of the substrate. Similar to the c-axis oriented films grown by the same off-axis sputtering technique (Figs. 4.11 and 4.12) $R_s(T)$ exhibit a T^2 dependence at $T < 50$ K. The absolute values are 80 $\mu\Omega$ at 4 K and 10 GHz, which is only a factor of 2 to 3 above the lowest values for c-axis oriented films (see Fig. 4.10). However, the temperature increase is very strong resulting in significantly higher R_s values at higher temperatures. This behavior can be explained within the weak-coupling grain model (Eq. 2.35), i.e. the observed temperature dependences reflect the temperature dependences of the critical current density of the weak links [68].

For bulk single crystals, however, the $R_s(4\,\mathrm{K})$ values at 10 GHz are below 50 $\mu\Omega$ for the ab-direction and 5 mΩ for the c-direction [170]. It should be emphasized

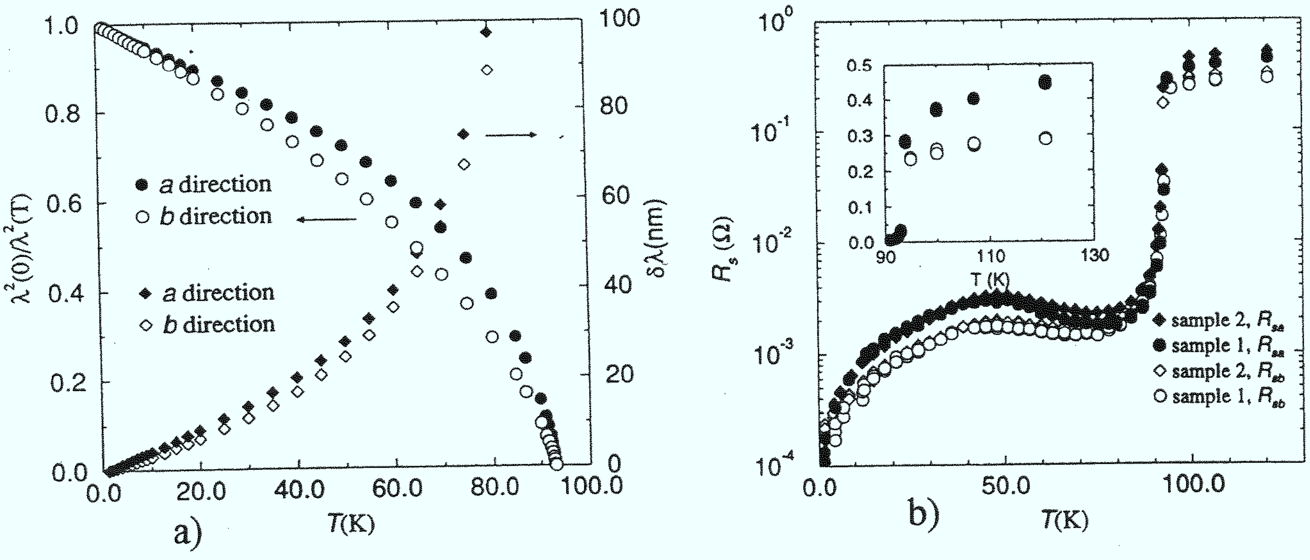

Fig. 4.16: Change of the penetration depth with temperature, $\lambda_L^2(0)/\lambda_L^2(T)$ and $\delta\lambda_L = \lambda_L(T) - \lambda_L(0)$ (a), as well as surface resistance $R_s(T)$ at 35 GHz (b) for rf currents oriented in a and b direction. The insert in (b) represents the dc-resistivity. The measurements were performed on detwinned bulk single crystals of $YBa_2Cu_3O_{6.95}$ (from [168]).

that there is a large uncertainty for the data in *c*-direction, because the demagnetization factor of the platelike single crystals (with the *c*-axis oriented perpendicular to the plate) is very high. Nevertheless, both $\delta\lambda_L$ and R_s exhibit a linear T dependence below about 30 K for both directions.

Due to the presence of the CuO chains as a conducting subystem (see Section 2.2.2) one also expects an *ab*-anisotropy of the surface impedance which can only be observed for untwinned $YBa_2Cu_3O_{7-x}$. Bulk single crystals can be detwinned by applying uniaxial pressure. For detwinned crystals a strong *ab*-anisotropy of the normal-state resistivity [57] and the plasma edge in the optical reflectivity (which defines the charge carrier density) was reported [59, 171]. Fig. 4.16a and b shows $\lambda_L^2(0)/\lambda_L^2(T)$, $\delta\lambda_L(T)$ and $R_s(T)$ at 35 GHz (b) for the *a* and *b* direction [168], indicating linear temperature dependences for R_s and $\delta\lambda_L$ in both directions. The lower values of $R_{s,b}(T)$ and $\delta\lambda_{L,b}(T)$ can be explained by the smaller $\lambda_L(0)$ values in *b* direction [171], which is most likely to be a result of an induced superconducting state in the CuO chains (see Section 2.2.2). It is interesting to note that for the gapless case the density of states exhibits a similar energy dependence for both bands (Fig. 2.5a), from which one expects similar dependences for $\delta\lambda_L$ in both directions. Therefore, in order to get a quantitative understanding of the observed *ab*-anisotropy the effect of induced superconductivity needs to be worked out for anisotropic order parameters as well.

4.5 rf field dependence of Z_s

The dependence of Z_s on the amplitude of the rf magnetic field is very important for the applicability of HTS films at elevated levels of rf power. In spite of this importance, to date no systematic studies as for the temperature dependence have been performed. In particular, from the available data it remains unclear which growing technique provides the weakest dependence of R_s on the amplitude of the rf magnetic field H_{rf}. The scarcity of the data is a result of the experimental difficulties connected with meaningful $Z_s(H_{rf})$ measurements. Basically, there are two experimental approaches which have been used successfully. First, stripline or coplanar resonators can be driven to the field limit by levels of rf-power much below one watt. However, as a result of the strong field enhancement effects at the edges (see Fig. 3.6 in Section 3.1.4), the H_{rf} values measured by planar resonators are representative for the edges, which are possibly degraded by the patterning procedure. The second possibility is dielectric resonators with sufficiently high quality factors, as described in Subsection 3.1.2. This technique is more representative of the "intrinsic" film properties. The third technique are planar disk resonators operating in modes without current enhancement at the edges (see Subsection 3.1.4).

Fig. 4.17 shows $R_s(H_{rf})$ of a film prepared by high-oxygen-pressure dc sputtering [48] measured at 1.5 GHz using a stripline resonator technique as described in [127]. Below a certain temperature-dependent H_{rf} level the data can be fitted with an H_{rf}^2 dependence, as predicted by Eq. 2.35. As described in detail in [71], both the

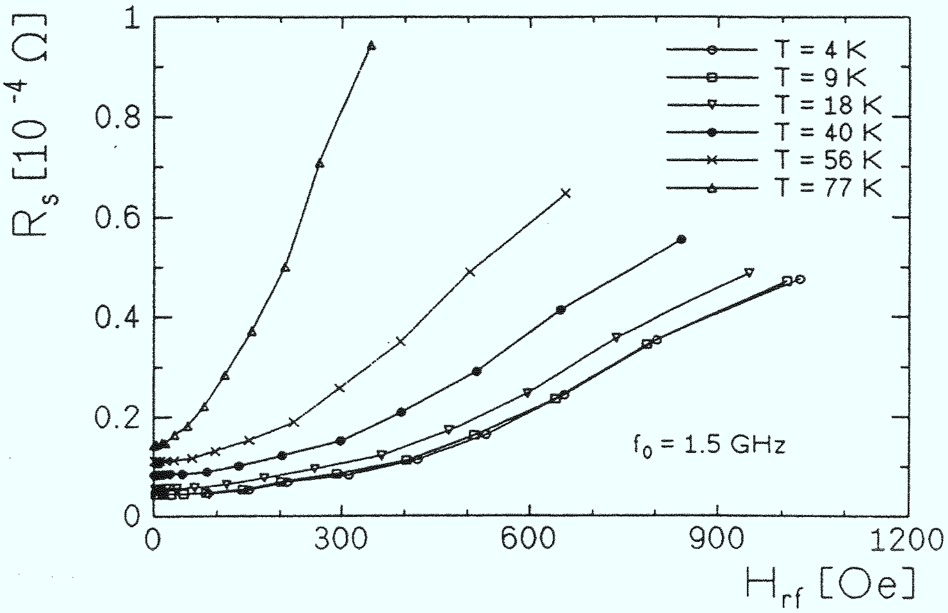

Fig. 4.17: Surface resistance versus rf magnetic peak field at 1.5 GHz and different temperatures, measured with a stripline resonator fabricated from an $YBa_2Cu_3O_{7-x}$ film prepared by high-oxygen-pressure dc sputtering (from [172]).

$\lambda_L(H_{rf}$,T) and the $R_s(H_{rf}, T)$ data are consistent with the weak-coupling grain model (Eq. 2.35 and 2.36, Section 2.2.1). The parameters used for the fit are critical current densities of the order of $5 \cdot 10^6$ A/cm^2 and average grain size of about 5 μm. This relatively large value of the grain size results from the weak dependence of λ_L on H_{rf} (Fig. 4.18). However, in order to fit the $R_s(H_{rf})$ values one has to assume I_cR products of only a few millivolts (see Eq. 2.35). This is 2 to 3 orders of magnitude below the values measured for artificially prepared grain boundaries in $YBa_2Cu_3O_{7-x}$ films [70]. According to Halbritter the large slopes of $R_s(H_{rf})$ can also be explained by assuming localized states in the tunneling barrier, which might create a region with a reduced order parameter in the vicinity of the grain boundary [173]. In this case it becomes likely that pair breaking is enhanced. However, it is presently impossible to quantify this effect.

At higher power levels R_s exhibits an H_{rf} dependence stronger than quadratic and a frequency dependence changing from quadratic to linear (Fig. 4.17). According to Sridhar et al. the entire $R_s(H_{rf}, T)$ can be fitted within a model based on an rf-current induced critical state [76, 174]. However, this model implies that the lower critical magnetic field H_{c1} is equal to zero, i.e. magnetic flux can penetrate at the lowest levels of H_{rf}. Moreover, the critical state model leads to a linear frequency dependence of $R_s(H_{rf}) - R_s(0)$ down to the lowest H_{rf} values, which is in contradiction to the quadratic dependences reported in [71]. In a more recent work, Nguyen combined the critical state model with the weak-coupling grain model in order to fit the entire $R_s(H_{rf}, T, f)$ dependences [175]. However, the question about

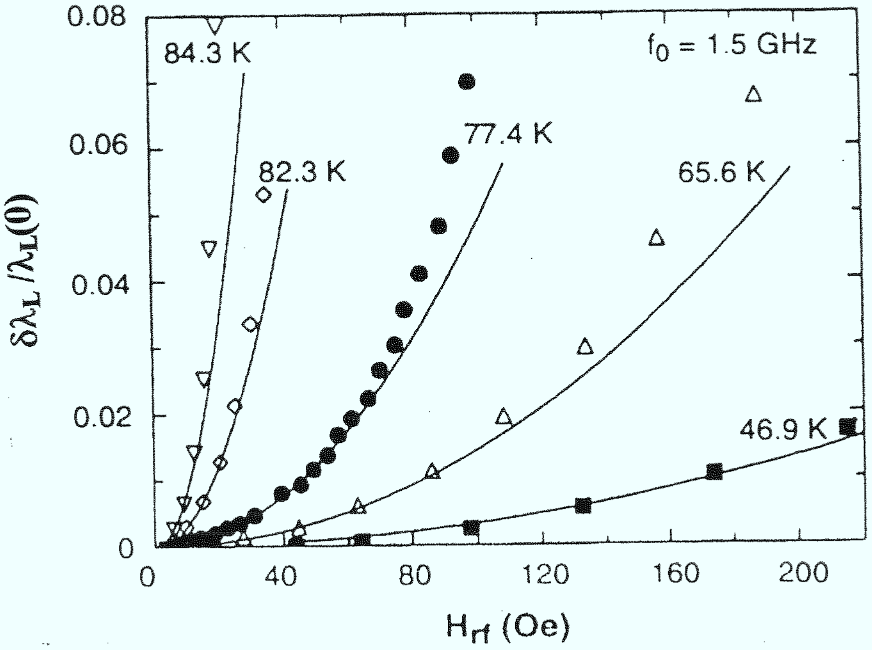

Fig. 4.18: Relative change of penetration depth with rf magnetic peak field at 1.5 GHz and different temperatures, measured with a stripline resonator fabricated from an $YBa_2Cu_3O_{7-x}$ film prepared by off-axis magnetron sputtering (from [71]).

the origin of the weak links with low I_cR values still remains unanswered.

All measurements discussed below were performed with stripline resonators, where the rf field is strongly peaked within a distance of about the penetration depth from the film edge. Here the material could be degraded due to oxygen deficiency or other damage originating from the patterning procedure. Hence resonator geometries with the maximum rf field sufficiently far away from the edges might give different results.

Fig. 4.19 from [156] shows $R_s(H_{rf})$ at about 5 GHz measured by a sapphire dielectric resonator for two $YBa_2Cu_3O_{7-x}$ films of two inches in diameter prepared by off-axis magnetron sputtering. Up to field levels of about 10 Oe R_s does not show a significant field dependence. Using a similar technique at 20 GHz, $R_s(H_{rf})$ of an $YBa_2Cu_3O_{7-x}$ film prepared by high-oxygen-pressure sputtering was measured up to field levels of 250 Oe indicating a weak linear $R_s(H_{rf})$ dependence (Fig. 4.20 from [114]), in strong contrast to the data in Fig. 4.17. Assuming an f^2 frequency dependence, R_s exhibits a much weaker dependence on H_{rf} in comparison to the stripline results. The slope measured at 4.2 K, however, is of the same order as the slight increase of R_s apparent in the 20 K data in Fig. 4.19 (using f^2 scaling). It is worthwhile to compare this slope to Eq. 2.39 in section 2.2.1, which is an estimate for the effect of pair breaking for a d-wave superconductor. Using λ_L=150 nm, and a thermodynamic critical field H_c with $\mu_0 H_c = 3$ T, the observed slope is consistent with a quasiparticle scattering rate τ_q^{-1} of $7 \cdot 10^{10}$ s^{-1}. This value corresponds to an $R_s(T)$ behavior with a pronounced plateau (see Fig. 4.6a in Section 4.1), which is typical for films prepared by high-

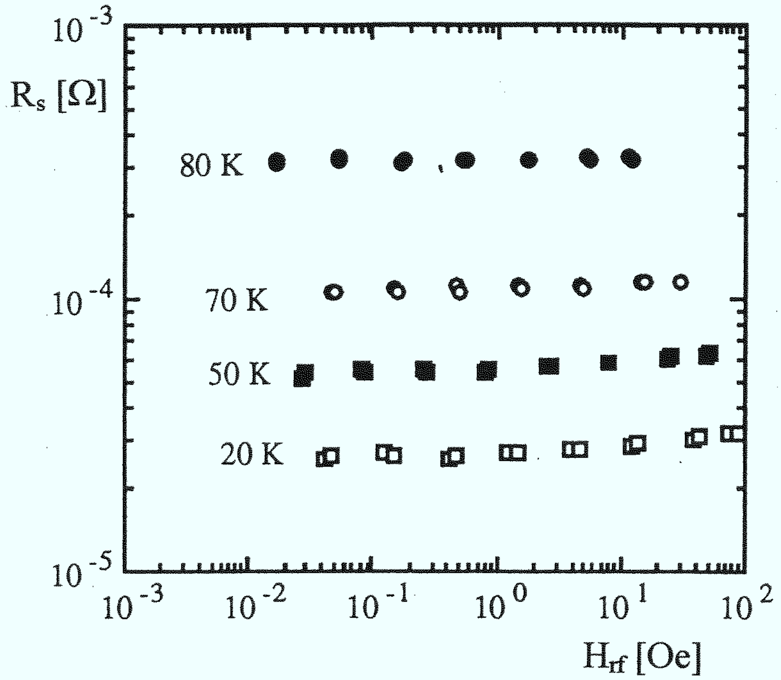

Fig. 4.19: Surface resistance versus H_{rf} at about 5 GHz at different temperatures, measured with a dielectric sapphire resonator for a pair of $YBa_2Cu_3O_{7-x}$ films of two inches in diameter prepared by off-axis magnetron sputtering (from [156]).

oxygen-pressure dc sputtering. According to Eq. 2.43, one also expects a linear slope for $\delta\lambda_L(H_{rf})/\lambda_L(0)$ of about $8 \cdot 10^{-5}$ /mT. This slope is slightly weaker than the experimental results presented in Fig. 4.18.

Meanwhile, weak $R_s(H_{rf})$ dependences like that in Fig. 4.20 were measured for many large-area films prepared by different growing techniques [120, 121, 116]. As shown recently by Zuccaro and Klein [116], $R_s(H_{rf})$ is strongly sample dependent for films prepared under the same conditions, in strong contrast to highly reproducible $R_s(T)$ curves at low levels of rf power. This indicates that inhomogeneity of the films can limit the high-field behavior. Recently, Hampel et al. presented results using a thermal imaging method to detect "hot spots" on an HTS microwave filter during operation a high rf power [117]. The results indicate that local defects, possibly originating from scratches in the substrate surface, are responsible for the field breakdown in the device. Such defects are most likely formed by regions with degraded critical current density. Hein et al. recently calculated the effect of global and local heating due to the rf power by solving the stationary heat equation for an HTS film on a substrate, which is connected with its backside to a heat sink [119]. The results of these numerical calculations are in qualitative agreement with the $R_s(H_{rf})$ curves shown in Fig. 4.20.

Most of the experimental data on the dependence of the surface impedance on dc magnetic fields are taken at magnetic induction levels of the order of tesla. As discussed in the next section, this provides information about the vortex dynamics.

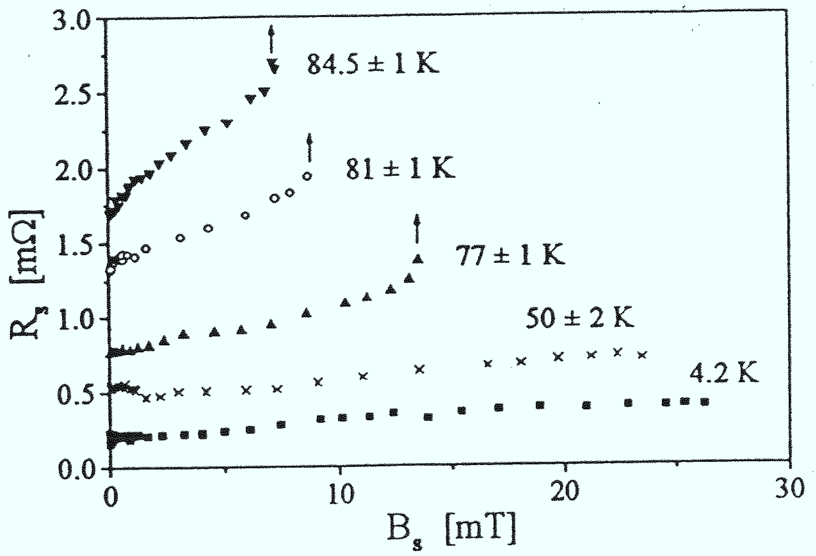

Fig. 4.20: Surface resistance versus rf magnetic field ($H_{rf} = B_s/\mu_0$) at 20 GHz at different temperatures, measured with a dielectric sapphire resonator for an $YBa_2Cu_3O_{7-x}$ film one inch in diameter prepared by high-oxygen-pressure dc sputtering (from [114]).

4.6 Surface impedance in the Shubnikov phase

The field dependence of the surface impedance for static magnetic fields above $\mu_0 H_{c1} \approx 100\,\mathrm{mT}$ is determined by the dynamics of the vortices. Weak link effects and pair breaking effects (see Section 2.2.1) are assumed to be negligible.

Fig. 4.21 from [176] shows δR_s and $\delta X_s(H)$ at different temperatures at 5.4 GHz in an ambient dc magnetic field oriented perpendicular to the surface of a c-axis oriented $YBa_2Cu_3O_{7-x}$ film prepared by high-oxygen-pressure sputtering. This measurement was performed using a parallel plate resonator (see Subsection 3.1.4). Both δR_s and δX_s exhibit an almost linear dependence on H as expected from Eq. 2.49. The small temperature variation of δX_s indicates that the Labusch parameter α_p has a small temperature variation. Fig. 4.22 from [99] shows a selection of experimental results for α_p determined from several experiments on $YBa_2Cu_3O_{7-x}$ and $Bi_2Sr_2CaCu_2O_8$. The general trend is that α_p has a much stronger temperature dependence than expected from the conventional theory of pinning (solid line, see [99, 177] and references therein). The dashed lines were calculated assuming an $\exp(-T_0/T)$ temperature dependence of the pinning potential employing $\alpha_p = d^2U/d^2x$ with T_0=28 K for $YBa_2Cu_3O_{7-x}$ (upper dashed line) and T_0=9 K for $Bi_2Sr_2CaCu_2O_8$ (straight dashed line). Such a smearing of the pinning potential is expected to be a result of thermal fluctuations, which should be more pronounced for $Bi_2Sr_2CaCu_2O_8$ due to the enhanced anisotropy. Interestingly, the results from Ghosh et al. [179] on $YBa_2Cu_3O_{7-x}$ films prepared by high-oxygen-pressure sputtering for magnetic fields parallel to the ab-plane are consistent with a nearly temperature independent α_p as

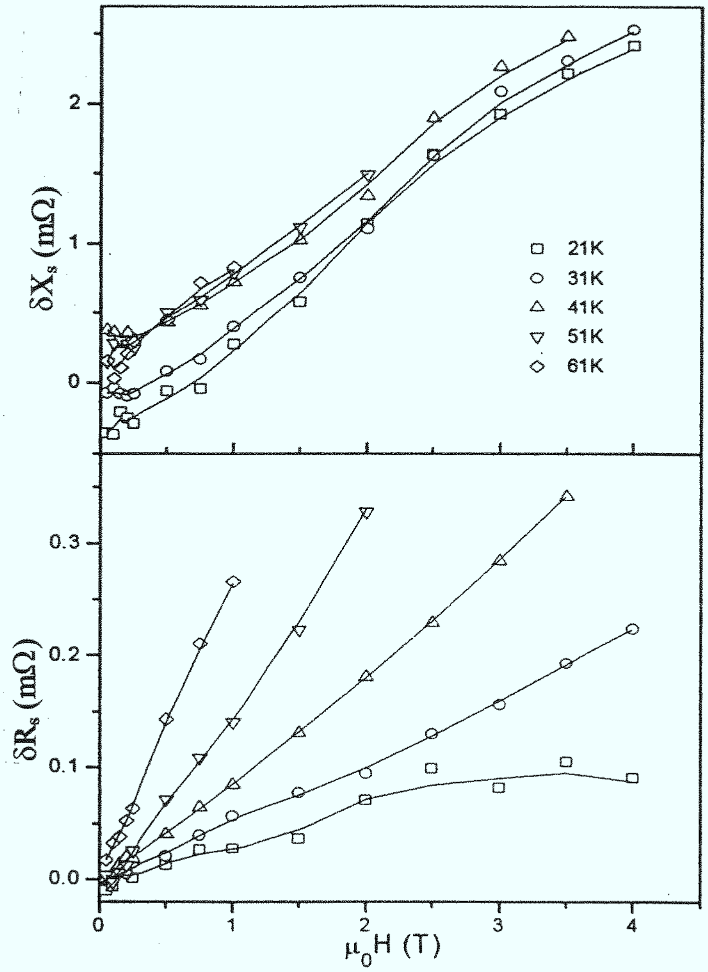

Fig. 4.21: $\delta R_s(H) = R_s(H) - R_s(H = 0)$ and $\delta X_s(H) = X_s(H) - X_s(H = 0)$ at different temperatures at 5.4 GHz in an ambient dc magnetic field H oriented perpendicular to the surface of a c-axis oriented $YBa_2Cu_3O_{7-x}$ film prepared by high-oxygen-pressure sputtering (from [176]).

high as 2 to 4 $\cdot 10^5$ N/m^2. This may be explained by intrinsic in-plane pinning of vortices.

For the determination of vortex viscosity η both R_s and X_s data need to be analyzed (see Eq. 2.49). The strong temperature dependence of $\delta R_s(H)$ in Fig. 4.21 reflects the strong temperature dependence of the vortex viscosity η. Data of $\eta(T)$ from different experiments are summarized in Fig. 4.23 from [99]. The solid line in Fig. 4.23 was calculated according to the Bardeen-Stephen formula

$$\eta = \mu_0 \Phi_0 \rho H_{c2}(T) = \mu_0 \Phi_0 \rho H_{c2}(0) \frac{1 - (T/T_c)^2}{1 + (T/T_c)^2} = \pi n h \omega_c(T) \tau(T) \qquad (4.2)$$

with $\Phi_0 = h/2e = 2.07 \cdot 10^{-15}$ Vs being the elementary flux quantum and ρ the normal-state resistivity. Using $\mu_0 H_{c2}(0)$=100 T, the solid line in Fig. 4.23 corre-

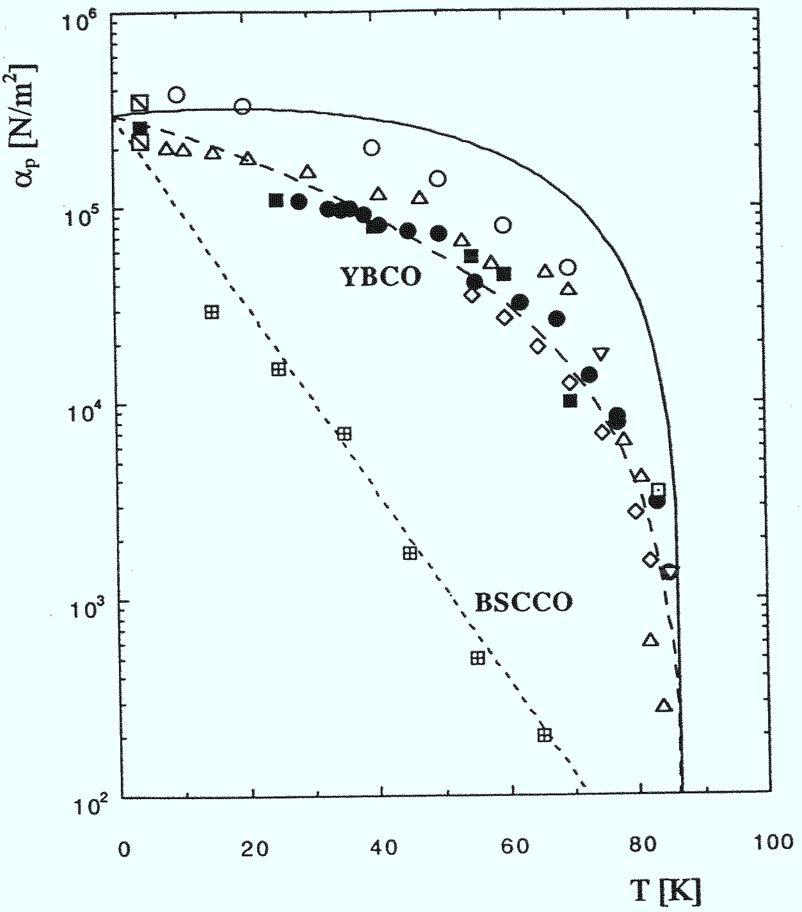

Fig. 4.22: Temperature dependence of Labusch parameter α_p. The solid line represents the approximation $\alpha_p(\tilde{t} = T/T_c) = \alpha(0)(1 - \tilde{t}^{4/3})(1 + \tilde{t}^2)$ by Blatter et al. [177], the dashed lines correspond to $\alpha_p(\tilde{t}) = \alpha(0)(1 - \tilde{t}^{4/3})(1 + \tilde{t}^2)\exp(-T/T_0)$ with $T_0 = 28$ K for $YBa_2Cu_3O_{7-x}$ and $T_0 = 9$ K for $Bi_2Sr_2CaCu_2O_8$ (from [99]).

sponds to $\rho = 17\,\mu\Omega cm$. This is smaller than $\rho(100K) = 50 - 100\,\mu\Omega$cm of $YBa_2Cu_3O_{7-x}$, as expected from the decrease of the quasiparticle scattering rate below T_c (see Section 4.2). The strong scattering of the η data in Fig. 4.23 may be an indication for the different τ_{res}-values of the different samples (see section 4.1).

According to Eq. 4.2 η can also be expressed as a function of charge carrier density n, quasiparticle scattering time τ and cyclotron frequency at H_{c2}, $\omega_c = e\mu_0 H_{c2}/m^*$. The Bardeen-Stephen expression relies on a hydrodynamic approach, i.e. $\omega_c\tau << 1$. In contrast, the region $\omega_c\tau > 1$ is equivalent to the so-called superclean limit: The quasiparticles in the vortex core occupy discrete energy levels with typical level spacing of the order of $\delta E = \Delta^2/\epsilon_F = \hbar\omega_c$. In the superclean limit there is no mixing between these levels due to scattering, i.e. $\delta E > \hbar/\tau$. Therefore η values above the dashed line in Fig. 4.23 correspond to the superclean limit, where the applicability of the Bardeen-Stephen expression is questionable. In summary, the vortex viscosity of

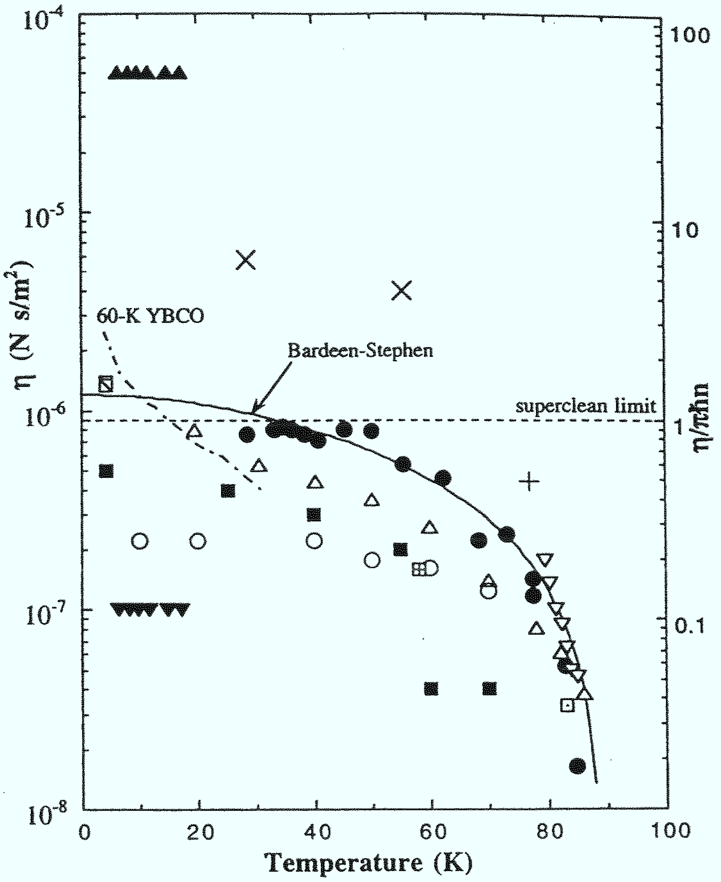

Fig. 4.23: Temperature dependence of the vortex viscosity η of $YBa_2Cu_3O_{7-x}$. Open and solid symbols represent data with H parallel to the c-axis, crosses represent data with H perpendicular to the c-axis. The solid line was calculated from the Bardeen-Stephen formula, the "superclean limit" is explained in the text (from [99]).

the cuprates is not yet understood theoretically, further complications are expected due to the anisotropy of the order parameter.

The temperature and frequency dependence of the surface impedance in an ambient magnetic field oriented perpendicular to the surface (i.e. parallel to the c-axis) was recently measured by Belk et al. [178] using a stripline resonator (Fig. 3.5b). Fig. 4.24 from this reference shows $R_s(T, f)$ for an applied magnetic flux density of two tesla. Interestingly, the analysis of the data indicates a $f^{1.2}$ to $f^{1.4}$ frequency dependence of $\delta R_s = R_s(H) - R_s(H = 0)$ below T=65 K. This is in contradiction to the Coffey and Clem model (see Section 2.2.4), which provides a combination of an f^2-dependent (see Eq. 2.49) plus a frequency-independent part of δR_s [98], the latter being a consequence of flux creep. Assuming a distribution of pinning energies, it was possible to explain the observed frequency dependences within an extension of the Coffey and Clem model [178].

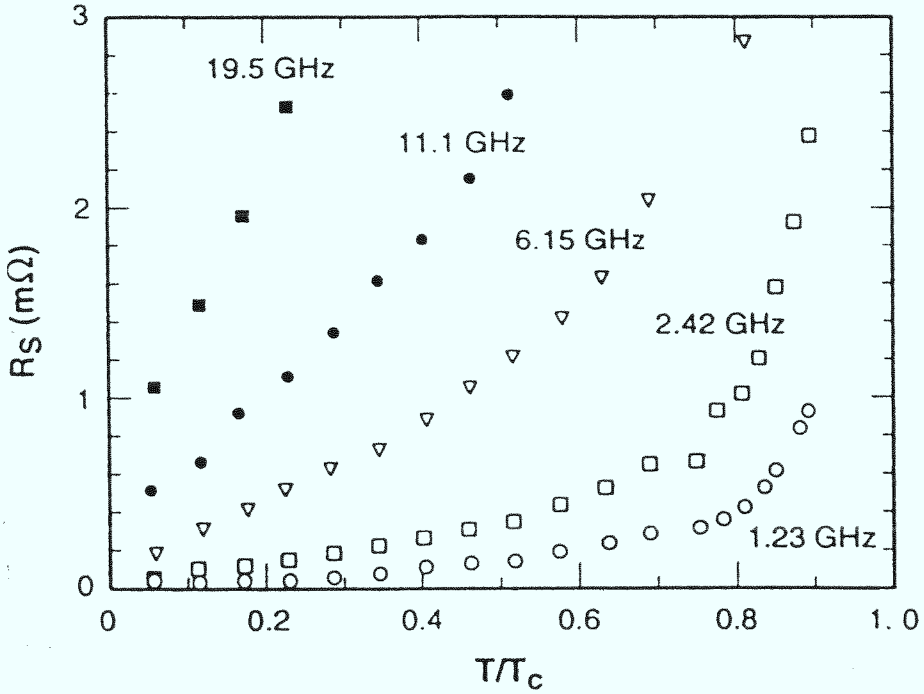

Fig. 4.24: Temperature dependence of the surface resistance at different frequencies in a magnetic flux density of two tesla applied parallel to the surface (from [178]).

4.7 Bi-Sr-Ca-Cu-O compounds

The most important representatives of the Bi-Sr-Ca-Cu-O compounds are $Bi_2Sr_2CaCu_2O_8$ (T_c = 90 K) and $Bi_2Sr_2Ca_2Cu_3O_{10}$ (T_c = 105 K). The $Bi_2Sr_2CaCu_2O_8$ phase can be grown as thin films and bulk single crystals as well [180]. However, in spite of sample quality being comparable to $YBa_2Cu_3O_{7-x}$ the surface resistance is about one order of magnitude larger in comparison to thin films of $YBa_2Cu_3O_{7-x}$ and the Tl-Ba-Ca-Cu-O compounds [133]. The penetration depth depends strongly on the level of oxygen doping, the achieved values for $\lambda_{L,a,b}(T \to 0)$ range from 260 nm [181] to 450 nm [133, 182]. The *ab* vs *c* anisotropy is much larger than for $YBa_2Cu_3O_{7-x}$, which gives rise to intrinsic Josephson coupling between adjacent CuO_2 layers [50]. The *d*-wave models, which are two-dimensional, should be more appropriate for the Bi-Sr-Ca-Cu-O compounds than for $YBa_2Cu_3O_{7-x}$.

The temperature dependence of λ_L of thin films was found to be T^2 at $T << T_c$ [161, 183], similar to $YBa_2Cu_3O_{7-x}$ films with high defect density (see Section 4.3). Recently, a linear dependence of λ_L and R_s was measured for bulk single crystals of $Bi_2Sr_2CaCu_2O_8$ [184]. Here the absence of a plateau in $R_s(T)$ indicates a high value of the residual scattering rate, which is in contradiction to the observed linear dependences according to the *d*-wave model (see Fig. 2.7 and 2.8). Similar to $YBa_2Cu_3O_{7-x}$, for $Bi_2Sr_2CaCu_2O_8$ thin films the temperature dependence of the conductivity σ_1 (Fig. 4.25) and the penetration depth (Fig. 4.26) was found to be

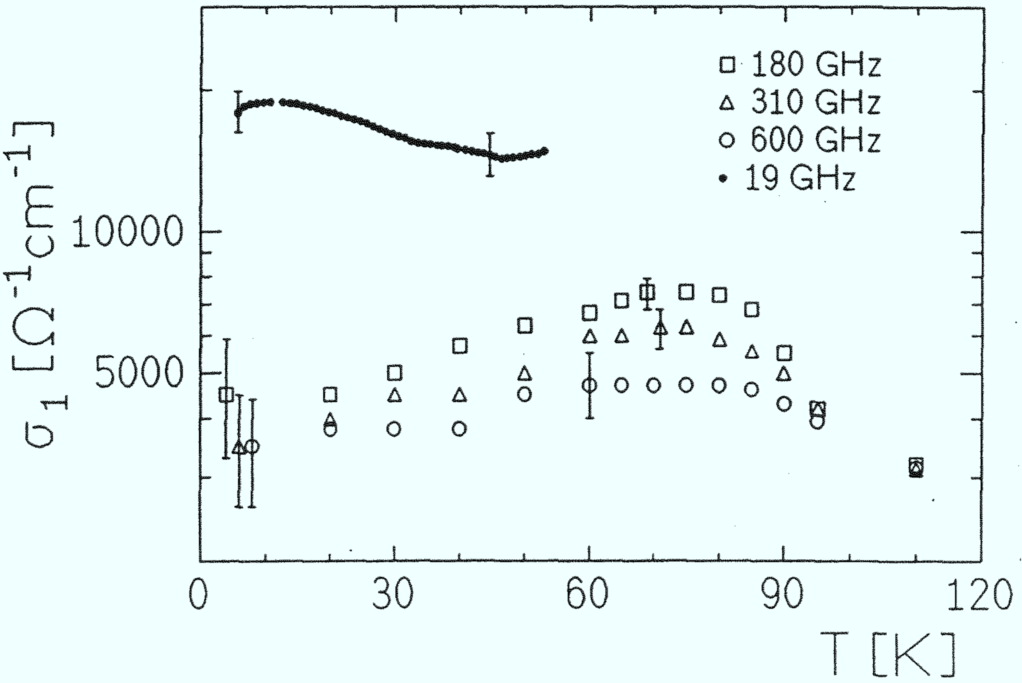

Fig. 4.25: Temperature dependence of the conductivity σ_1 for a $Bi_2Sr_2CaCu_2O_8$ film prepared by pulsed laser deposition (from [133]).

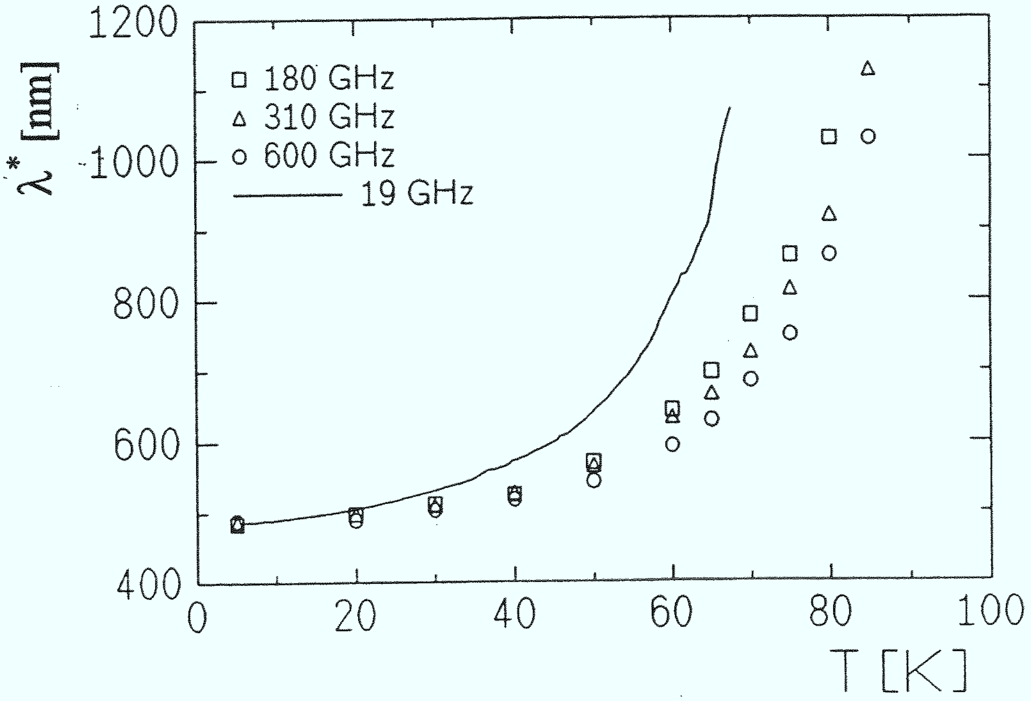

Fig. 4.26: Temperature dependence of the penetration depth $\lambda^* = 1/\sqrt{\omega\mu_0\sigma_2}$ for a $Bi_2Sr_2CaCu_2O_8$ film prepared by pulsed laser deposition (from [133]).

determined by a strong temperature dependence of the quasiparticle scattering rate below T_c (Fig. 4.27). According to this analysis within the modified two-fluid model from Bonn et al. (Eq. 2.33 and 2.34, Section 2.2.1) the reason for the high R_s values of $Bi_2Sr_2CaCu_2O_8$ in comparison to $YBa_2Cu_3O_{7-x}$ is the large value of the penetration depth (Fig. 4.27). Therefore, the Bi-Sr-Ca-Cu-O compounds are not considered to be of any relevance for microwave applications (except active devices based on the intrinsic Josephson effect).

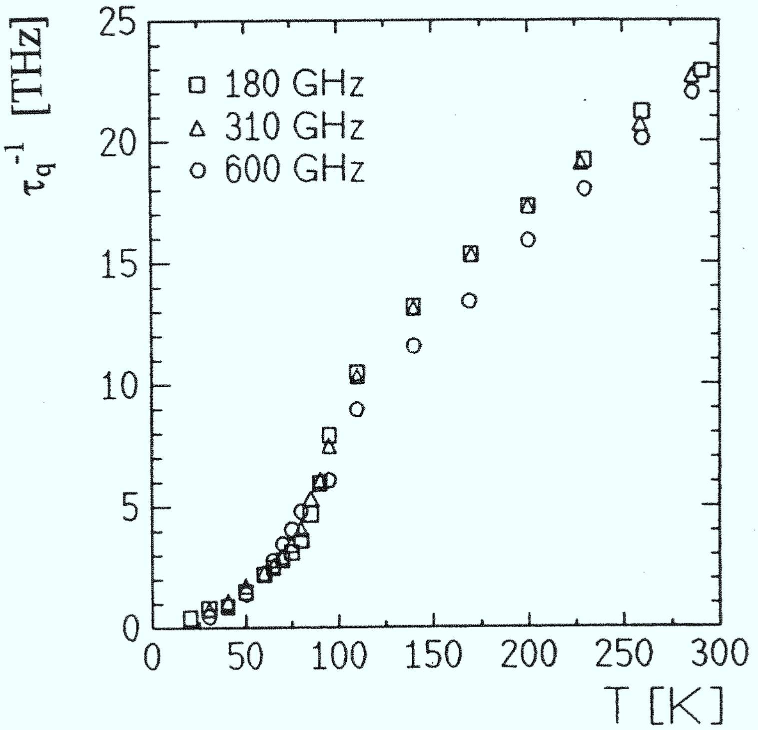

Fig. 4.27: Temperature dependence of the quasiparticle scattering rate τ_q^{-1} for a $Bi_2Sr_2CaCu_2O_8$ film prepared by pulsed laser deposition (from [133]).

4.8 Tl-Ba-Ca-Cu-O compounds

The Tl-Ba-Ca-Cu-O compounds are a very challenging alternative to $YBa_2Cu_3O_{7-x}$ since high-quality films providing a level of microwave losses as low as for $YBa_2Cu_3O_{7-x}$ can be grown. On the other hand the critical temperatures are higher, and therefore the R_s(77 K) values are lower. Crystal structure, physical properties, and synthesis are reviewed in [187]. Here only recent results on the microwave properties will be discussed.

So far, films with very low R_s values have been made from $Tl_2Ba_2CaCu_2O_8$ (T_c up to 105 K, $Tl_{0.5}Pb_{0.5}Sr_2Ca_2Cu_3O_9$ (T_c up to 118 K, [188]), and $Tl_2Ba_2Ca_2Cu_3O_{10}$ (T_c up to 110 K, [185]). Because of the low vapor pressure of thallium the films are prepared in a two-step process, starting with the growth of an amorphous thallium-free precursor film. As second step, crystallization takes place upon annealing the precursor film in a sealed container with thallium vapor. Epitaxial films with some low-angle grain boundaries are obtained due to the presence of a liquid phase, resulting in grain size of up to 100 μm. Fig. 4.28 from [185] shows the surface resistance at 87 GHz for several $Tl_2Ba_2Ca_2Cu_3O_{10}$ films with the annealing procedure performed at 1168 K (A and B), 1165 K (C), and 1161 K (D). It is obvious that $R_s(T)$ (and dc resistivity and penetration depth as well) depend strongly on the grain structure, which is extremely sensitive to the post-annealing procedure. The advantage of $Tl_2Ba_2Ca_2Cu_3O_{10}$ with respect to $YBa_2Cu_3O_{7-x}$ is the higher T_c, leading to

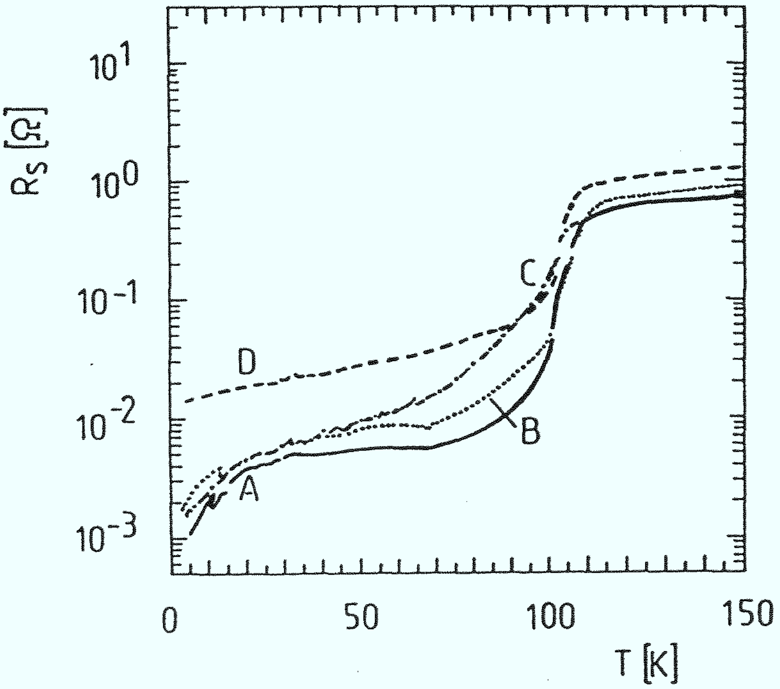

Fig. 4.28: Measured $R_s(T)$ at 87 GHz for several $Tl_2Ba_2Ca_2Cu_3O_{10}$ films which were post annealed in thallium vapor at 1168 K (A and B), 1165 K (C), and 1161 K (D) (from [185]).

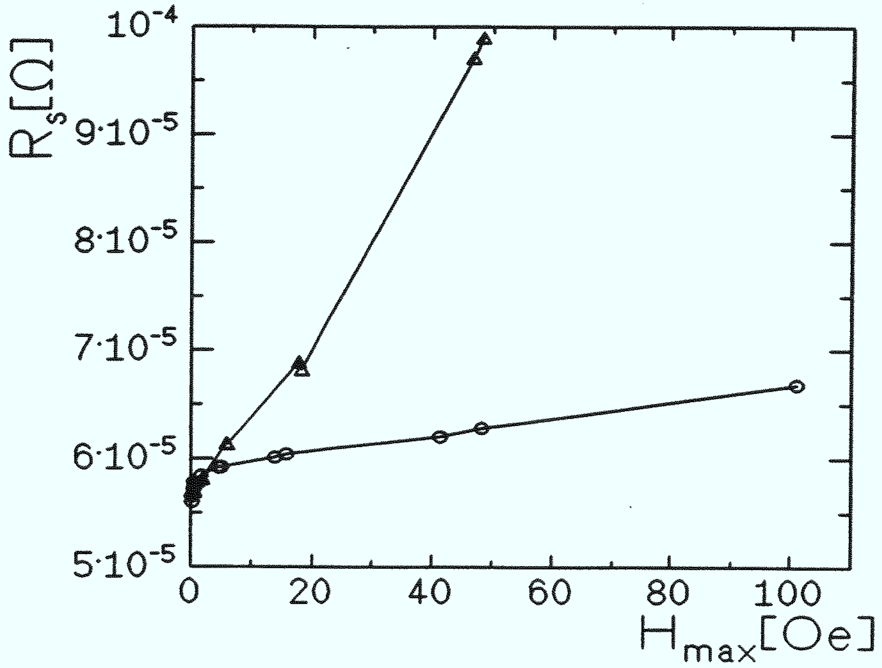

Fig. 4.29: Surface resistance versus maximum rf-magnetic field H_{max} for an $YBa_2Cu_3O_{7-x}$ film (circles) in comparison to a $Tl_2Ba_2CaCu_2O_8$ film (triangles) at 5.5 GHz and 70 K, measured by a dielectric resonator technique (from [186]).

R_s values at 77 K up to two times smaller in comparison to $YBa_2Cu_3O_{7-x}$ (curve A). Fig. 4.29 from [186] shows $R_s(H_{rf})$ for $YBa_2Cu_3O_{7-x}$ in comparison to $Tl_2Ba_2CaCu_2O_8$ at 5.5 GHz and 70 K. Obviously, the thallium films have a stronger $R_s(H_{rf})$ dependence in comparison to $YBa_2Cu_3O_{7-x}$, which is assumed to result from a higher level of granularity.

In summary, thin films of the Tl-Ba-Ca-Cu-O compounds provide an interesting alternative to $YBa_2Cu_3O_{7-x}$, in particular for operation at 77 K and above. The further improvement of epitaxy should be accompanied by a further reduction of the power dependence of R_s. Furthermore, ony may hope that similar properties will be achievable in the future with the mercury compounds [42, 43]. Recent results (not R_s) on thin films of these compounds are quite promising [189].

4.9 *n*-type cuprates

The *n*-type (=electron doped) cuprate $Nd_{1.85}Ce_{0.15}CuO_{4-y}$ can be prepared as epitaxial thin film with high quality. For the best films (prepared by pulsed laser deposition on yttria-stabilized zirconia buffered substrates) R_s at $T \rightarrow 0$ of 80 $\mu\Omega$ was achieved at a frequency of 9.6 GHz [190], which is comparable to that of thin films of $YBa_2Cu_3O_{7-x}$. Fig. 4.30 from [190] shows the measured temperature dependence of R_s for two different samples. The solid lines represent the best fits to the data using $R_s(T) = C/T \exp(-\Delta/kT) + R_{res}$, with $2\Delta/kT_c = 4.1$. This is in good agreement with values determined from the temperature dependence of the magnetic field penetration depth [191, 192, 193].

The observation of such a thermal activated behavior is a clear indication of *s*-wave superconductivity with a pronounced gap in the density of states. The experimental value of $2\Delta/kT_c$ is larger than the weak-coupling BCS value indicating strong coupling. Interestingly, the temperature dependence of the dc resistivity above T_c is quadratic rather than linear as for *p*-type cuprates like $YBa_2Cu_3O_{7-x}$. The observed quadratic dependence is more similar to conventional metals, indicating that electron-phonon interaction is the dominant inelastic scattering machanism. According to photoemission data there is no nesting of the Fermi surfaces for the *n*-type cuprates [194]. Therefore, only for *p*-type cuptrates electron-electron interaction is dominant, which may lead to the high critical temperatures. In the *n*-type cuprates, however, superconductivity may be conventional, i.e. by strong electron-phonon interaction. Unfortunately, so far the observed critical temperatures of the *n*-type cuprates are quite low.

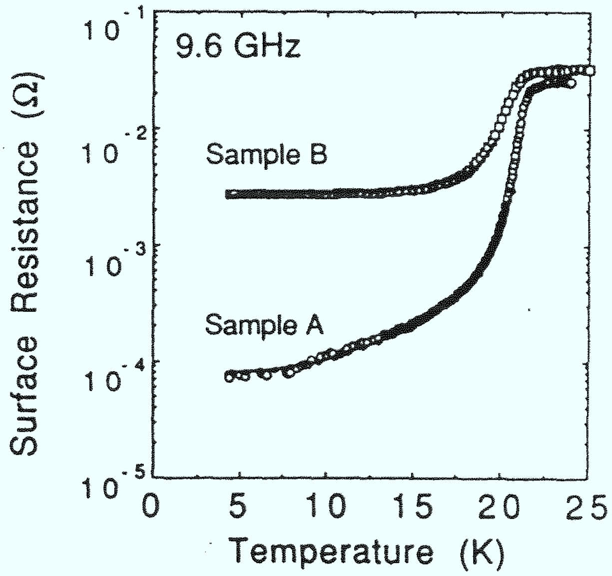

Fig. 4.30: $R_s(T)$ at 9.6 GHz for two different thin films of $Nd_{1.85}Ce_{0.15}CuO_{4-y}$ (from [190]).

Chapter 5

Conclusions

The electrodynamic properties of oxide high temperature superconductors have been studied extensively since their discovery by Bednorz and Müller in 1986. After the successful preparation of epitaxial thin films in 1988 the microwave losses were found to be very low, initiating ongoing work on high temperature superconductor based microwave devices. In turn, these efforts in device work initiated systematic studies of the microwave properties of the different superconducting compounds, the optimization of film growth techniques with respect to low microwave losses, and theoretical modeling in order to understand the physics of microwave absorption.

Many features of the linear microwave properties, i.e. the temperature and frequency dependence of the surface impedance, are now understood. The temperature and frequency dependence of the surface resistance is determined by a strong decrease of the quasiparticle scattering rate below the critical temperature, and not by density of state effects as in many conventional superconductors. This gives rise to a plateau in the temperature dependence of the surface resistance, which becomes more pronounced for high-purity samples with low values of the impurity scattering rate. Thus – to some extent – defects help to reduce the surface resitance in the temperature range of technical applicability between 30 and 70 K. On the other hand, for $YBa_2Cu_3O_{7-x}$ oxygen vacancies in the copper oxygen chains give rise to a strong enhancement of the surface resistance and the penetration depth as well.

One possible explanation for the strong temperature decrease of the quasiparticle scattering rate is that spin fluctuations rather than phonons provide the dominant contribution to the inelastic scattering rate. This is an indication for a purely electronic mechanism being responsible for superconductivity in the high temperature superconducting cuprates. According to recent theories there is strong evidence that spin fluctuation scattering gives rise to superconductivity with high values of the critical temperature. One peculiarity of this new type of superconductivity is a d-wave order parameter. For a d-wave order parameter the high residual microwave losses observed in the HTS cuprates could be partially intrinsic in origin, explicitly due to a finite density of states at the Fermi energy even at $T \to 0$. On the other hand, there are other possible explanations for extrinsic residual losses. In

$YBa_2Cu_3O_{7-x}$, for example, the copper oxygen chains form an intrinsically normal-conducting subsystem, which becomes weakly superconducting by charge transfer due to the internal proximity effect. This induced superconducting state in the one-dimensional copper-oxygen chains is extremely sensitive to oxygen deficiency and disorder, i.e. the induced superconducting state easily becomes gapless.

Finally, in materials with more complex crystal structure as in the Tl-Ba-Ca-Cu-O compounds, there is still some residual granularity in high-quality films. Weak links formed by grain boundaries are a possible source of residual losses. On the other hand, weak links generate a quadratic high frequency magnetic field dependence of the surface resistance at field levels of several orders of magnitude below the intrinsic lower critical field H_{c1}. Such an increase was indeed observed for $YBa_2Cu_3O_{7-x}$ stripline resonators. Recent measurements of the power dependence of high-quality $YBa_2Cu_3O_{7-x}$ films exhibit a very weak linear dependence, indicating that granularity is not the dominant loss contribution. On the other hand, in the case of a d-wave or a strongly anisotropic s-wave order parameter velocity-induced pair breaking gives rise to an intrinsic increase of the surface impedance with magnetic field. This still needs to be worked out theoretically in more detail, and more experiments in the field range below H_{c1} for dc and rf fields are required as well.

Presently, a lot of work is being performed on the surface impedance in the mixed state. This has already thrown some light onto the vortex dynamics, but a complete understanding has not yet been achieved. So far, one can conclude that individual pinning can describe the observed dependence (not too close to T_c), but the temperature dependence of the vortex viscosity as determined from the Coffey and Clem model are still not understood. Careful analysis of frequency, field and temperature dependences, measurements of anisotropies and theoretical modeling beyond Coffey and Clem should lead to further progress.

Without any doubt, there now is a large potential for application of HTS films in microwave technology. Now the most important task for scientists working on microwave properties and applications of HTS is to talk to the microwave system engineers and try to figure out where superconducting devices can solve some of their problems. A market for HTS microwave devices will be essential to justify further fundamental work. Parallel efforts on material improvement, physical modeling and understanding, device design, and system engineering will be essential to utilize the large potential of high-temperature-superconductors in microwave technology.

Acknowledgments

At first, I would like to thank my coworkers and collegues at Forschungszentrum Jülich, Dr. U. Dähne, Dr. Yu. Divin, Dr. M. Faley, Dr. I. Ghosh, Dr. B. Kabius, Dr. U. Poppe, Dipl. Phys. A. Scholen, Dr. M. Seo, Dr. J. Schubert, Dipl. Phys. H. Schulz, Dr. H. Soltner, Dipl. Phys. N. Tellmann, Dr. R. Wördenweber, Dr. A. Zaitsev, and Dipl. Phys. C. Zuccaro, for their commitment in performing experimental work togehter with me. Their continuous efforts are the basis for this review article. I would like to express my sincere thanks to the head of our institute, Prof. Dr. K. Urban, who has strongly supported the activities of my group and who gave many useful advices which helped to improve the manuscript. In addition, the support of the former and present head of the Institut für Schicht- und Ionentechnik, Prof. Dr. C. Heiden and Prof. Dr. A.I. Braginski, was essential for pointing the work into the right direction. Technical support from Dipl. Ing. W. Evers, K. Hirtz, W. Reinboth and G. Wassenhoven is gratefully acknowledged, as it was essential for successful experimental work.

Our own work in the field covered by this review article has gained important input from many national and international collaborations. Therefore, for valuable discussions before and during my work on this review article I would like to express my thanks to Prof. Dr. H. Chaloupka, Dipl. Phys. W. Diete, Dr. M. Hein, Dipl. Phys. S. Hensen, Dipl. Phys. M. Jeck, Dr. S. Kolesov, Dipl. Phys. M. Lenkens, Dr. habil. G. Müller, Dr. S. Orbach-Werbig, Prof. Dr. H. Piel, Dr. T. Patzelt, Dr. A. Pischke, Dipl. Phys. H. Schlick, Dipl. Phys. D. Wehler (Bergische Universität Wuppertal), Dr. J. Geerk, Dr. J. Halbritter (Forschungszentrum Karlsruhe), Prof. Dr. H. Kinder, Dr. W. Prusseit (Technische Universität München), Dr. C.T. Rieck, Prof. Dr. K. Scharnberg (Universität Hamburg), Prof. Dr. W. Weber (Universität Dortmund), Prof. Dr. R. Hübener (Universität Tübingen), Prof Dr. G. Güntherodt (Technische Universität Aachen), Prof. Dr. H. Saemann-Ischenko (Universität Erlangen), Prof. Dr. K. Renk (Universität Regensburg), Dr. R. Fischer, and Dipl. Ing. H. Kratz (Daimler Benz AG). Among the friends and collegues outside Germany, I like to thank Dr. S. A. Wolf (Naval Research Laboratory, USA), Dr. V. Z. Kresin (Lawrence Berkeley Laboratory), Dr. D.E. Oates (MIT Lincoln Laboratory, USA), Dr. J. Wosik (University of Houston, USA), Prof. Dr. S. Anlage (University of Maryland, USA), Prof. Dr. S. Sridhar (Northeastern University, USA), Dr. D.W. Face (DuPont, USA), Dr. H. Asano (NTT, Japan), Dr. Y. Goncharov, Prof. Dr. G. Kozlov (Academy of Sciences, Moscow, Russia), Prof. Dr. O. Vendik (Ioffe Institute, St. Petersburg, Russia), Dr.

R. Humphreys (DRA Malvern, UK), Prof. Dr. C. Gough, Dr. A. Porch, Dr. B. Avenhaus (University of Birmingham, UK), Prof. Dr. N.Mc.N. Alford (Southbank University, UK), Dr. A. Andreone (University of Naples, Italy), Dr. J. Dumas, Prof. Dr. C. Schlenker (CNRS Grenoble, France), and Dr. J.C. Mage (Thomson CSF, France) for valuable discussions on the subject of this review article.

Our own work discussed in this review article was funded in part by the German "Bundesminsterium für Bildung, Wissenschaft, Forschung und Technologie" (BMBF) within the consortia "First applications of high-temperature superconductors in micro- and cryoelectronics" and "HOTRONIK", and by the European Community within the ESPRIT project "SUPERMICA" and the Brite-Euram project "DiHiMiCo".

List of Symbols

Symbol	**Description**	**Units**
a	average grain size	m
α_p	Labusch parameter (=pinning force constant)	N/m
$\vec{B}$, $\vec{B}^*$	magnetic flux density vector, complex conjugated	T, G (1 G = 10^{-4} T)
β	propagation constant of an electromagnetic wave	m^{-1}
c	velocity of light in vaccum	$2.9979 \cdot 10^9$ m/s
$D(\epsilon)$	density of states at energy ϵ	
$\vec{D}$, $\vec{D}^*$	displacement current vector, complex conjugated	$\mathrm{A/m^2s}$
Δ	energy gap of a superconductor	eV
$\vec{E}$, $\vec{E}^*$	electric field vector, complex conjugated	V/m
$\epsilon = E - E_F$	difference between quasiparticle energy E and Fermi energy E_F	eV
ϵ_0	electrical permeability of vacuum	$8.854 \cdot 10^{-12}$ As/Vm
$\epsilon_r = \epsilon_{r,1} + i\epsilon_{r,2}$	complex relative electrical permittivity	
$\vec{e_x}, \vec{e_y}, \vec{e_z}$	unit vectors of a cartesian coordinate system (x,y,z): $\vec{e_x} = (1,0,0), \vec{e_y} = (0,1,0), \vec{e_z} = (0,0,1)$	
η	vortex viscosity	Ns/m
f	frequency	Hz (1 Hz = 1 s^{-1})
F	Fermi function	
G	geometric factor	Ω
$\Gamma = \hbar\tau^{-1}$	energy corresponding to momentum transfer by a scattering process with scattering rate τ^{-1}	eV
$\vec{H}$, $\vec{H}^*$	magnetic field vector, complex conjugated	A/m, Oe (1 Oe = $1.257 \cdot 10^{-3}$ A/m
H_{rf}	amplitude of high-frequency (rf) magnetic field	A/m, Oe
H_c	critical magnetic field	A/m, Oe
H_{c1}, H_{c2}	lower/upper critical field of a type-II superconductor	A/m, Oe
h	Plancks's constant	$6.626 \cdot 10^{-34}$ Js
$\hbar$	$h/2\pi$	$1.055 \cdot 10^{-34}$ Js
i	imaginary unit, $i^2 = -1$	
I	electrical current	A
I_c	critical current	A

I_{rf}	high-frequency (rf) electrical current	A
j	electrical current density	$\mathrm{A/m^2}$
j_c	critical current density	$\mathrm{A/m^2}$
j_{rf}	high-frequency (rf) electrical current density	$\mathrm{A/m^2}$
k	Boltzmann's constant	$1.3807 \cdot 10^{-23}$ Nm/K
k_0	free space wavenumber $= \omega/c$	$\mathrm{s^{-1}}$
$\vec{k}, \vec{K}, \vec{Q}$	linear monetum	kgm/s
h, H	height	m
κ	filling factor: fraction of stored electromagnetic energy	
l	mean free path	m
λ	magnetic field penetration depth	m
λ_C	Campbell penetration depth	m
λ_J	Josephson penetration depth	m
λ_L	London penetration depth = magnetic field penetration depth of a superconductor	m
λ_n	Skin depth = rf field penetration depth of a conventional metal	m
Λ	electron-phonon coupling constant	
m_e	electron mass	$9.1095 \cdot 10^{-34}$ kg
m^*	effective mass	in units of m_e
μ_0	magnetic permeabilty of vacuum	$1.2566 \cdot 10^{-6}$ Vs/Am
μ_r	relative magnetic permeabilty	
N, N_n, N_s	charge carrier density: total, normal-conducting electrons, superconducting electrons	$\mathrm{m^{-3}}$
n_q, n_s	normalized charge carrier density: quasiparticles, superconducting electrons	$\mathrm{m^{-3}}$
ω	angular frequency	Hz
ω_c	cyclotron frequency ($= e\mu_0 H/m^*$)	Hz
ω_p	pinning frequency $= \alpha_p/\eta$	Hz
P	power	W
dP/dA	power loss per unit area	$\mathrm{W/m^2}$
ϕ	phase	degree, radian
ϕ_0	magnetic flux quantum $= h/2e$	$2.07 \cdot 10^{-15}$ $\mathrm{T/m^2}$
$\Psi_{a,b}$	overlap of wavefunctions	
R	resistance	Ω
R_s	surface resistance (=real part of Z_s)	Ω
R_{res}	residual surface resistance (=$R_s(T \rightarrow 0\mathrm{K})$)	Ω
ρ	resistivity	Ωm
$\sigma = \sigma_1 - i\sigma_2$	complex conductivity	$1/\Omega$m
T	absolute temperature	K
t	time	s
t_f	film thickness	m
$\tan\delta$	loss tangent (=$\epsilon_{r,2}/\epsilon_{r,1}$	
TM_{mnp}	transverse magnetic mode of the order m, n, p	
TE_{mnp}	transverse electric mode of the order m, n, p	

TEM_{mnp}	transverse electromagnetic mode of the order m, n, p	
τ, τ^{-1}	scattering time, scattering rate	s, s^{-1}
v_F	Fermi velocity = $\sqrt{2E_F/m^*}$	m/s
X_s	surface reactance (=imaginary part of Z_s)	Ω
ξ_0	BCS-coherence length	m
ξ_F	effective coherence length	m
Z_s	complex impedance	Ω
Z_s	complex surface impedance	Ω
Z_0	wave impedance of vacuum = $\sqrt{\mu_0/\epsilon_0}$	376.7 Ω

Bibliography

[1] M.Hein, Microwave properties of high-temperature superconductors: surface impedance, circuits and systems, in *Studies of High-Temperature Superconductors*, volume 18, Nova Science Publisher, 1995.

[2] M.Rolfes, Superconductors: the wireless industry comes of age, *Superconductor Industry*, Winter 95:24, 1995.

[3] N.Klein, G.Müller, H.Piel, B.Roas, L.Schultz, U.Klein, and M.Peiniger, Millimeter wave surface resistance of epitaxial grown $YBa_2Cu_3O_7$ thin films, *Appl.Phys.Lett.*, 54:757, 1989.

[4] N.Klein, Electrodynamic properties of high temperature superconductor films, in *Synthesis and characterization of high-temperature superconductors*, volume 130-132, Material Science Forum, 1993.

[5] K.F.Renk, Far-infrared spectroscopy of high temperature superconductors, *Studies of High-Temperature Superconductors*, 10, 1991.

[6] S.J.Penn, T.W.Button, P.A.Smith, and N.McN Alford, Radio-frequency and low noise performance of $YBa_2Cu_3O_7$ thick films, *Proc. of the 1994 European Conference on Applied Superconductivity, Edinburgh, Inst. Phys. Conf.*, 148:1051, 1995.

[7] R.D.Parks, *Superconductivity*, Marcel Dekker, Inc., New York, 1969.

[8] V.Z.Kresin, H.Morawitz, and S.A.Wolf, *Mechanism of conventional and high T_c superconductivity*, Oxford University Press, 1993.

[9] D.S.Dessau, Z.X.Shen, D.M.King, D.S.Marshall, L.W.Lombardo, P.H.Dickinson, A.G.Loeser, J.DiCarlo, C.H.Park, A.Kapitulnik, and W.E.Spicer, Key features in the measured band structure of $Bi_2Sr_2CaCu_2O_{8+\delta}$: flat bands at E_f and Fermi surface nesting, *Phys. Rev. Lett.*, 71:2781, 1993.

[10] C.T.Rieck, W.A.Little, J.Ruvalds, and A.Virosztek, Energy gap, susceptibility, and damping in superconducting cuprates, *Sol. State Comm.*, 88:395, 1993.

[11] S.M.Quinlan, D.J.Scalapino, and N.Bulut, Superconducting quasiparticle lifetime due to spin-fluctuation scattering, *Phys. Rev. B*, 49:1470, 1994.

[12] J.Halbritter, On rf-residual losses in superconducting cavities, *Proceedings of the Second Workshop on RF Superconductivity, Geneva*, page 23, 1984.

[13] W.Buckel, *Supraleitung: Grundlagen und Anwendungen*, VCH Verlagsgesellschaft mbH, 1993.

[14] U.Welp, W.K.Kwok, G.W.Crabtree, K.G.Vandervoort, and J.Z.Liu, Magnetic measurements of the upper critical field of $YBa_2Cu_3O_{7-\delta}$ single crystals, *Phys. Rev. Lett.*, 62:1908, 1989.

[15] R.Gross, P.Chaudary, M.Kawasaki, and A.Gupka, Scaling behavior in electrical transport across grain boundaries in $YBa_2Cu_3O_{7-\delta}$ superconductors, *Phys. Rev. B*, 42:10735, 1990.

[16] R.Gross and B.Mayer, Transport processes and noise in $YBa_2Cu_3O_{7-\delta}$ grain boundary junctions, *Physica C*, 180:235, 1991.

[17] J.A. Stratton, *Electromagnetic theory*, McGraw-Hill Publishing Company, 1941.

[18] J.H.Hinken, *Superconductor-Electronics: Fundamentals and Microwave Applications*, Springer, New York, 1989.

[19] H.London and F.London, *Proc. Roy. Soc. (Lond.)*, A149:71, 1935.

[20] S.S. Gorter and H.Casimir, *Phys. Z.*, 35:963, 1934.

[21] N.Klein, H.Chaloupka, G.Müller, S.Orbach, H.Piel, B.Roas, L.Schultz, U.Klein, and M.Peiniger, The effective microwave surface impedance of epitaxial $YBa_2Cu_3O_{7-\delta}$ thin films, *J. Appl. Phys.*, 67:6940, 1990.

[22] M.Tinkham, *Introduction to Superconductivity*, 1975.

[23] J.P.Turneaure, J.Halbritter, and H.A.Schwettmann, The surface impedance of superconductors and normal conductors: the Mattis-Bardeen theory, *Journal of Superconductivity*, 4:341, 1991.

[24] D.C.Mattis and J.Bardeen, Theory of the anomalous skin effect in normal and superconducting metals, *Physical Review*, 111:412, 1958.

[25] A.A.Abrikosov, L.P.Gor'kov, and I.M.Khalatnikov, A superconductor in a high frequency field, *Soviet Physics JETP*, 35:182, 1959.

[26] A.A.Abrikosov and L.P.Gor'kov, On the theory of superconducting alloys, *Soviet Physics JETP*, 35:1090, 1959.

[27] G.E.H.Reuter and E.H.Sondheimer, The theory of the anomalous skin effekt in metals, *Proc. Roy. Soc*, A195:336, 1949.

[28] J.P.Turneaure, *PhD thesis, Stanford University*, 1967.

[29] J.Halbritter, On surface resistance of superconductors, *Z.Physik*, 266:209, 1974.

[30] R.Blasche and R.Blocksdorf, Influence of the inelastic electron-phonon scattering on the superconducting surface resistance, *Z.Physik B*, 49:99, 1982.

[31] G.Müller, Supraleitende Niobresonatoren im Millimeterwellenbereich, *Dissertation, Universität Wuppertal*, WUB DI 83-1, 1983.

[32] C.Zuccaro, Mikrowellen-Oberflächenimpedanz von Metallen und Hochtemperatur-Supraleitern: nichtlokale und nichtmomentane Effekte, *Diplomarbeit, Universität Hamburg*, 1995.

[33] M.Peiniger, Experimentelle Untersuchungen an supraleitenden Nb_3Sn-Resonatoren iim Mikrowellenbereich, *Dissertation, Universität Wuppertal*, WUB DIS 89-1, 1989.

[34] F.Marsiglio, Coherence effects in electromagnetic absorption in superconductors, *Phys. Rev. B*, 44:5373, 1991.

[35] J.Halbritter, Submillimeter surface impedance and relexation: a case study of quasi-two-dimensional $YBa_2Cu_3O_{7-x}$, *Journal of Superconductivity*, 5:171, 1992.

[36] G.Müller, *Habilitationsschrift, Universität Wuppertal*, 1994.

[37] J.G.Bednorz and K.A.Müller, Possible high-T_c superconductivity in the Ba-La-Cu-O system, *Z.Physik B*, 64:189, 1986.

[38] Barbara Goss Levi, In high-T_c superconductors, is *d*-wave the new wave?, *Physics Today*, May 1993:17, 1993.

[39] N.Klein, Brauchen wir einen neuen Mechanismus zur Erklärung der Hoch-T_c-Supraleitung?, *Physikalische Blätter*, 50:551, 1994.

[40] J.Halbritter, Rf residual losses, surface impedance, and granularity in superconducting cuprates, *J. Appl. Phys.*, 68:6315, 1990.

[41] B.Raveau, C.Michel, M.Hervien, and D.Groult, *Crystal chemistry of high-T_c superconducting copper oxides*, Springer Verlag, 1991.

[42] E.V.Antipov, S.N.Putilin, E.N.Kopnin, J.J.Capponi, C.Chaillout, S.M.Loureiro, M.Marezio, and A.Santoro, Mercury-based copper mixed-oxide superconductors, *Physica C*, 235-240:21, 1994.

[43] M.Hervieu, C.Michel, G.Van Tendeloo, C.Martin, A.Maignan, and B.Raveau, Copper oxycarbonates and mercury based cuprates: structural mechanisms of new superconductors, *Physica C*, 235-240:25, 1994.

[44] H.Claus, M.Braun, A.Erb, K.Röhberg, B.Runtsch, H.Wühl, G.Bräuchle, P.Schweib, G.Müller-Vogt, and H.v.Löhneysen, The "90K plateau" of oxygen deficient $YBa_2Cu_3O_{7-\delta}$ single crystals, *Physica C*, 198:42, 1992.

[45] R.Hauff, V.Breit, H.Claus, D.Herrmann, A.Knierim, P.Schweiss, H.Wühl, A.Erb, and G.Müller-Vogt, Superconductivity in overdoped $YBa_2Cu_3O_{7-x}$ single crystals near x=7, *Physica C*, 235:1953, 1994.

[46] Y.Kubo, Y.Shimakawa, T.Satoh, S.Iijima, T.Ichihashi, and H.Igarashi, Large T_c-variation from 0K to 80K and hole concentration in $Tl_2Ba_2CuO_6$, *Physica C*, 162-164:991, 1989.

[47] M.I.Faley, U.Poppe, H.Soltner, U.Dähne, N.Klein, H.Schulz, and W.Evers, Variation of oxygen content in $YBa_2Cu_3O_{7-x}$ films deposited by high oxygen pressure dc-sputtering, *IEEE Trans. on Applied Superconductivity*, 3:1082, 1993.

[48] U.Poppe, N.Klein, U.Dähne, H.Soltner, C.L.Jia, B.Kabius K.Urban, A.Lubig, K.Schmidt, S.Hensen, S.Orbach, G.Müller, and H.Piel, Low-resistivity epitaxial $YBa_2Cu_3O_7$ thin films with improved microstructure and reduced microwave losses, *J. Appl. Phys.*, 71:5572, 1992.

[49] J.Schützmann, S.Tajima, S.Miyamoto, and S.Tanaka, c-axis optical response of fully oxygenated $YBa_2Cu_3O_{7-\delta}$: observation of dirty-limit-like superconductivity and residual unpaired carriers, *Phys. Rev. Lett.*, 73:174, 1994.

[50] R.Kleiner and P.Müller, Intrinsic Josephson effects in high-T_c superconductors, *Phys. Rev. B*, 49:1327, 1994.

[51] P.Zimmermann, H.Keller, S.L.Lee, I.M.Savic, M.Warden, D.Zech, R.Cubitt, E.M.Forgan, E.Kaldis, J.Karpinski, and C.Krüger, Muon-spin-rotation studies of the temperature dependence of the magnetic penetration depth in the $YBa_2Cu_3O_7$ family and related compounds, *Phys. Rev. B*, 52:541, 1995.

[52] G.J.Dolan, F.Holtzberg, C.Feild, and T.R. Dinger, Anisotropic vortex structure of $YBa_2Cu_3O_7$, *Phys. Rev. Lett.*, 62:2184, 1989.

[53] J.-J.Chang and D.J.Scalapino, Electromagnetic response of layered superconductors, *Phys. Rev. B*, 40:4299, 1989.

[54] J.R.Schrieffer, X.G.Wen, and S.C.Zhang, Dynamic spin fluctuation and the spin bag mechanism of high-T_c superconductivity, *Phys. Rev. B*, 39:11663, 1989.

[55] P.Monthoux, A.V.Balatsky, and D.Pines, Weak-couling theory of high-temperature superconductivity in the antiferromagnetically correlated copper oxides, *Phys. Rev. B*, 46:14803, 1992.

[56] G.Müller, N.Klein, A.Brust, H.Chaloupka, M.Hein, S.Orbach, H.Piel, and D.Reschke, Survey of microwave surface impedance data of high-T_c superconductors — evidence for nonpairing charge carriers, *Journal of Superconductivity*, 3:235, 1990.

[57] T.A.Friedmann, M.W.Rabin, J.Giapintzakis, J.P.Rice, and D.M.Ginsberg, Direct measurement of the anisotropy of the resistivity in the a-b plane of twin-free, single crystal, superconducting $YBa_2Cu_3O_{7-x}$, *Phys. Rev. B*, 42:6217, 1990.

[58] Z.Schlesinger, L.D.Rotter, R.T.Collins, F.Holtzberg, and C.Feild, Infrared properties of high-T_c superconductors, *Physica C*, 185-189:57, 1991.

[59] A.Zibold, L.Widder, H.P.Geserich, G.Bräuchle, H.Claus, H.v.Löhneysen, N.Nücker, A.Erb, and G.Müller-Vogt, Optical investigation of the metal-insulator transition regime in single-domain crystals of $YBa_2Cu_3O_x$, *Physica C*, 212:365, 1992.

[60] S.Takahashi, A.Shoyama, and M.Tachiki, Optical conductivity in the superconducting state of layered cuprate oxides, *Physica C*, 185-189:1677, 1991.

[61] M.Tachiki, T.Koyama, and S.Takahashi, Superconducting properties of layered oxides. *Progress of Theoretical Physics*, 108:297, 1992.

[62] S.H.Liu and R.A.Klemm, Energy-gap structure of layered superconductors, *Phys. Rev. B*, 48:10650, 1993.

[63] R.A.Klemm and S.H.Liu, Role of normal layers in penetration depth determinations of the pairing state in high-T_c superconductors, *Phys. Rev. Lett.*, 74:2343, 1995.

[64] J.R Kirtley, Tunneling measurements of the energy gap in high-T_c superconductors, *Intern. J. of Modern Physics*, 4:201, 1990.

[65] D.A.Bonn, Ruixing Liang, T.M.Riseman, D.J.Baar, D.C.Morgan, Kuan Zhang, P.Dosanjh, T.L.Duty, A.MacFarlane, G.D.Morris, J.H.Brewer, and W.N.Hardy, Microwave determination of the quasiparticle scattering time in $YBa_2Cu_3O_{6.95}$, *Phys. Rev. B*, 47:11314, 1993.

[66] U.Dähne, Y.Goncharov, N.Klein, N.Tellmann, G.Kozlov, and K.Urban, Frequency and temperature dependence of the millimeter wave conductivity of epitaxial $YBa_2Cu_3O_7$, *Journal of Superconductivity*, 8:129, 1995.

[67] D.Walker and K.Scharnberg, Electromagnetic response of high-T_c superconductors. *Phys. Rev. B*, 42:2211, 1990.

[68] T.L.Hylton, A.Kapitulnik, M.R.Beasley, J.P.Carini, L.Drabeck, and G.Gruener, Weakly coupled grain model of high-frequency losses in high T_c superconducting thin films, *Appl.Phys.Lett.*, 53:1343, 1988.

[69] A.M.Portis, *Electrodynamics of high temperature superconductors*, World Scientific, Singapore, 1993.

[70] R.Gross, L.Alff, A.Beck, O.M.Froehlich, R.Gerber, R.Gerdemann, A.Marx, B.Mayer, and D.Koelle, On the nature of high-T_c josephson junctions-clues from noise and spatially resolved analysis, *Proceedings of the* 2^{nd} *Workshop on HTS applications and new materials*, page 8, 1995.

[71] P.P.Nguyen, D.E.Oates, G.Dresselhaus, and M.S.Dresselhaus, Nonlinear surface impedance of $YBa_2Cu_3O_{7-x}$ thin films: measurements and a coupled grain model, *Phys. Rev. B*, 48:6400, 1993.

[72] C.L.Jia, H.Soltner, B.Kabius, U.Poppe, and K.Urban, A study of antiphase boundaries and "223" planar faults in epitaxial $YBa_2Cu_3O_7$ films by high resolution electron microscopy, *Physica C*, 182:163, 1991.

[73] H.P.Lang, H.Haefke, G.Leemann, and H.-J.Güntherodt, Scanning tunneling microscopy study of different growth stages of $YBa_2Cu_3O_{7-\delta}$ thin film, *Physica C*, 194:81, 1992.

[74] B.Dam, J.H.Rector, N.Koeman, and P.Griessen, Growth, defects and surface morphology of pulsed laser deposited films, *Proceedings of the* 2^{nd} *Workshop on HTS applications and new materials*, pages 57, 1995.

[75] G.M.Fischer, A.V.Andreev, Y.Y.Divin, T.Freltoft, J.Mygind, N.F.Pedersen, Y.Shen, and P.Vase, AC josephson effect in $YBa_2Cu_3O_{7-\delta}$ bicrystal grain boundary junctions, *Physica B*, 194-196:1687, 1994.

[76] S.Sridhar, Nonlinear microwave impedance of superconductors and ac response of the critical state, *Appl.Phys.Lett.*, 65:1054, 1994.

[77] C.T.Rieck, Universität Hamburg, private communication.

[78] A.A.Golubov, O.V.Dolgov, E.G.Maksimov, I.I.Mazin, and S.V.Shulga, Strong-coupling effects in s-wave two-band superconductor, *Physica C*, 235-240:2383, 1994.

[79] B.A.Aminov, M.A.Hein, G.Müller, H.Piel, D.Wehler, Ya.G.Pomomarev, K.Rosner, and K.Winzer, Two-gap structure in $YBa_2Cu_3O_{7-x}$ single crystals, *Journal of Superconductivity*, 7:459, 1994.

[80] A.A. Golubov, Forschungszentrum Jülich GmbH, private communication.

[81] V.Z.Kresin and S.A.Wolf, Induced superconducting state and two-gap structure: application to cuprate superconductors and conventional multilayers, *Phys. Rev. B*, 46:6458, 1992.

[82] V.Z.Kresin and S.A.Wolf, Induced superconductivity and gapless state in $YBa_2Cu_3O_{7-x}$, *Physica C*, 198:328, 1992.

[83] M.Tachiki and S.Takahashi, Theory of superconductivity in multilayer systems, *Physica B*, 169:121, 1991.

[84] Ya.G.Ponomarev, B.A.Aminov, M.A.Hein, H.Heinrichs, V.Z.Kresin, G.Müller, H.Piel, K.Rosner, S.V.Tchesnokov, E.B.Tsokur, D.Wehler, K.Winzer, A.V.Yarygin, and K.T.Yusupov, Josephson effect and single-particle tunneling in $YBa_2Cu_3O_{7-x}$ and $YbBa_2Cu_3O_{7-x}$ single-crystal break junctions, *Physica C*, 243:167, 1995.

[85] S.D.Adrian, M.E.Reeves, S.A.Wolf, and V.Z.Kresin, Penetration depth in layered superconductors: applications to the cuprates and conventional multilayers, *Phys. Rev. B*, 51:6800, 1995.

[86] P.J.Hirschfeld, W.O.Putikka, and D.J.Scalapino, Microwave conductivity of d-wave superconductors, *Phys. Rev. Lett.*, 71:3705, 1993.

[87] P.J.Hirschfeld, W.O.Putikka, and D.J.Scalapino, d-wave model for microwave response of high-T_c superconductors, *Phys. Rev. B*, 50:10250, 1994.

[88] R.A.Klemm, K.Scharnberg, D.Walker, and C.T.Riek, Electromagnetic response of unconventional superconductors, *Z.Physik B*, 72:139, 1988.

[89] T.Jacobs, S.Sridhar, C.T.Rieck, K.Scharnberg, T.Wolf, and J.Halbritter, Microwave surface impedance of $YBa_2Cu_3O_{7-\delta}$ crystals: Experiment and comparison to a d-wave model, *J. Phys. Chem. Solids*, 56:1945, 1995.

[90] P.Monthoux and D.J.Scalapino, Self-consistent $d_{x^2-y^2}$ pairing in a two-dimensional Hubbard model, *Phys. Rev. Lett.*, 72:1874, 1994.

[91] P.Monthoux and D. Pines, Spin fluctuation induced superconductivity and normal state properties of $YBa_2Cu_3O_7$, *Phys. Rev. B*, 49:4261, 1994.

[92] Chien-Hua Pao and N.E.Bickers, Anisotropic superconductivity in the 2D Hubbard model: gap function and interaction weight, *Phys. Rev. Lett.*, 72:1870, 1994.

[93] D.J.Scalapino, The case for $d_{x^2-y^2}$ pairing in the cuprate superconductors, *Physics Reports*, 250:329, 1995.

[94] S.K.Yip and J.A.Sauls, Nonlinear Meissner effect in CuO superconductors, *Phys. Rev. Lett.*, 69:2264, 1992.

[95] D.Xu, S.K.Yip, and J.A.Sauls, The nonlinear meisner effect in unconventional superconductors, *Phys. Rev. B*, 51:16233, 1995.

[96] M.W.Coffey and J.R.Clem, Unified theory of effects of vortex pinning and flux creep upon the rf surface impedance of type-II superconductors, *Phys. Rev. Lett.*, 67:386, 1991.

[97] E.H.Brandt, Flux line lattice in high-T_c superconductors: anisotropy, elasticity, fluctuation, thermal depinning, ac penetration and susceptibility, *Physica C*, 195:1, 1992.

[98] S.Ravenaz, D.E.Oates, B.Labbe-Lavigne, G.Dresselhaus, and M.S.Dresselhaus, Frequency dependence of Z_s of $YBa_2Cu_3O_{7-\delta}$ thin films in a dc magnetic field: investigation of vortex dynamics, *Phys. Rev. B*, 50:1178, 1994.

[99] M.Golosovsky, M.Tsindlekht, and D.Davidov, High-frequency vortex dynamics in $YBa_2Cu_3O_7$, *Phys. Rev. B*, 50:470, 1994.

[100] Dong-Ho Wu, J.C.Booth, and S.M.Anlage, Frequency and field variation of vortex dynamics in $YBa_2Cu_3O_{7-\delta}$, *Phys. Rev. Lett.*, 75:525, 1995.

[101] J.P.Carini, A.M.Awasthi, W.Beyermann, G.Gruner T.Hylton, K.Char, M.R.Beasley, and A.Kapitulnik, Millimeter-wave surface resistance measurements in highly oriented $YBa_2Cu_3O_7$ thin films, *Phys. Rev. B*, 37:9726, 1988.

[102] L.Drabeck, G.Gruner, J.-J.Chang, A.Inam, X.D.Wu, L.Nazar, T.Venkatesan, and D.J.Scalapino, Millimeter-wave surface impedance of $YBa_2Cu_3O_7$ thin films, *Phys. Rev. B*, 40:7350, 1989.

[103] L.Drabeck, K.Holczer, G.Gruner, J.-J.Chang, D.J.Scalapino, A.Inam, X.D.Wu, L.Nazar, and T.Venkatesan, Surface resistance of laser deposited $YBa_2Cu_3O_7$ films, *Phys. Rev. B*, 42:10020, 1990.

[104] S.Hensen et al., Effect of small changes in metalstoichiometry on microwave losses of epitaxial grown $YBa_2Cu_3O_{7-x}$ films, *Proc. of the 1st European Conference on Applied Superconductivity*, page 1053, 1993.

[105] N.Tellmann, N.Klein, U.Dähne, A.Scholen, H.Schulz, and H.Chaloupka, High-Q $LaAlO_3$ dielectric resonator shielded by $YBa_2Cu_3O_7$ films, *IEEE Transactions on Applied Superconductivity*, 4:143, 1994.

[106] A.Scholen, Untersuchung der Oberflächenimpedanz von epitaktischen $YbBa_2Cu_3O_{7-\delta}$-Dünnfilmen bei 19 und 37 GHz, *Diplomarbeit, RWTH Aachen*, 1995.

[107] V.N.Egorov and V.L.Masalov, Whispering-gallery mode dielectric resonators: theory and applications in low-noise oscillators, *Radiotech. and Electron.*, 32:1071, 1987.

[108] V.B.Braginsky, V.S.Ilchenko, and Kh.S.Bagdassarov, Experimental observation of fundamental microwave absorption in high-quality dielectric crystals, *Phys.Lett.A*, 120:300, 1987.

[109] R.Heidinger, Dielectric measurements on sapphire for electron cyclotron wave systems, *Journal of Nuclear Sciences*, 212-215:1101, 1992.

[110] N.Klein, U.Dähne, U.Poppe, N.Tellmann, K.Urban, S.Orbach, S.Hensen, G.Müller, and H.Piel, Microwave surface resistance of epitaxial $YBa_2Cu_3O_{7-\delta}$ films at 18.7 GHz measured by a dielectric resonator technique, *Journal of Superconductivity*, 5:195, 1992.

[111] Y.Kobayashi, T.Imai, and H.Kayano, Microwave measurement of temperature and current dependences of surface impedance for high-T_c superconductors, *IEEE Trans. on Microwave Theory and Techniques*, 39:1530, 1991.

[112] Z-Y.Shen, C.H.Wilker, Ph.Pang, W.L.Holstein, D.Face, and D.J.Kountz, High T_c superconducting-sapphire microwave resonator with extremely high Q-values up to 90K, *IEEE Trans. on Microwave Theory and Techniques*, 40:2424, 1992.

[113] J.Krupka, M.Klinger, M.Kuhn, A.Baranyak, M.Stiller, J.Hinken, and J.Modelski, Surface resistance measurements of HTS films by means of sapphire dielectric resonators, *IEEE Transactions on Applied Superconductivity*, 3:3043, 1993.

[114] W.Diete, B.Achermann, H.Chaloupka, M.Jeck, T.Kamppeter, S.Kolesov, G.Müller, H.Piel, and H.Schlick, New measurement techniques for the surface resistance and its power dependence of large-area $YBa_2Cu_3O_{7-\delta}$ films, *Proceedings of the Second European Conference on Applied Superconductivity, Inst. Phys. Conf.*, Ser. No 148:1107, 1995.

[115] H.Chaloupka, Universität Wuppertal, private communication.

[116] A.G.Zaitsev R.Wördenweber, G.Ockenfuss, R.Kutzner, T.Königs, C.Zuccaro, and N.Klein, Microwave losses and structural properties of large area $YBa_2Cu_3O_7$ films on r-cut sapphire buffered with (001) / (111) oriented CeO_2, *Proceedings of the 1996 Applied Superconductivity Conference, Pittsburgh.*

[117] G.Hampel, P.Kolodner, P.L.Gammel, P.A.Polakos, E.de Obaldia, P.M.Mankiewich, A.Anderson, R.Slattery, D.Zhang, G.C.Liang, and C.F.Shih, High power failure of superconducting microwave filters: investigation by means of thermal imaging, *Appl.Phys.Lett.*, 69:571, 1996.

[118] D.Schmitt and T.Weiland, Status and future of the 3d mafia group of codes *IEEE Trans. on Microwave Theory and Techniques*, 42:1886, 1994.

[119] M.Hein, Universität Wuppertal, private communication.

[120] M.Hein, W.Diete, M.Getta, S.Hensen, T.Kaiser, G.Müller, H.Piel, and H.Schlick, Fundamental limits of the linear microwave response of epitaxial Y-Ba-Cu-O films, *Proceedings of the 1996 Applied Superconductivity Conference, Pittsburgh.*

[121] W.Diete, M.Getta, M.Hein, T.Kaiser, G.Müller, H.Piel, and H.Schlick, Surface resistance and nonlinear microwave losses of epitaxial HTS films, *Proceedings of the 1996 Applied Superconductivity Conference, Pittsburgh.*

[122] P.F.Goldsmith, *Infrared and Millimeter Waves*, volume 6, K.J.Button, Academic Press, New York, 1992.

[123] J.S.Martens, V.M.Hietala, D.S.Ginley, T.E.Zipperian, and G.K.G.Hohenwarter, Confocal resonator for measuring the surface resistance of high - temperature superconducting films, *Appl.Phys.Lett.*, 58:2543, 1991.

[124] J.S.Martens, S.M.Garrison, and S.A.Sachtjen, Surface resistance analysis: A new thin-film characterization tool, *Solid State Technology*, Dec. 94:51, 1994.

[125] T.E. Harrington, J.Wosik, S.A.Long, Open resonator mode patterns for characterization of unisotropic HTS thin films and dielectrics, *Proceedings of the 1996 Applied Superconductivity Conference, Pittsburgh.*

[126] A.Porch, M.J.Lancaster, and R.G.Humphreys, The coplanar resonator technique for determining the surface impedance of $YBa_2Cu_3O_{7-\delta}$ thin films, *IEEE Trans. on Microwave Theory and Techniques*, 43:306, 1995.

[127] D.E.Oates, A.C.Anderson, D.M.Sheen, and S.M.Ali, Stripline resonator measurements of Z_s versus H_{rf} in $YBa_2Cu_3O_{7-x}$ thin films, *IEEE Trans. on Microwave Theory and Techniques*, 39:1522, 1991.

[128] R.C.Taber, A parallel plate resonator technique for microwave loss measurements on superconductors, *Rev.Sci.Instrum.*, 61:2200, 1990.

[129] R.K.Hoffmann, *Handbook of Microwave Integrated Circuts*, Artech House Inc., 1987.

[130] D.E.Oates, P.P.Nguyen, G.Dresselhaus, M.S.Dresselhaus, C.W.Lam, and S.M.Ali, Measurements and modelling of linear and nonlinear effects in striplines, *Journal of Superconductivity*, 5:361, 1992.

[131] J.Krupka, R.G.Geyer, M.Kuhn, and J.H.Hinken, Dielectric properties of single crystals of Al_2O_3, $LaAlO_3$, $NdGaO_3$, $SrTiO_3$, and MgO at cryogenic temperatures, *IEEE Trans. on Microwave Theory and Techniques*, 42:1886, 1994.

[132] N.Klein, N.Tellmann, C.Zuccaro, P.Swiatek, and H.Schulz, $YBa_2Cu_3O_7$ shielded high permittivity dielectric resonators for stable oscillators, *Proc. of the 1994 European Conference on Applied Superconductivity, Edinburgh, Inst. Phys. Conf.*, 148:743, 1995.

[133] U.Dähne, Submillimeterwellen - Spektroskopie an Hochtemperatur - Supraleitern, *Dissertation, RWTH Aachen*, 1995.

[134] D.Wehler, G.Müller, Ch.Murek, H.Piel, K.Schönmann, Th.Wolf, and S.A.Wolf, Anisotropic microwave losses of partially untwinned $YBa_2Cu_3O_{7-x}$-single crystals, *Physica C*, 235-240:2003, 1994.

[135] D.Wehler, *Dissertation, Bergische Universität Wuppertal*, 1996.

[136] L.D.Chang, M.J.Moskowitz, R.B.Hammond, M.M.Eddy, W.L.Olson, D.D.Casavant, E.J.Smith, and M.Robinson, Microwave surface resistance in Tl-based superconducting thin films, *Appl.Phys.Lett.*, 55:1357, 1989.

[137] W.N.Hardy, D.A.Bonn, D.C.Morgan, Ruixing Liang, and Kuan Zhang, Precision measurements of the temperature dependence of λ in $YBa_2Cu_3O_{6.95}$: strong evidence for nodes in the gap function, *Phys. Rev. Lett.*, 70:3999, 1993.

[138] D.A.Bonn, S.Kamal, Kuan Zhang, Ruixing Liang, D.J.Baar, E.Klein, and W.Hardy, Comparison of the influence of Ni and Zn impurities on the electromagnetic properties of $YBa_2Cu_3O_{6.95}$, *Phys. Rev. B*, 50:4051, 1994.

[139] D.R.Cohn, S.C.Han, P.P.Woskov, B.L.Zhou, A.Ferdinand, R.H.Giles, J.Waldman, D.W.Cooke, and R.E.Muenchhausen, Precision submillimeter wave laser reflection measurements of high-temperature superconductors, *Journal of Superconductivity*, 4:389, 1992.

[140] A.A.Volkov, B.P.Gorshunov, G.V.Kozlov, S.I.Krasnosvobodtsev, E.V.Pechen, O.I.Sirotinski, and Ya.Pettselt, Electrodynamic properties of a superconducting film of Y-Ba-Cu-O in the submillmeter band, *Sov. Phys. JETP*, 68:148, 1989.

[141] D.Miller, P.L.Richards, S.Etemand, A.Inam, T.Venkatesan, B.Dutta, X.D.Wu, C.B.Eom, T.H.Geballe, N.Newman, and B.F.Cole, Residual losses in epitaxial thin films of $YBa_2Cu_3O_7$, from microwave to submillimeter wave frequencies, *Appl.Phys.Lett.*, 59:2326, 1991.

[142] D.Miller, P.L.Richards, S.M.Garrison, N.Newman, C.B.Eom, T.H.Geballe, S.Etemand, A.Inam, T.Venkatesan, J.S.Martens, W.Y.Lee, and L.C.Bourne, Submillimeter and microwave residual losses in epitaxial films of Y-Ba-Cu-O and Tl-Ca-Ba-Cu-O, *Journal of Superconductivity*, 5:379, 1992.

[143] D.N.Basov, M.Müller, A.Koller, J.Schützmann, E.V.Pechen, J.Betz, B.Brunner, and K.F.Renk, Study of residual absorption of high-T_c thin films by means of photothermal interference spectroscopy, *Springer Series in Solid-State Science*, 113:282, 1993.

[144] M.C.Nuss, K.W.Goossen, P.M.Mankiewich, M.L.O'Malley, J.L.Marshall, and R.E.Howard, On the surface resistance of $YBa_2Cu_3O_7$ between 10 and 500 GHz, *IEEE Trans. Magn.*, 27:863, 1991.

[145] M.C.Nuss, K.W.Goossen, P.M.Mankiewich, and M.L.O'Malley, Terahertz surface impedance if thin $YBa_2Cu_3O_7$ superconducting films, *Appl.Phys.Lett.*, 58:2561, 1991.

[146] M.C.Nuss, P.M.Mankiewich, M.L.O'Malley, E.H.Westerwick, and Peter Littlewood, Dynamic conductivity and "coherence peak"in $YBa_2Cu_3O_7$ superconductors, *Phys. Rev. Lett.*, 66:3305, 1991.

[147] D.L.Rubin, K.Green, J.Gruschus, J.Kirchgessner, D.Moffat, H.Padamsee, J.Sears, Q.S.Shu, L.F.Schneemeyer, and J.V.Waszczak, Observation of a narrow superconducting transition at 6 GHz in crystals of $YBa_2Cu_3O_7$, *Phys. Rev. B*, 38:6538, 1988.

[148] S.Orbach, Oberflächenimpedanz epitaktisch aufgewachsener $YBa_2Cu_3O_{7-\delta}$-Filme bei 87 GHz, *Dissertation, Universität Wuppertal*, report WUB-DIS 94-9, 1994.

[149] N.Klein, N.Tellmann, S.A.Wolf, and V.Z.Kresin, Microwave surface impedance of $YBa_2Cu_3O_{7-x}$-films: s-wave versus d-wave pairing, *Journal of Superconductivity*, 7:459, 1994.

[150] J.Geerk, G.Linker, and O.Mayer, Epitaxial growth and properties of Y-Ba-Cu-O thin films, *Mat. Sci. Repts.*, 4:193, 1989.

[151] R.G.Humphreys, J.S.Satchell, N.G.Chew, J.A.Edwards, S.W.Goodyear, S.E.Blenkinsop, O.D.Dosser, and A.G.Gullis, Physical vapour deposition techniques for the growth of $YBa_2Cu_3O_7$ films, *Supercond. Sci. and Technol.*, 3:38, 1990.

[152] D.E.Morris, A.G.Markelz, B.Fayn, and J.H.Nickel, Conversion of 124 into 123+CuO and 124, 123 and 247 phase regions in the Y-Ba-Cu-O system, *Physica C*, 168:153, 1990.

[153] J.L. Driscoll, J.A.Alonso, P.C.Wang, T.H.Geballe, and J.C.Bravman, Studies of structural disorder in $ReBa_2Cu_3O_{7-x}$ thin films (re=rare earth) as a function of rare-earth ionic radius and film deposition conditions, *Physica C*, 232:288, 1994.

[154] B.Büchner, U.Calliess, H.D.Jostarndt, W.Schlabitz, D.Wohlleben, Correlation of spectroscopic and superconducting properties of $REBa_2Cu_3O_{7-y}$ with the rare earth ionic radius, *Solid State Comm.* 73:357, 1990.

[155] G.Müller, B.Aschermann, H.Chaloupka, W.Diete, M.Getta, M.Hein, S.Hensen, F.Hill, M.Lenkens, S.Orbach-Werbig, T.Patzelt, H.Piel, J.Rembesa, H.Schlick, T.Unselm, and R.Wagner, On-axis dc sputtered $YBa_2Cu_3O_{7-x}$ films up to 2 inches in diameter for microwave antenna arrays, *IEEE Trans. on Applied Superconductivity*, 5:1729, 1995.

[156] D.W.Face, C.Wilker, Z.Y.Shen, P.Pang, and R.J.Small, Large area $YBa_2Cu_3O_7$ films for high power microwave applications, *IEEE Trans. on Applied Superconductivity*, 5:1581, 1995.

[157] R.Semerad, B.Utz, P.Berberich, W.Prusseit, and H.Kinder, Coevaporation of $YBa_2Cu_3O_{7-\delta}$ films up to 9 inches diameter, *Proc. of the 1994 European Conference on Applied Superconductivity, Edinburgh, Inst. Phys. Conf.*, 148:847, 1995.

[158] H.Maeda, A.Koizumi, N.Bamba, E.Takayama-Muromachi, F.Izumi, H.Asano, K.Shimizu, H.Moriwaki, H.Maruyama, Y.Kuroda, and H.Yamazaki, EXAFS and neutron diffraction studies of local and average structures for $YBa_2Cu_{2.8}Zn_{0.2}O_{7-\delta}$, *Physica C*, 157:483, 1989.

[159] U.Dähne, N.Klein, H.Schulz, N.Tellmann, and K.Urban, Dynamic conductivity of epitaxial $YBa_2Cu_3O_{7-x}$ thin films up to 600 GHz, *Proc. of the 1994 European Conference on Applied Superconductivity, Edinburgh, Inst. Phys. Conf.*, 148:1095, 1995.

[160] J.M.Valles, R.C.Dynes, A.M.Cucolo, L.F.Schneemeyer M.Gurvitch, J.P.Garno, and J.V.Waszcak, Electron tunneling into single crystals of $YBa_2Cu_3O_7$, *Phys. Rev. B*, 44(21):11986, 1991.

[161] Zhengxiang Ma, Rf properties of high temperature superconducting materials, *PhD thesis, Stanford University*, G.L. Report No. 5298, 1995.

[162] N.Klein, N.Tellmann, H.Schulz, K.Urban, S.A.Wolf, and V.Z.Kresin, Evidence of two-gap s-wave superconductivity in $YBa_2Cu_3O_{7-x}$ from microwave surface impedance measurements, *Phys. Rev. Lett.*, 71:3355, 1993.

[163] M.R.Beasley, Recent penetration depth measurements of high-T_c superconductors and their implications, *Physica C*, 209:43, 1993.

[164] N.Klein, U.Poppe, N.Tellmann, H.Schulz, W.Evers, U.Dähne, and K.Urban, Microwave surface resistance of epitaxial $YBa_2Cu_3O_{7-x}$ films: studies on oxygen deficiency and disordering, *IEEE Trans. on Applied Superconductivity*, 3:1102, 1993.

[165] A.Fuchs, W.Prusseit, P.Berberich, and H.Kinder, High-precision penetration depth measurements of $YBa_2Cu_3O_{7-\delta}$ as a function of oxygen content, *Phys. Rev. B*, 53:14745, 1996.

[166] B.W.Veal, A.P.Paulikas, H.You, H.Shi, Y.Fang, and J.W.Downey, Observation of temperature-dependent site disorder in $YBa_2Cu_3O_{7-\delta}$ below 150°C, *Phys. Rev. B*, 42:6305, 1990.

[167] S.Orbach, S.Hensen, G.Müller, H.Piel, M.Lippert, G.Saemann-Ischenko, and S.A.Wolf, Effect of oxygen deficiency and disorder on microwave losses of epitaxially grown $YBa_2Cu_3O_{7-\delta}$ films, *Journal of Alloys and Compounds*, 195:555, 1993.

[168] K.Zhang, D.A.Bonn, S.Kamal, R.Liang, D.J.Baar, W.N.Hardy, D.Basov, and T.Timusk, Measurement of the a, b-plane anisotropy of microwave surface impedance of untwinned $YBa_2Cu_3O_{6.95}$ single crystals, *Phys. Rev. Lett.*, 73:2484, 1994.

[169] T.L.Hylton, Electrical transport and defect structures in yttrium-barium-copper-oxide thin films, *PhD thesis, Stanford University*, G.L. report No. 4804, 1991.

[170] J.Mao, D.H.Wu, J.L.Peng, R.L.Greene, and S.M.Anlage, Anisotropic surface impedance of $YBa_2Cu_3O_{7-\delta}$ single crystals, *Phys. Rev. B*, 51:3316, 1995.

[171] A.Zibold, K.Widder, H.P.Geserich, T.Scherer, P.Marienhoff, M.Neuhaus, W.Jutzi, A.Erb, and G.Müller-Vogt, Optical anisotropy of $YBa_2Cu_3O_{7-\delta}$ films on $NdGaO_3$ (001) substrates: a comparison with single domain crystals, *Appl.Phys.Lett.*, 61:345, 1992.

[172] D.E.Oates, MIT Lincoln Laboratory, H.Schulz and N.Klein, Forschungszentrum Jülich GmbH, unpublished (*similar results obtained by the same technique can be found in Ref.71, but here the maximum field levels are higher and the quadratic slope is lower).*

[173] J.Halbritter, Granular superconductors and their inrinsic and extrinsic surface impedance, *Journal of Superconductivity*, 8:691, 1995.

[174] B.A.Willemsen, J.S.Derov, J.H.Silva, and S.Sridhar, Nonlinear response of suspended high temperature superconducting thin film microwave resonators, *IEEE Trans. on Applied Superconductivity*, 5:1753, 1995.

[175] P.P.Nguyen, D.E.Oates, G.Dresselhaus, and M.S.Dresselhaus, Microwave hystertic losses in $YBa_2Cu_3O_{7-x}$ and NbN thin films, *Phys. Rev. B*, 51:6689, 1995.

[176] I.S.Ghosh, Micorwave losses of high-temperature superconducting thin films induces by high magnetic fields, *PhD thesis, Imperial College of Science, Technolgy and medicine, London*, 1995.

[177] G.Blatter, M.V.Feigelmann, V.B.Geshkenbein, A.I.Larkin, and V.M.Vinokur, Vortices in high-temperature superconductors, *Review Modern Physics*, 66:1147, 1994.

[178] N.Belk, D.E.Oates, A.E.Feld, G.Dresselhaus, and M.S.Dresselhaus, Frequency and temperature dependence of Z_s of $YBa_2Cu_3O_{7-\delta}$ thin films an a dc magnetic field: investigation of vortex dynamics, *Phys. Rev. B*, 52:3459, 1996.

[179] I.S.Ghosh, L.F.Cohen, V.Fry, T.Tate, A.D.Caplin, J.C.Gallop, S.Sievers, R.Somekh, S.Hensen, and M.Lenkens, Microwave losses of $YBa_2Cu_3O_{7-\delta}$ thin films in high magnetic fields, *IEEE Trans. on Applied Superconductivity*, 5:1756, 1995.

[180] A.Bourdillon and N.X.Tan Bourdillon, *High temperature superconductors: processing and science*, Academic Press, Inc., San Diego, 1993.

[181] A.Maeda, Y.Lino, T.Hanaguri, N.Motohira, K.Kishio, and T.Fukase, Magnetic field dependence of the london penetration depth of $Bi_2Sr_2CaCu_2O_y$, *Phys. Rev. Lett.*, 74:1202, 1995.

[182] U.Dähne, T.Amrein, Y.Goncharov, N.Klein, G.Kozlov, L.Schultz, N.Tellmann, and K.Urban, Temperature dependence of the millimeter wave conductivity of $YBa_2Cu_3O_7$ and $Bi_2Sr_2Ca_1Cu_2O_8$ thin films at 300 GHz, *Physica C*, 235-240:2066, 1994.

[183] Zhengxiang Ma, R.C.Taber, L.W.Lombardo, A.Kapitulnik, M.R.Beasley, P.Merchant, C.B.Eom, S.Y.Hou, and J.M.Phillips, Microwave penetration depth measurements on 2212 BSCCO single crystals and $YBa_2Cu_3O_{7-\delta}$ thin films, *Phys. Rev. Lett.*, 71:781, 1993.

[184] T.Jacobs, S.Sridhar, Qiang Li, G.D.Gu, and N.Koshizuka, In-plane and *c*-axis microwave penetration depth of $Bi_2Sr_2Ca_1Cu_2O_{8+\delta}$ crystals, *Phys. Rev. Lett.*, 75:4516, 1995.

[185] S.Huber, S.Manzel, H.Bruchlos, S.Hensen, and G.Müller, Thallium-based high-T_c films with very low surface impedance, *Physica C*, 244:337, 1995.

[186] D.Face, DuPont, private communication.

[187] A.M.Herman and J.V.Yaktimi (editors), *Thallium-based high-temperature superconductors*, Marcel Dekker, Inc., 1994.

[188] A.Lauder, C.Wilker, Z.Y.Shen, P.S.W.Pang, W.L.Holstein, D.J.Kountz, and D.W.Face, *Proceedings of the 1994 International Wire and Cable Symposium*, page 155, 1994.

[189] S.H.Yun and J.Z.Wu, Superconductivity above 130K in high-quality mercury-based cuprate thin films, *Phys. Rev. Lett.*, 68:862, 1996.

[190] S.N.Mao, X.X.Xi, Jian Mao, D.H.Wu, Qi Li, S.M.Anlage, and T.Vankatesan, Structural characterization and microwave loss of $Nd_{1.85}Ce_{0.15}CuO_{4-y}$ superconducting thin films on yttria-stabilized zirconia buffered sapphire, *Appl.Phys.Lett.*, 64:375, 1994.

[191] Dong-Ho Wu, Jian Mao, S.N.Mao, J.L.Peng, X.X.Xi, T.Venkatesan, R.L.Greene, and S.M.Anlage, Temperature dependence of penetration depth and surface resistance of $Nd_{1.85}Ce_{0.15}CuO_4$, *Phys. Rev. Lett.*, 70:85, 1993.

[192] A.Andreone, A.Cassinese, A.Di Chiari, R.Vaglio, A.Gupta, and E.Sarnelli, Temperature dependence of the penetration depth in $Nd_{1.85}Ce_{0.15}CuO_{4-\delta}$ superconducting thin films, *Phys. Rev. B*, 49:6392, 1994.

[193] C.W.Schneider, Z.H.Barber, J.E.Evetts, S.N.Mao, X.X.Xi, and T.Vankatesan, Penetration depth measurements for $Nd_{1.85}Ce_{0.15}CuO_4$ and NbCN thin films using a kinetic inductance technique, *Physica C*, 233:77, 1994.

[194] D.M.King, Z.X.Shen, D.S.Dessau, B.O.Wells, W.E.Spicer, A.J.Arko, D.S.Marshall, J.DiCarlo, A.G.Loeser, C.H.Park, E.R.Ratner, J.L.Peng, Z.Y.Li, and R.L.Greene, Fermi surface and electronic structure of $Nd_{2-x}Ce_xCuO_{4-\delta}$, *Phys. Rev. Lett.*, 70:3159, 1993.

Forschungszentrum Jülich

Jül-3773
May 2000
ISSN 0944-2952